MEASUREMENTS OF PHOTO-NEUTRONS FROM A MEDICAL LINEAR ACCELERATOR USING CR-39 PLASTIC NUCLEAR TRACK DETECTORS

By

JONATHAN MICHAEL MONSON

Bachelor of Science in Physics
Brigham Young University - Idaho
Rexburg, Idaho, United States
2010

Submitted to the Faculty of the
Graduate College of
Oklahoma State University
in partial fulfillment of
the requirements for
the Degree of
MASTER OF SCIENCE
May, 2014

MEASUREMENTS OF PHOTO-NEUTRONS FROM A MEDICAL LINEAR ACCELERATOR USING CR-39 PLASTIC NUCLEAR TRACK DETECTORS

Thesis Approved:

Eric Benton

Eduardo Yukihara

David Peakheart

ACKNOWLEDGMENTS

There are many people that I want to express my thanks and appreciation to for providing assistance in helping me accomplish my research project. I feel that mere words cannot do justice in showing how grateful I am to these individuals. I hope they will read this acknowledgment and know that their guidance, instruction, influence, and moral support were instrumental to my education and this research project.

I first want to thank my Father in Heaven in all that He has done for me. He has continued to bless me throughout my life by providing me with the opportunity to be around those who have helped shape me to who I am today. I would not be here nor have the experiences I have had without His help. I have definitely seen His tender mercies in my life and for that I am grateful.

I would like to thank my advisor, Eric Benton, for his continued guidance throughout this research. I have been extremely fortunate to have him as my advisor and to be taught under his tutelage. His passion and dedication to science has made my time here at Oklahoma State University both challenging and more importantly, fun. I am extremely grateful for him accepting me as his graduate student and having patience with me in my progression in the field of medical physics.

I would also like to thank the current and former members of the E.V. Benton Radiation Physics Laboratory: Tyler Collums, Rafiq Islam, Aaron Ruse, Nathan Lindy, Robert Honeyman, Joe Ross, Rajesh Panthi, and Maysam Tavkoli. Their assistance on this project, as well as their camaraderie during my time in this group was very important to me. I would like to especially thank Rafiq Islam and Tyler Collums for their additional help in and outside of work. Their insights and experiences were key

to this research.

I would like to thank Dr. David Peakheart at Hillcrest Medical Center in Tulsa, Oklahoma for sacrificing his time and providing us with valuable beam time for this project. I am thankful for the faculty of the Oklahoma State University Physics Department for their instruction and guidance during my coursework. I am especially thankful for Dr. Eduardo Yukihara, Dr. Jeremy Polf, and Dr. Satyanarayan Nandi for their wise council and patients in working with me throughout my academic endeavors.

I would like to thank my family for all the love and support they have offered me throughout my life. My father has always been someone whom I aspired to be like and has helped me in all aspects of life. My mother was a constant source of encouragement and love in my life. I can never truly express my gratitude for them. They have definitely shaped me to the person I am today and for that I am truly grateful.

I am thankful for my children Abigail and Daniel for making my life happier. Their love and smiling faces each day has made this research worth it.

Most importantly I want to thank my wife, Rebecca. She has supported me and sacrificed so much so that I can be here to continue my educational pursuits. She means everything to me and I could not have done it without her. Thank you so much honey, I love you.

Acknowledgements reflect the views of the author and are not endorsed by committee members or Oklahoma State University.

Name: Jonathan Michael Monson

Date of Degree: May, 2014

Title of Study: Measurement of Photo-Neutrons From a Medical Linear Accelerator Using CR-39 Plastic Nuclear Track Detectors

Major Field: Medical Physics

Photo-neutrons are produced when x-ray energies exceed 7 MeV. Photo-neutron production varies depending on x-ray beam energy. CR-39 PNTDs were used in this study to measure the neutron absorbed dose and dose equivalent produced by a Varian Clinac 23EX for x-ray beams of 6 and 18 MV_p and with a Varian Trilogy using an x-ray beam of 10 MV_p. Neutron absorbed dose and dose equivalent were measured at 100 cm SSD at 0, 20, and 40 cm off-axis from the primary beam in air. Using a polyethylene phantom the neutron absorbed dose and dose equivalent were measured at 100 cm SSD from the top of the phantom at 0, 5, and 10 cm from the surface, in the beam central axis and off-axis distances of 20 and 40 cm at a depth of 10 cm. The neutron absorbed dose and dose equivalent from medical linear accelerators have been measured from the LET spectrum of recoiled tracks produced in the CR-39 PNTDs for high energy neutrons (1-20 MeV) and the neutron dose equivalent for low energy (< 1 MeV) neutrons were measured using TRNDs. In this study, the experimentally measured absorbed dose and dose equivalent from photo-neutrons produced in a common medical linear accelerator operating at energies 10 and 18 MV_p range from 0.2 $\mu Gy_n/Gy_x$ and 2 $\mu Sv_n/Gy_x$ to 495 $\mu Gy_n/Gy_x$ and 5500 $\mu Sv_n/Gy_x$, respectively. The neutron absorbed dose for the 6 MV_p x-ray beam was measured to be 0 $\mu Gy_n/Gy_x$. Low energy neutrons accounted for less than 1% of the neutron dose equivalent. Those detectors exposed inside of the phantom measured a higher contribution from high LET (> 100 keV/μm) particles than those detectors exposed in air.

TABLE OF CONTENTS

LIST OF TABLES

LIST OF FIGURES

Figure Page

CHAPTER 1

INTRODUCTION

1.1 Photo-Neutrons

In x-ray radiation therapy, the primary objective is to deliver x-rays to the volume of a cancerous tumor, without exposing healthy tissue, thus killing the cancerous cells while minimizing the damage done to the body. This objective is not always possible due to scattering of the x-rays and other particles which takes place in the medical linear accelerator (linac) and in the body itself.

Linacs use high frequency electromagnetic waves to accelerate electrons to energies between 4 and 25 MV_p [Facure et al., 2005]. Bremsstrahlung x-rays are produced when these high energy electrons collide with the high Z nuclei of an x-ray target such as tungsten, resulting in a spectrum of x-ray energies with the maximum energy equal to the incident electron energy or peak accelerating voltage of the linac. The average x-ray energy of the beam is about one-third of the maximum energy [Krane, 1988].

When x-rays with high enough energies, greater than approximately 7 MeV, collide with high Z materials such as tungsten or lead that are found in the linac, target, shielding, collimators or flattening filters, they can overcome the threshold energy to produce neutrons. These neutrons are known as photo-neutrons since they came from x-ray interaction with high Z nuclei. Neutrons, created through photo-neutron production, have a wide range of energies. The notation given for photo-neutron production is T(γ,n)R, meaning that an x-ray or other energetic photon, γ, collides and interacts with a target nucleus, T, producing a neutron, n, and leaving behind nucleus R. The representation of a photo-neutron interaction without concern for the

nuclei involved is given within the parentheses, (γ,n). Photo-neutrons are not only produced within the linac's head, but can also be produced in the patient's body [Paredes et al., 1999].

Since neutrons are uncharged, they do not interact with the electrons in tissue. Instead, they can interact elastically with the hydrogen nuclei (protons) of the tissue molecules causing the protons to recoil [IARC, 2000]. In tissue, 70 to 85% of the energy in high energy ($\geq$ 1 MeV) neutron interactions is transferred to recoil hydrogen nuclei [NATO, 1996]. These recoiling nuclei (charged protons) are the source of ionizing events. Low energy protons, with linear energy transfer (LET) up to $\sim$ 100 keV/μm produced in neutron interactions, form densely ionizing tracks which are efficient in producing biological damage in cells [IARC, 2000]. As the neutrons undergo elastic collisions, they lose most of their energy and thermalize. Once thermalized, the neutron can be captured or absorbed by a nucleus. This results in an unstable nucleus, or compound nucleus that will rapidly decay, releasing more energy into the tissue.

Neutrons, because they do not possess a charge, can travel further in a medium than charged particles of similar energy. This results in a high probability of neutrons depositing dose in a non-targeted region of the body. For example, if a patient is being treated for prostate cancer, a scattered neutron could deposit dose to the patient's lungs, heart, brain, or other vital organ despite the fact that none of these organs receive direct x-ray radiation. Once inside the patient's body neutrons can scatter through multiple collisions with hydrogen nuclei. The average distance, or mean free path, that the neutron can travel is dependent upon the neutron's energy, the interaction cross section, and the density of the material, and can vary from a fraction of a cm to several tens of centimetres [IARC, 2000]. Although the absorbed dose deposited through neutron-induced secondaries in the patient is clinically much too low to induce any early radiation effects, it could lead to health problems, such as secondary cancer, later in the patient's life [IARC, 2000].

1.2 Late Effects From Neutron Exposure

Photo-neutrons produced in the linac or within the patient's body itself, can produce biological damage, both in the region covered by the primary x-ray beam and outside this treatment region. These neutrons can deposit unwanted dose randomly, or stochastically, throughout the patient's body. These effects usually take the form of genetic changes (changes to DNA) which can ultimately manifest themselves as a cancer. These stochastic effects tend to show up years after exposure. The probability that cancer will occur is dependent upon the dose to a patient. The greater the dose a patient receives the greater the probability of an effect. However, because stochastic effects are random, it is not guaranteed that, due to unwanted neutron exposure, a secondary cancer will occur. One must keep in mind that, because stochastic effects can affect anyone, even those who have not received radiation above background levels, a specific cancer cannot be traced back to a specific event or time. While it is impossible to determine the cause of a specific cancer, it is possible to estimate the probability that exposure to radiation will lead to cancer.

The International Agency on Research for Cancer (IARC) [IARC, 2000] has conducted various studies involving a range of absorbed dose and dose rates over a wide range of mean energy from many sources to determine the probability of stochastic effects in mice, rats, rabbits, dogs, and rhesus monkeys. In one such study, involving both x-rays and neutrons, Broerse et al. [1981], preformed full body irradiations on rhesus monkeys. A total of 20 monkeys were irradiated with x-rays of doses of 2800-8600 mGy, and 9 monkeys were irradiated with neutrons at doses of 2300-4400 mGy. 21 monkeys were part of the control group that was not irradiated. Monkeys exposed to x-rays or neutrons experienced a significant increase in the incidence of malignant tumours compared to the non-irradiated controls. 90% (8/9) of the neutron irradiated animals died of complications resulting in malignant tumours compared to 50% (10/20) of animals exposed to x-rays and 30% (7/21) of unexposed animals.

The effect on patients from photo-neutron exposure during x-ray therapy is still poorly understood. This is largely due to the challenges of measuring neutrons due to their neutral charge and to the fact that neutrons are in a mixed radiation field. Due in part to this complexity, the total absorbed dose from photo-neutrons from clinical linear accelerators are not calculated during treatment planning. However, studies have been performed, such as the IARC study mentioned above [IARC, 2000], that show a strong correlation between neutron exposure and secondary cancers. This makes it important to quantify the absorbed dose from neutrons, especially to healthy tissue surrounding the treatment volume, during x-ray radiotherapy. In addition, if neutron dose is deemed excessive, steps should be taken to minimize the dose contribution to the patient from photo-neutrons.

1.3 Purpose and Intent

The professional literature available on photo-neutron production in medical linear accelerators is limited. The aim of this present work is to measure the neutron dose equivalent produced by x-ray beams of 6, 10, and 18 MV_p, in air and also in a polyethylene phantom. The experiment attempted to simulate actual patient treatment with MV_p x-rays.

The main type of radiation detector used in this work was CR-39 plastic nuclear track detector (PNTD). CR-39 is an unique detector used to help quantify the neutron dose. The advantages of using CR-39 PNTD over other detectors are: 1) it is small enough to place anywhere inside a phantom to obtain measurements inside a body and 2) it is insensitive to x-rays thus making CR-39 PNTD an optimal choice in measuring neutrons in a mixed radiation field dominated by energetic x-rays.

In this study, two sets of experiments were conducted to measure photo-neutron production in medical linear accelerators. The first set of experiments measured absorbed dose and dose equivalent from 1-20 MeV neutrons and used regular CR-

39 PNTDs. The second experiment measured absorbed dose and dose equivalent from neutrons with energies lower than 1 MeV and used CR-39 PNTD modified with cadmium and ^{6}Li, so called thermal and resonance neutron detectors or TRNDs, as discussed further in Chapter 3.

The first part of this work provides a basic overview of radiation therapy, photoneutron production, and neutron interaction cross sections, along with properties of CR-39 PNTDs, nuclear track formation and dosimetric quantities.

CHAPTER 2

PHOTO-NEUTRONS

2.1 Radiotherapy

Radiation therapy, also known as radiotherapy, refers to the treatment of cancerous cells by ionizing radiation. The goal of radiotherapy is to deliver a high dose of ionizing radiation to the cancerous cells of a tumor, in order to kill those cells, while minimizing the radiation delivered to healthy cells surrounding the tumor. Radiotherapy is one of two the most reliable and effective treatments for cancer, with more than fifty percent of cancer patients having received radiotherapy at some point in their treatment [Joiner and van der Kogel, 2009]. Surgery is the other primary form of effective treatment and has a great success rate when preformed at an earlier stage before cancer has metastasized [Mukherjee, 2011]. In some locations on or within the body, such as in the head, neck, lung, cervix, bladder, prostate, and skin, radiotherapy is a good alternative to surgery due to its better long term control, fewer side effects, and better cosmetic results [Joiner and van der Kogel, 2009]. In addition, radiotherapy helps mitigate the severity of the effects of having cancer by reducing pain and helping the overall morale of the patient.

Chemotherapy is another important treatment modality for cancer therapy in which a mixture of chemicals (drugs) is used to kill rapidly dividing cells. Rapid cell division is one property that distinguishes cancer cells from most normal cell types [Cooper and Hausman, 2009]. Since chemotherapy cannot distinguish between rapidly dividing cancerous cells and rapidly dividing healthy cells, chemotherapy harms both cancerous and healthy cells. These healthy cells include those of the bone marrow,

digestive tract, and hair follicles.

Table 2.1 shows the percent of patients receiving radiotherapy as a principal form of treatment, as well as the percent of patients with all types of cancers who received radiotherapy at some stage of treatment.

Table 2.1 Optimal radiotherapy utilization rate by cancer type. [Delaney et al., 2005]

Tumour Type	**Proportion of all Cancers (%)**	**Proportion of patients receiving radiotherapy (%)**	**Patients receiving radiotherapy (% of all cancers)**
Breast	13	83	10.8
Lung	10	76	7.6
Melanoma	11	23	2.5
Prostate	12	60	7.2
Gynaecological	5	35	1.8
Colon	9	14	3.1
Rectum	5	61	3.1
Head and neck	4	78	3.1
Gall bladder	1	13	0.1
Liver	1	0	0.0
Oesophageal	1	80	0.8
Stomach	2	68	1.4
Pancreas	2	57	1.1
Lymphoma	4	65	2.6
Leukaemia	3	4	0.1
Myeloma	1	38	0.4
Central nervous system	2	92	1.8
Renal	3	27	0.8
Bladder	3	58	1.7
Testis	1	49	0.5
Thyroid	1	10	0.1
Unknown primary	4	61	2.4
Other	2	50	1.0
Total	100	-	52.3

Calculations by DeVita et al. and Souhami and Tobias [DeVita et al., 1979; Souhami and Tobias, 1986; Tobias, 1996], who analysed data on the relative roles of the main cancer treatment modalities from national cancer programs, suggest that surgery

and/or radiotherapy are successful in roughly 40% of patient cases. 15% of these cases are radiotherapy alone.

The cure rate from chemotherapy is about seven times smaller than that of radiotherapy; with about 10 percent of patients having prolongation of life [Joiner and van der Kogel, 2009]. Chemotherapy, as well as surgery, is often combined with radiotherapy, depending on the severity of the cancer, tumor location, patient age, and the development and general health of the patient.

2.2 Design of a Medical Linear Accelerator (Linac)

The medical linear accelerator (linac) uses high frequency electromagnetic waves to accelerate electrons to high energies (4-25 MeV) through a linear accelerator waveguide. Figure 2.1 shows a block diagram of a typical medical linac.

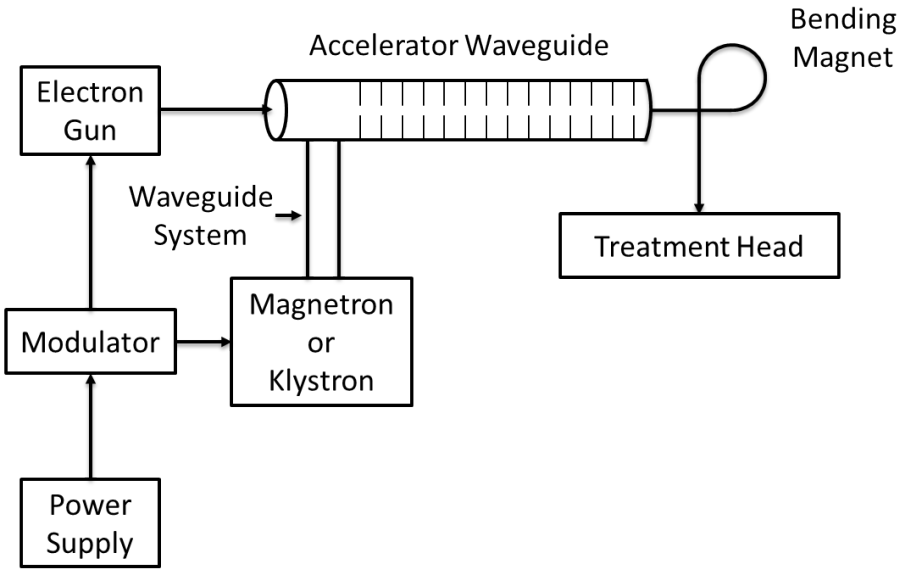

Figure 2.1 A block diagram of a typical medical linac, adapted from [Khan, 2003].

A linac produces electrons from an electron gun situated at one end of the linear accelerator waveguide. The acceleration of electrons is caused by pulsed microwaves produced by a magnetron or klystron, and propagated down a waveguide system in

the accelerator. In order for electrons to be accelerated efficiently, the magnetron or klystron, electron gun, and wave guide system must be under vacuum.

2.2.1 Electron Gun

The source of electrons is an electron gun. At one end of the electron gun is a cathode and at the other end an anode. The cathode is made out of a tungsten filament which when heated boils off electrons. This process is called thermionic emission. When high voltage is applied between the cathode and anode the electrons emitted from the tungsten filament are accelerated in the direction of the anode. The electron gun in linacs uses this process to produce a beam of $\sim$ 50 keV electrons. The anode is situated at the opening of the accelerating waveguide, which allows the electrons to travel through the anode and into the accelerator waveguide.

2.2.2 Magnetron/Klystron

Once inside the linac waveguide, the electromagnetic field of the pulsed microwaves filling the waveguide's cavities transfers its energy to the electrons causing them to accelerate. This electromagnetic field in the form of microwave radiation is produced by a Radio Frequency (RF) oscillator in the form of a magnetron or by a klystron [Podgorsak, 2003].

The magnetron is a source of high power RF waves, while the klystron is an RF power amplifier [Khan, 2003]. A RF driver or an RF oscillator which produces a low power radio frequency needs to accompany the klystron.

2.2.3 Waveguide System

Waveguides are rectangular or cylindrical metallic structures used in the transmission of microwaves [Podgorsak, 2003]. In linacs, two waveguides are used: RF power transmission waveguides, and accelerating waveguides. The RF power transmission

waveguide transmits RF power from the magnetron or klystron to the accelerating waveguide, which accelerates the electrons.

The accelerating waveguide is a cylindrical structure containing a series of disks forming cavities with circular holes at the center and placed at equal distances along the waveguide. The traveling wave structure and the standing wave structure are the two types of accelerating waveguides used in linacs.

Traveling Wave Structure

In the traveling wave structure, a traveling wave is produced where the electric field passes through the accelerator waveguide and the electrons "ride" the wave as shown in Figure 2.2. The cavity geometry and the size of the hole separating the cavities determine the speed of the wave in the waveguide. The first few cavities are smaller and have larger holes. This allows the beam to be bunched and accelerated to relativistic velocities. In the remainder of the accelerator, the energy continues increasing the electron's relativistic mass so that the cavities are uniform [Greene and Williams, 1997].

Standing Wave Structure

In the standing wave structure, a standing wave is made by the superposition of the forward traveling wave and its reflected image. The force experienced by the electron is the same as that in the traveling wave structure, however, the field is zero where there are nodes. If the cavities are tuned so that the electrons can cross one whole cavity at a time, a constant acceleration can be applied.

The geometry of the traveling wave structure is inefficient when compared to the standing wave structure, because only every second cavity contributes to the acceleration of the electrons. However every other cavity can be moved to produce a side couple design as shown in Figure 2.3. The microwaves will pass through all of the

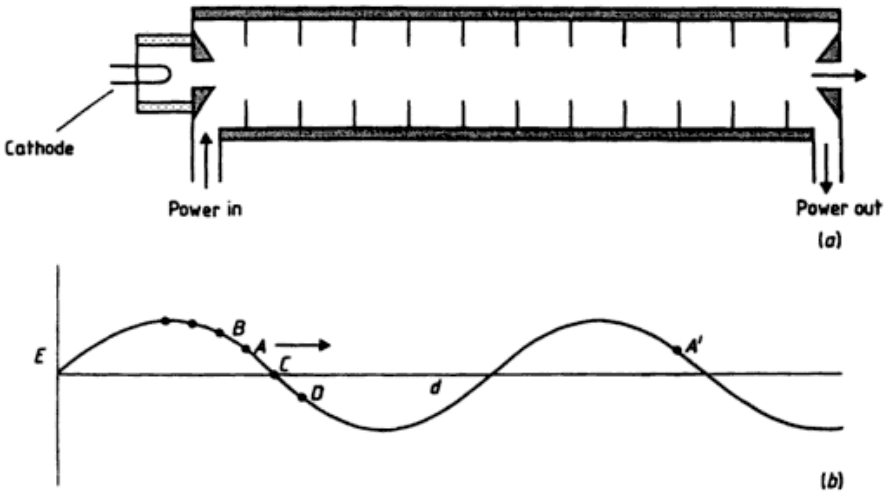

Figure 2.2 (a) A traveling wave accelerator. (b) A traveling wave respresenting the axial electric field. E is the electric field strength and d is the distance along the axis. Points A-D indicate positions of electrons on the wave. [Greene and Williams, 1997]

cavities while the electrons pass only through the central ones.

Using this design, the microwave intensity is uniform across the entire length of the accelerator waveguide. Due to this, the standing wave accelerator gives a higher acceleration per unit length, leading to a shorter accelerator compared to the traveling wave structure for a given maximum electron energy. However, as the power is uniform down the waveguide, it requires a higher power microwave magnetron or klystron to drive it for a given electron energy [Greene and Williams, 1997].

Electrons in both accelerator types experience forces during acceleration that tend to cause divergence of the beam. Focus coils that run along the length of the accelerator waveguide are added to prevent divergence of the beam. Steering coils are also placed at the exit of the accelerating waveguide to make sure the beam is traveling in the desired direction

The length of the accelerating waveguide depends on the final electron kinetic

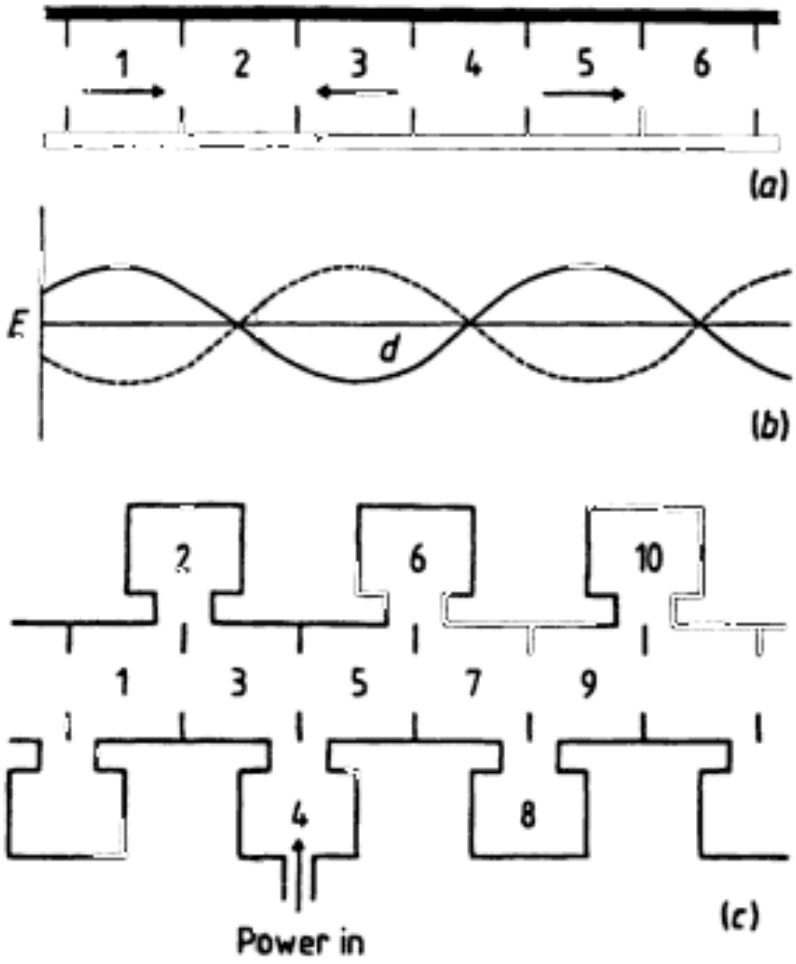

Figure 2.3 (a) A standing wave accelerator. (b) Standing waves, the dotted line representing the field one half cycle after the field shown by the solid line. (c) Side coupled cavities [Greene and Williams, 1997].

energy and ranges from $\sim$ 30 cm at 4 MeV to $\sim$ 150 cm at 25 MeV [Podgorsak, 2003]. The electron beam exits the accelerator waveguide in the form of a pencil beam of about 3 mm in diameter [Khan, 2003] and will not be completely monoenergetic.

2.2.4 Bending Magnets

The accelerating waveguide is usually mounted perpendicular to the treatment head and the electron beam must be redirected. One method to accomplish this is to use a uniform magnetic field. However, because the radius of curvature of the electron in the magnetic field is dependent upon electron energy, the electrons will tend to disperse given the distribution of electron energies.

To obtain an electron beam of uniform energy, a 270° magnetic bending system is used (Figure 2.4). These bending magnets use shaped pole faces that produce a magnetic field which grows in strength as the radial distance from the beam increases. More energetic electrons penetrate further into the bending magnet's field and are then subjected to a stronger magnetic field resulting in a tighter radius of curvature [Greene and Williams, 1997]. Collimators can be placed within the bending magnet's field as shown in Figure 2.4 to remove electrons that have higher or lower energies than that desired. This will then create an electron beam of uniform energy passing through the same point and moving in the same direction.

2.2.5 Treatment Head

The uniform electron beam is then passed to the treatment head of the linear accelerator. The treatment head consists of a thick shell of high density shielding material such as lead, tungsten, or lead-tungsten alloy [Khan, 2003]. It contains the x-ray target, both fixed and movable collimators, scattering foils, and flattening filters.

Once inside the treatment head, the electron beam is converted to bremsstrahlung x-rays by colliding with an x-ray target in the treatment head as shown in Figure 2.5.

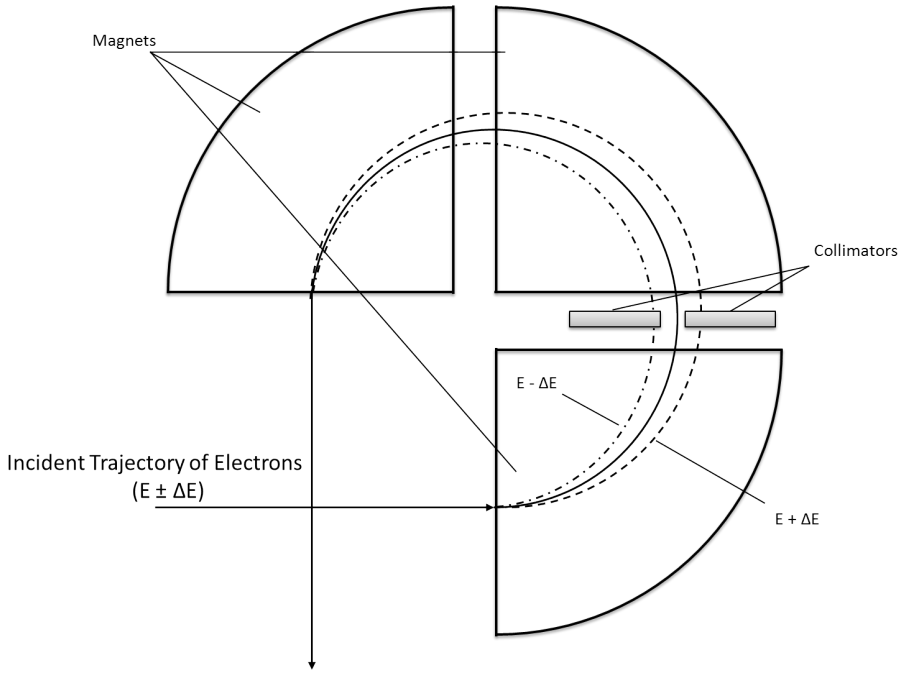

Figure 2.4 Diagram of a 270° bending magnet.

The x-ray target must be made out of a material with high atomic number and high melting point. Tungsten, with a Z of 74 and a melting point of 3,370°C is conventionally used.

The electron energy is converted into a spectrum of x-ray energies with the maximum energy equal to the incident electron energy. The average x-ray energy of the beam is approximately one third of the maximum energy [Khan, 2003].

2.2.6 Primary Collimators

The x-rays produced are immediately collimated by the fixed primary collimator. This collimator absorbs all but the x-rays traveling in the desired direction. The beam is then subject to further modifications by a flattening filters, secondary collimators, a mulitleaf collimator (MLC), and/or wedges, blocks, or compensators.

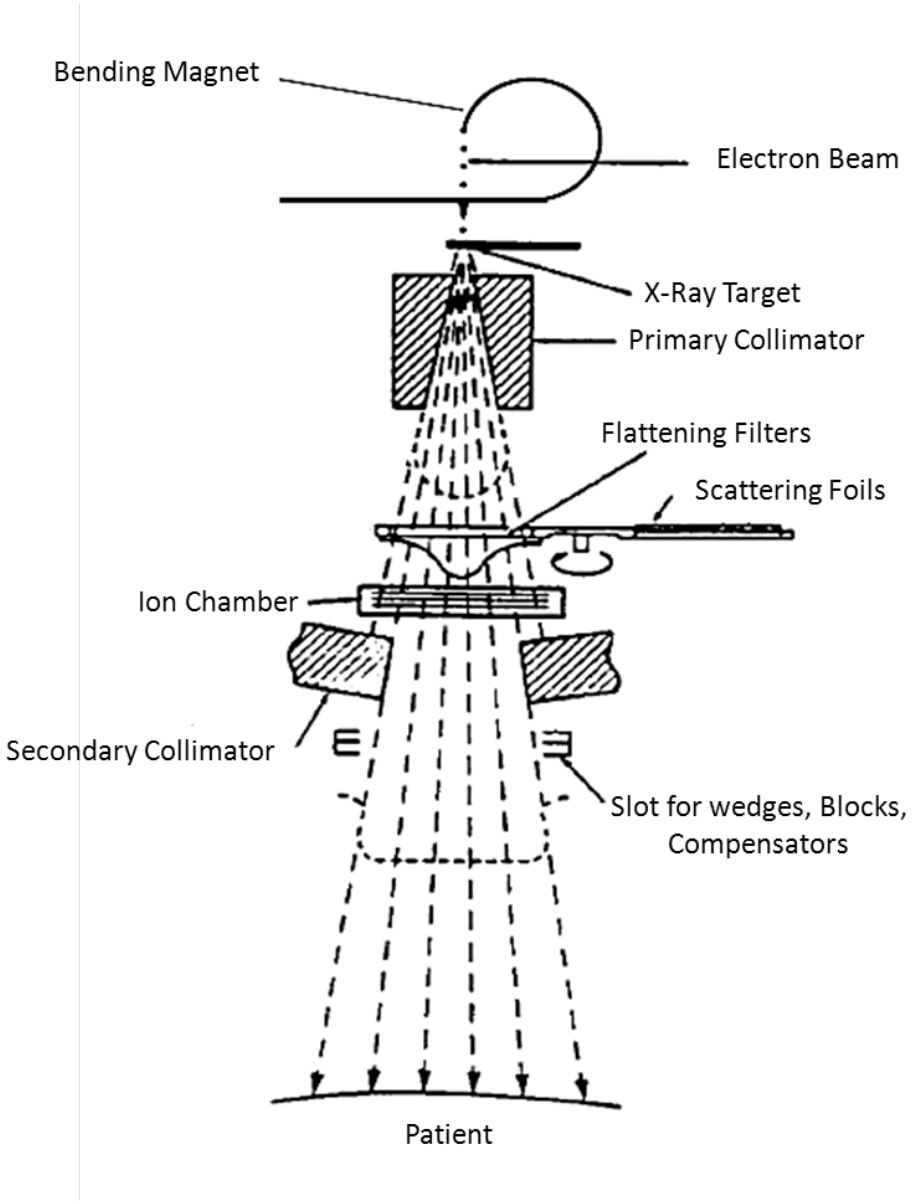

Figure 2.5 Components of a treatment head from a typical medical linear accelerator [Khan, 2003].

2.2.7 Flattening Filters

When the electron beam collides with the tungsten target, the x-ray intensity is peaked in the forward direction. This is because of the angular distribution of x-rays produced by electrons in the megavoltage range [Khan, 2003]. To make the x-ray beam intensity uniform across the field, a flattening filter is inserted in the beam. Flattening filters are commonly made out of lead, however tungsten can also be used.

2.2.8 Secondary Collimators

Secondary collimation is used after the flattening filter. These collimators are movable and consist of two pairs of lead or tungsten blocks (jaws). The purpose of the jaws is to provide a rectangular opening from 0 x 0 cm to the maximum field size as projected at a standard distance 100 cm from the x-ray source.

MLCs can also be used to provide direct shaping of the x-ray beam to match the contour of the cancer tumor itself. An MLC is a collimation system made up of individual "leaves" made out of high Z materials, usually tungsten, which can move independently in and out of the x-ray beam. MLCs are now widely used and have become a main component in beam shaping in external beam radiotherapy [Jeraj and Vlado, 2004].

2.3 Cross Section

The probability of a particular outcome occurring from an interaction between a particle and nucleus is defined by its interaction cross section, σ. Cross section has dimensions of area with units of cm^2. However, in nuclear physics cross sections are often given in units of barns, b, where $1b = 10^{-24}$ cm^2. Cross sections for most nuclear interactions are on the order of 0.001 to 1000b. The cross section of a given interaction is dependent on the incident particle's energy. A general rule of thumb

is that with increasing energy of the incident particle, the cross section will decrease [Rinard, 1991].

2.4 Photo-Neutron Production

Photon interaction with matter can result in various outcomes. These different outcomes can be classified according to the target with which the photon interacts, such as electrons, atoms, or nuclei, and the type of event which takes place, i.e. scattering or absorption. Table 2.2 shows some of the possible interactions that may occur.

Table 2.2 Various categories of photon interactions [Hirayama, 2000].

Total		
Scattering		**Absorption**
Elastic	Inelastic	
Rayleigh	Compton	Photoelectric effect
Elastic Nuclear	Inelastic nuclear	Photonuclear reaction
		Pair production

Photo-neutrons are produced through photonuclear reactions called photo-disintegration [Khan, 2003]. Photo-disintegration occurs when a nucleus absorbs a high energy photon, leading the absorbing nucleus to undergo internal rearrangement and the ejection of one or more subatomic particles, such as a protons, neutrons, or alpha particles. This process is known as evaporation [NBS, 1982]. Most photo-neutrons (80-90 %) are produced through the evaporation process following resonance in heavy nuclei [IAEA, 1979]. Evaporation neutrons are emitted isotropically and have average energies ranging from 1-2 MeV [NCRP, 2005].

Photo-neutrons can also be emitted from a process called direct emission [NBS, 1982]. Direct emission is when a high energy particle e.g. photon, interacts directly with

one or more individual nucleons (neutrons) inside a nucleus. Direct emission neutrons have average energies of several MeVs. The angular distribution of direct neutrons follows a $\sin^2\theta$ distribution [NCRP, 2005]. Direct emission neutron production for 15-30 MeV x-rays interacting with heavier nuclei is ∼10-20 % [IAEA, 1979].

Photo-neutron production (γ,n) is dependent upon the photo-neutron cross section and the binding energy. The binding energy of a nucleus is the difference in the total energy of the bound system (the nucleus) and the combined energy of the separate nucleons. In other words binding energy is the energy that must be added to a nucleus to break it apart into its component nucleons [Serway et al., 2005]. The minimum energy required to overcome the binding energy is called the threshold energy, E_{th}. In photo-neutron production, the added energy obviously is in the form of an incident x-ray photon. The photo-neutron threshold energies for a variety of elements and isotopes are shown in Table 2.3. These elements and isotopes represent those that make up the human body (^{12}C, ^{14}N, and ^{16}O), air (^{14}N, and ^{16}O) and the treatment head of the linac, (^{206}Pb, ^{207}Pb, ^{208}Pb, and ^{186}W).

Table 2.3 shows that photo-neutrons can be created with photon energies as low as ∼7 MeV for higher Z materials such as tungsten and lead. Other elements such as carbon, nitrogen, and oxygen require higher energies, ∼ 19, 11, 16 MeV, respectively, to undergo (γ,n) interactions.

When a photo-neutron interaction occurs, one or more neutrons can be produced depending upon the photon energy and the photo-neutron cross section. The total photo-neutron cross section is the sum of $\sigma(\gamma,n)$, $\sigma(\gamma,2n)$, $\sigma(\gamma,3n)$ ... etc:

$$\sum_{i=1}^{\infty} \sigma(\gamma, in). \tag{2.1}$$

The photo-neutron cross section, (γ, in), for ^{12}C, ^{14}N, ^{16}O, ^{206}Pb, ^{207}Pb, ^{208}Pb, and ^{186}W are shown in Figures 2.6, and 2.7. These curves follow a Poision or Lorentz distribution, where at higher energies the cross section will reach a peak or multiple

Table 2.3 Threshold energies of different elements/isotopes for (γ,n), (γ,2n), and (γ,3n) interactions [Berman, 1975].

Element	**(γ,n) Threshold** (MeV)	**(γ,2n) Threshold** (MeV)	**(γ,3n) Threshold** (MeV)
^{12}C	18.72	31.83	-
^{14}N	10.56	-	-
^{16}O	15.72	-	-
^{206}Pb	8.05	14.79	23.02
^{207}Pb	6.75	14.79	21.62
^{208}Pb	7.31	22.24	22.24
^{186}W	7.22	12.94	20.41

peaks. These peaks are called resonances and occur at photon energies where reactions with the nuclei are enhanced. If the resonance peak is broad and the incident photon energy is located near the resonance peak, the probability that a neutron will be emitted is large.

In Figure 2.6, the cross sections for ^{206}Pb, ^{207}Pb, ^{208}Pb, and ^{186}W show photo-neutron production beginning at x-ray energies above 8.05, 6.75, 7.31, 7.22 MeV, respectively. The resonance peaks in ^{206}Pb, ^{207}Pb, ^{208}Pb, and ^{186}W start to form around 10 MeV and continue until 18 MeV. The highest cross section values measured are 531, 505, 518, and 406 b, respectively, and occur at photon energies between 12 and 16 MeV.

The cross section data for ^{12}C, ^{14}N, and ^{16}O, in Figure 2.7, show that for these three isotopes, neutron production begins at $\sim$18, $\sim$10, $\sim$15 MeV, respectively. As the x-ray energy increases to about 22-26 MeV, a resonance peak is reached in all three isotopes. The highest cross section values measured for ^{12}C, ^{14}N, and ^{16}O are 7,

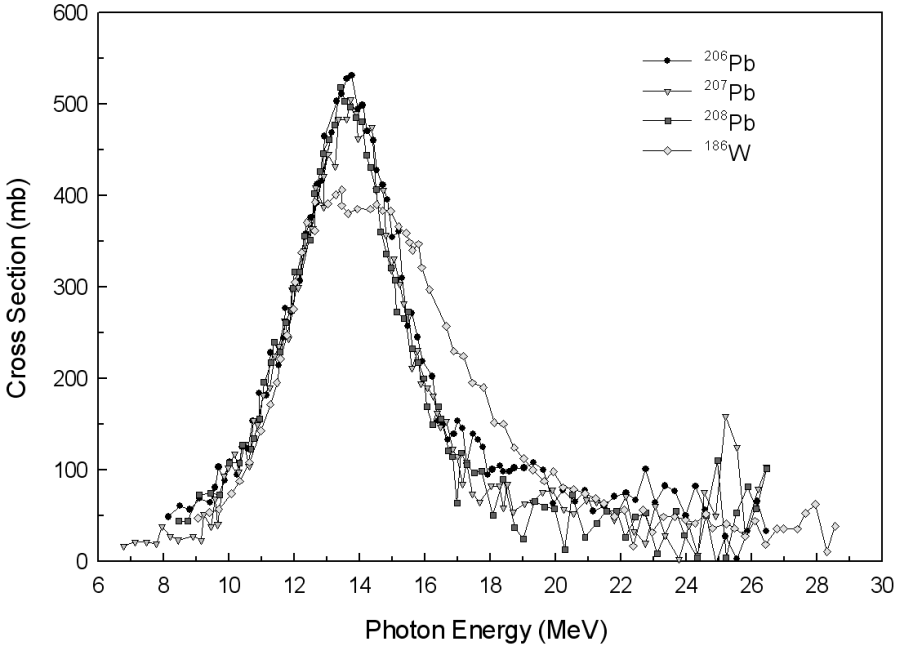

Figure 2.6 Photo-neutron cross section of ^{186}W, ^{206}Pb, ^{207}Pb, and ^{208}Pb found in the treatment head of the linac [Berman, 1975].

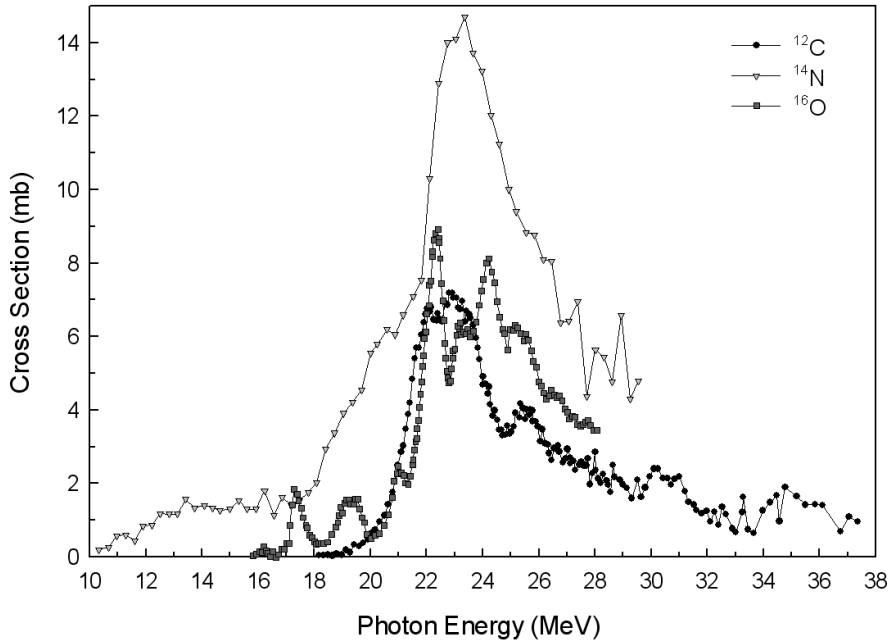

Figure 2.7 Photo-neutron cross section of ^{12}C, ^{14}N, and ^{16}O found in the air and the human body [Berman, 1975].

15, and 9 b, respectively.

Once the interaction threshold is overcome, neutrons emerge with kinetic energies which can be calculated by:

$$E_n = h\nu - E_{th}, \tag{2.2}$$

and have velocities of:

$$v_n = \left(\frac{2E_n}{m_n}\right)^{\frac{1}{2}}, \tag{2.3}$$

where E_n is the energy of the emitted neutron, E_{th} is the threshold energy, and m_n is the mass of the neutron. Table 2.4 shows the maximum energies of the emerging neutron as determined by equation (2.2). One must remember that photo-neutrons will have a broad range of energies and that Table 2.4 shows only the maximum energy that the incident photo-neutron can possess.

Table 2.4 Maximum kinetic energies of photo-neutron, of (γ,n) interactions, from energies of incident photons of 6, 10, 18, MeV.

Elements	**Photon Energy (MeV)**		
	6	**10**	**18**
^{12}C	-	-	-
^{14}N	-	-	7.44
^{16}O	-	-	2.28
^{206}Pb	-	1.95	9.95
^{207}Pb	-	3.25	11.25
^{208}Pb	-	2.69	10.69
^{186}W	-	2.78	10.78

2.5 Neutron Interaction with Matter

As uncharged particles, neutrons are unaffected by the Coulomb barrier of nuclei [Krane, 1988]. Most neutrons when traveling through matter do not interact with it at all. Those neutron that do interact with matter will do so with the nuclei of the atoms. In general, the cross section for neutron interactions increases as the neutron energy decreases.

A neutron interaction with a nucleus can result in many different outcomes as shown in Table 2.5. The possible results from a neutron interacting with different materials can be classified into two major categories: scattering and absorption.

Table 2.5 Various categories of neutron interaction. [Rinard, 1991]

Total	
Scattering	**Absorption**
Elastic	Electro-Magnetic
Inelastic	Charged
	Neutral
	Fission

2.5.1 Scattering

A neutron reaction is written as X(n,b)Y where X is the target nuclei, n is the projectile neutron, and Y and b are the reaction products [Krane, 1988]. If the outgoing particle is a neutron and the target and reaction nuclei are the same, the reaction is a scattering reaction. Scattering interactions are further divided into two categories: elastic and inelastic. In elastic scattering, the incident neutron is scattered by a target nucleus changing the direction and speed of the incident neutron. In this process, the target nucleus remains intact and the total kinetic energy of the system is conserved.

In inelastic scattering, the kinetic energy of the neutron and target nucleus after the collision is always less than the kinetic energy before the collision, therefore kinetic energy is not conserved [Rinard, 1991]. This is due to target nucleus undergoing an internal rearrangement which leaves it in an excited state. The excited nucleus will de-excite through the emission of photons or other secondary particles, in what is called an evaporation process (Figure 2.8). If the neutron energy is lower than the energy required to elevate a nucleus into an excited state, inelastic scattering will not occur.

2.5.2 Absorption

In the absorption process an indecent neutron is absorbed or captured by the target nucleus and a compound nucleus is formed. This new compound nucleus will usually decay into a lower energy state by emitting a variety of particles. These particles can include gamma-rays due to the excitation of the nucleus, neutral particles where one or more neutron is emitted, charged particles such as protons, deuterons, alpha particles, and even fission fragments where the nucleus splits into two or more fragments releasing a number of neutrons in the process [Rinard, 1991].

2.5.3 Target Fragmentation

Target fragmentation is the breaking up of target nucleus through interaction with an incident neutron, proton or other subatomic particle. A target fragmentation event can result in a number of different scenarios depending on the kinetic energy of the incident neutron and the proximity of the interaction [Goldhaber and Heckman, 1978]. Figure 2.8 illustrates target fragmentation where in a neutron collides with a target nucleus.

Target fragmentation can occur when a high energy neutron interacts with a nucleus. The incident neutron interacts with individual nucleons within the target

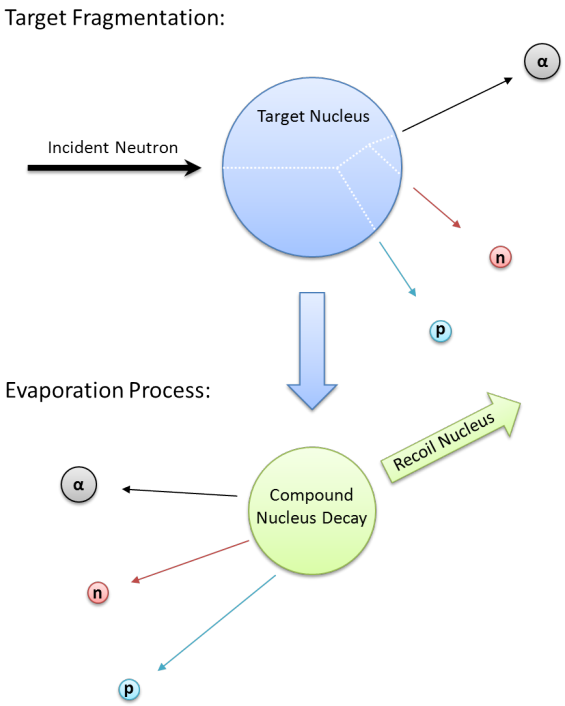

Figure 2.8 Diagram of the target fragmentation and evaporation processes.

nucleus, kicking out protons, neutrons, α particles, and other heavy nuclei ($Z \geq 3$) in a process known as an intranuclear cascade [Benton, 2004]. The emission of these nucleons is usually in the same direction as the incident neutron. After the nucleons are kicked out of the target nucleus, the target nucleus, is in an unstable excited state analogous to a compound nucleus [Benton, 2004]. This residual nucleus achieves stability by evaporating neutrons, protons, and alpha particles. The emitted particles due to evaporation are isotropic.

Each type of event mentioned above has its own cross section. These cross sections are independent of one another making the total probability the sum of each individual cross section [Rinard, 1991]. Table 2.6 shows the notation and a description for the individual cross section of these various types of interactions.

Table 2.6 Notations and descriptions for various cross sections [Rinard, 1991]

Notation		Description
σ_t	=	Total cross section (σ_s + σ_a)
σ_s	=	Total scattering cross section (σ_{el} + σ_i)
σ_{el} or $\sigma_{n,n}$	=	Elastic scattering cross section
σ_i or $\sigma_{n,n'}$	=	Inelastic scattering cross section
σ_a or σ_c	=	Absorption or capture cross section
σ_{ne}	=	Non-elastic cross section (σ_t - σ_{el})
$\sigma_{n,\gamma}$	=	Radiative capture cross section
σ_f or $\sigma_{n,f}$	=	Fission cross section
$\sigma_{n,p}$	=	(n,p) reaction cross section

2.6 Neutron Interactions with Tissue

The total cross section of neutron interactions with tissue depends on the individual neutron interactions with each individual type of nucleus in tissue. The most common nuclei in tissue are hydrogen, carbon, and oxygen. High energy neutrons interact with carbon and oxygen nuclei in tissue through inelastic collisions and can result in the release of alpha particles [Howell, 2010]. These alpha particles deposit their energy into the tissue. Epithermal neutrons between the energies ∼10 keV and ∼1 MeV interact elastically with the hydrogen nuclei. The energy transferred in this process causes the proton to recoil while the incident neutron scatters off elastically, as shown in Figure 2.9. Thermal neutrons interact with tissue through the absorption process [Howell, 2010].

The most probable mechanism for neutrons to transfer energy to tissue is from elastic scattering with the hydrogen nuclei of soft tissue [Howell, 2010]. The reasons for this is that hydrogen is the most abundant element in tissue, hydrogen has a large

neutron scattering cross section, and its mass is similar to that of a neutron causing the neutron to transfer the majority of its energy during np collisions.

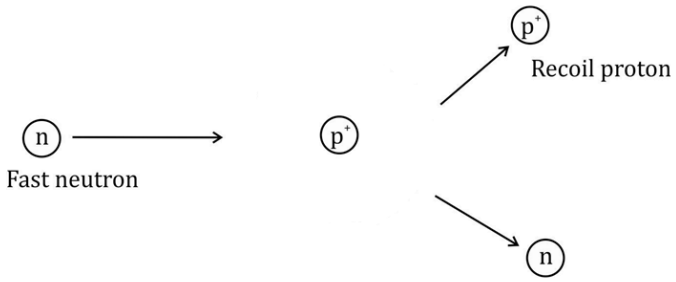

Figure 2.9 A schematic representation of neutron interaction with a hydrogen nuclei, resulting in proton recoil [Howell, 2010].

The total cross section for incident neutrons on hydrogen, carbon, and oxygen as a function of neutron energy is shown in Figure 2.10. Figure 2.10 shows that in the range of 10^{-12} to 10^{-8} MeV, elastic interactions dominate and the cross section decreases with increasing energy. In the energy range of 10^{-8} to 10^{-1} MeV, inelastic interactions dominate and the cross section is fairly constant. The peaks at about 10^{-1} to 10^{1} MeV for carbon and oxygen nuclei are resonance peaks. These resonance peaks are the result of incident neutrons elevating the target nuclei into an excited nuclear states. Hydrogen does not possess resonances, because it does not have an excited nuclear state.

The total neutron cross section of hydrogen is nearly an order of magnitude greater than that of carbon or oxygen as seen in Figure 2.10. For this reason, the hydrogen content of a material will have a large effect on neutron interactions with the material.

Figure 2.11 shows the total neutron cross section for tissue (ICRU muscle) [ICRU, 1983] along with that for CR-39 PNTDs and Polyethylene. The total cross section for these materials were calculated by using the neutron cross sections in Figure 2.10, along with the atomic compositions of these materials listed in Table 2.7.

The average neutron cross sections in Figure 2.11 are very similar to each other

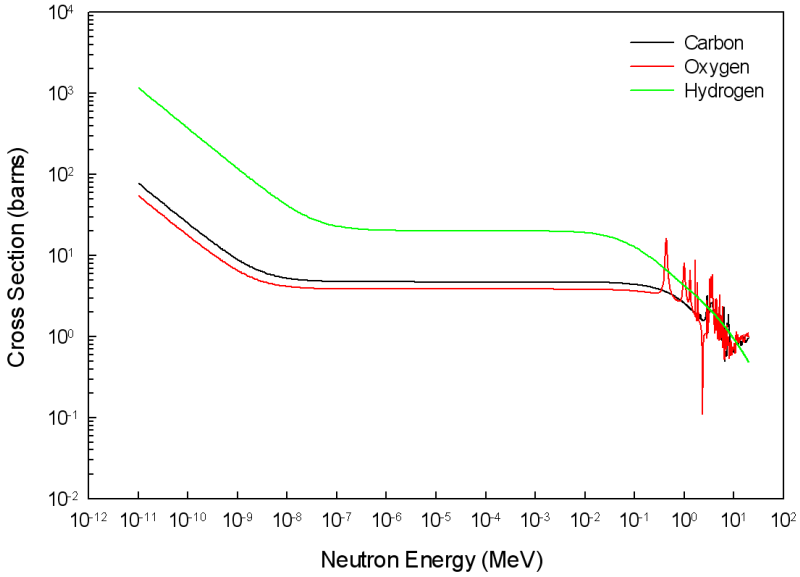

Figure 2.10 The average total cross section for neutron interaction with carbon, oxygen, and hydrogen as a function of incident neutron energy [NNDC, 2013].

for all three materials listed. Polyethylene and ICRU muscle match the closest due to their similar hydrogen content, demonstrating that a polyethylene phantom is a good approximation of a human body. Figure 2.11 also shows that although there is a slight difference in the neutron cross section for CR-39 and ICRU muscle at lower neutron energies ($< 10^{-1}$ MeV), CR-39 is a near-tissue equivalent material.

Table 2.7 The Atomic compositions in a percent of the materials used in this study (Polyethylene, and CR-39) and of ICRU muscle [ICRU, 1983].

	Atomic Percentages (%)		
Content	**ICRU Muscle**	**CR-39**	**Polyethylene**
H	63.3	48.6	66.7
C	6.4	32.4	33.3
O	28.5	19.0	-
Other	1.8	-	-

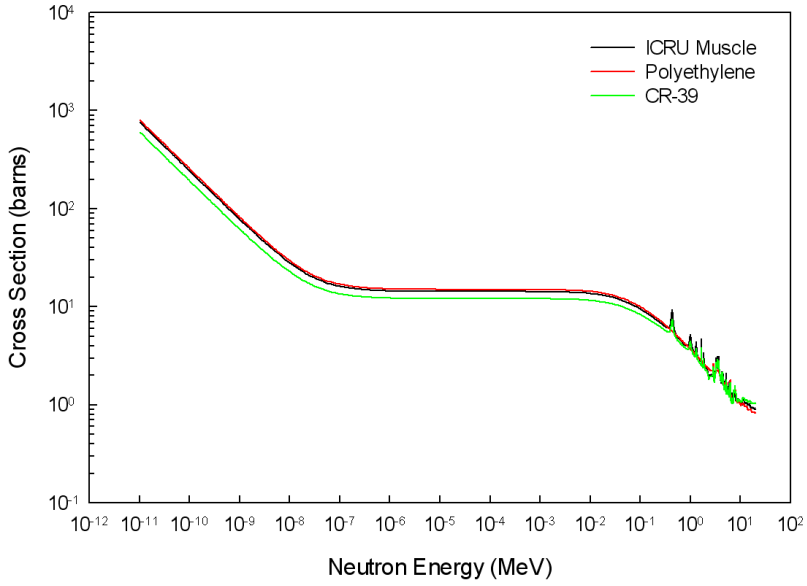

Figure 2.11 The average total cross section for neutron interaction with ICRU Muscle, Polyethylene, and CR-39 as a function of incident neutron energy [NNDC, 2013].

2.6.1 Uncertainty in Neutron Dosimetry

According to the NCRP [NCRP, 1991] the uncertainty inherit in neutron dosimetry, under ideal conditions is ± 35% with a 95% confidence level. The uncertainty in actual field measurements may be greater due to scattering, directional dependence, differences in neutron cross sections, as well as the efficiency and any intrinsic error in the instrument [[NCRP, 1991; ICRP, 1982]]. Others have reported the uncertainty in personnel neutron dosimetry to be as high as ± 50% [Sims and Killough, 1983; NRC, 1977; ANSI, 1976].

CHAPTER 3

CR-39 PLASTIC NUCLEAR TRACK DETECTOR AND THERMAL RESONANCE NEUTRON DETECTOR

3.1 Properties of CR-39 Plastic Nuclear Track Detector

CR-39 plastic nucelar track detector (PNTD) is an ideal detector for neutron dosimetry. CR-39 or polyallyldiglycol carbonate ($C_{12}H_{18}O_7$) is a thermoset crosslinked polymer, whose chemical properties make it one of the most sensitive plastic nuclear track detectors in terms of LET [Cartwright and Shirk, 1978; Cassou and Benton, 1978]. CR-39 is homogeneous, optically transparent and sensitive to charged particles of $LET_\infty H_2O$ between 5 and 1500 keV/μm, including protons $\leq$ 10 MeV, α-particles of energy $\leq$ 50 MeV and heavy ions of all energies. The chemical compositions of CR-39 PNTD ($C_{12}H_{18}O_7$) is similar to human tissue, so its response to neutrons is similar to tissue.

Neutrons with energies between 1 and 20 MeV can be detected through recoil protons produced in elastic interactions between neutrons and the hydrogen nuclei of the polymer. Neutrons can also be detected in the PNTD through recoil heavy ion tracks from non-elastic target fragmentation interactions with carbon and oxygen nuclei.

CR-39 PNTD is an ideal detector for neutron dosimetry in x-ray radiotherapy since it is insensitive to photons of all energies. Most other neutron detectors are sensitive to x-rays. For these other detectors, when placed in a high flux x-ray field, the signal from x-rays will overwhelm that produced by neutrons.

Unlike active detectors, no power is required for CR-39 PNTD operation and the

analysis is done off-site. CR-39 PNTD is also not bulky and can be placed within a phantom to measure different organ doses.

3.2 Track Formation In CR-39 Plastic Nuclear Track Detector

When a charged particle passes through a layer of CR-39 PNTD, it breaks many of the molecular bonds of the polymer along its trajectory. This damaged path through the bulk of the detector is known as a 'latent damage trail.' After exposure of the CR-39 PNTD, it is brought back to the lab and is chemically etched in a NaOH solution for a fixed amount of time. The NaOH solution will start dissolving the material of the CR-39 PNTD, reacting more with the latent damage trial than with the bulk of the material. The rate at which the alkaline solution attacks the latent damage trail is referred to as the track etch rate, V_T. The bulk etch rate, V_G, is the rate at which the alkaline solution attacks the bulk of the detector. The track etch rate and bulk etch rate are illustrated in Figure 3.1. Both V_T and V_G are measured in units of μm/hr. After the CR-39 PNTD has been etched, it is removed from the NaOH solution, after which it can be viewed with an optical microscope. A conical pit, the nuclear track, in the surface of the detector will be seen where the latent damage trail was formed. The size of the elliptical opening of the conical pit is proportional to the linear energy transfer (LET) of the particle which formed the latent damage trail. The LET is the amount of energy transferred from the ionizing particle to the material per unit path length [Benton, 2004].

The quantity of interest when measuring tracks in PNTDs is the reduced etch rate ratio, V_R. V_R is a dimensionless quantity that relates the track etch rate, V_T, to the bulk etch rate, V_G [Henke and Benton, 1971]:

$$V_R \equiv \frac{V_T}{V_G} \, . \tag{3.1}$$

For etchable tracks to be seen, $V_T > V_G$:

$$\frac{V_T}{V_G} = V_R > 1 \, .$$

The angle between the charged particle's trajectory and the side of the conical track is referred to as the cone angle, θ. The sine of θ is equal to the ratio of the bulk etch rate, V_G, to the track etch rate, V_T:

$$\sin\theta = \frac{V_G}{V_T} = \frac{1}{V_R} \, . \tag{3.2}$$

The reduced etch rate ratio, V_R, is proportional to the LET of the incident particle that formed the track. Particles with large LET displace a larger number of electrons when passing through the CR-39 PNTD than do lower LET particles. This will cause a greater number of chemical bonds to break leading to larger latent damage trails. Thus higher LET particles produce larger tracks. The cone angle, θ, is inversely proportional to the LET. A particle of low LET produces a larger cone angle, θ, and a shallower track than does a particle of larger LET.

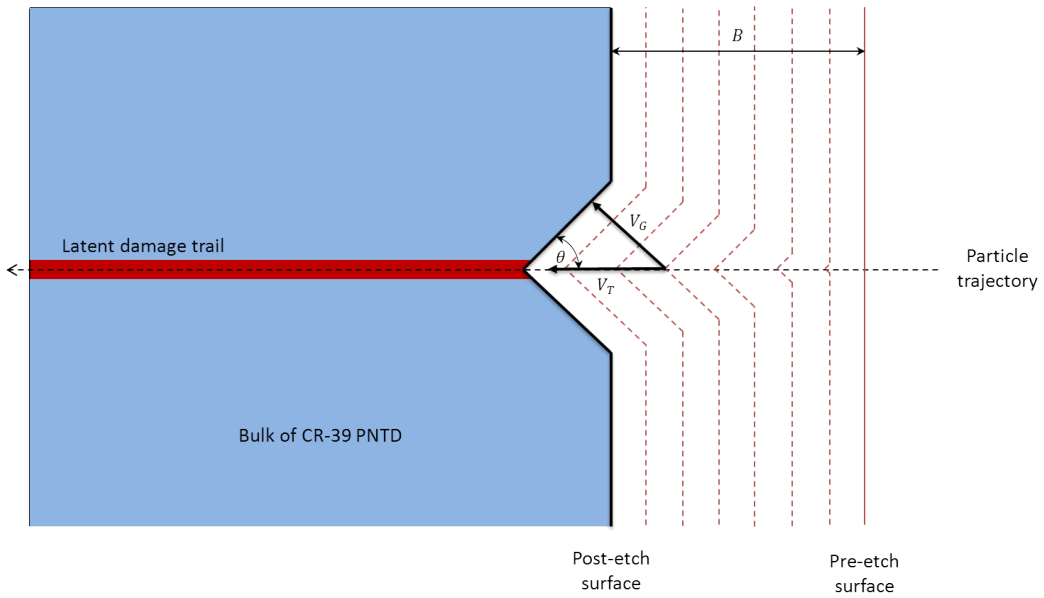

Figure 3.1 Formation of a nuclear track through chemical etching. [Benton, 2004]

3.2.1 Geometry of Nuclear Tracks

The appearance of the post etch nuclear track is that of a conical pit with a circular or elliptical opening at the surface of the PNTD. By measuring the semi-major axis, a, and semi-minor axis, b, at the surface of the PNTD, the LET of the charged particle can be determined.

The semi-major axis, a, and the semi-minor axis, b, of the elliptical opening from the conical track can be determined using three parameters: the bulk etch, B, the cone angle, θ, and the dip angle, δ, which is the angle between the trajectory of the particle and the surface of the track detector [Benton, 2004]:

$$a = \frac{B\cos\theta}{\sin\delta + \sin\theta} \,, \tag{3.3}$$

$$b = B\sqrt{\frac{\sin\delta - \sin\theta}{\sin\delta + \sin\theta}} \,. \tag{3.4}$$

Using equations, (3.3), and (3.4), the cone angle θ can be found from a, b, and B by:

$$\tan\theta = \frac{1-(b/B)^2}{2(a/B)} \,. \tag{3.5}$$

Likewise, the dip angle δ can be found by:

$$\tan\delta = \frac{1+(b/B)^2}{2\sqrt{(a/B)^2-(b/B)^2}} \,, \tag{3.6}$$

or

$$\tan\delta = \frac{(B/a)-\tan\theta}{\sqrt{1-(B/a)^2-2(B/a)\tan\theta}} \,. \tag{3.7}$$

The reduced etch rate, V_R, can be determined from a, b, and B:

$$V_R = \sqrt{1+\frac{4(a/B)^2}{[1-(b/B)^2]^2}} \,. \tag{3.8}$$

3.2.2 Determining Bulk Etch

The bulk etch, B, is the amount of material etched away from the CR-39 PNTD's surface and is usually measured in units of μm. It can be derived by integrating the bulk etch rate, V_G, with respect to time:

$$B = \int_{t_o}^{t} V_G \, dt \; . \tag{3.9}$$

The bulk etch is determined from the difference in mass of the detector due to the etching process:

$$B = \frac{(m_1 - m_2)T_2}{2m_2} \left(1 - \frac{PT_2}{2A}\right), \tag{3.10}$$

where m_1 refers to the mass before etching, m_2 to the mass after etching, T_2, to the mean thickness after etching, P to the perimeter and A to the surface area of one side of the detector [Henke et al., 1986].

3.3 Dosimetric Quantities

CR-39 PNTD, due to its tissue equivalence, has a clear advantage over many other detectors used for dosimetric measurements. To acquire a tissue equivalent absorbed dose measurement careful calibration and conversions need to be applied. As mentioned previously, the analysis of CR-39 PNTD involves measuring the semi-major axis and semi-minor axis of the etched track to calculate the LET of the charged particle that formed it. In this experiment, the charged particles that formed tracks were either proton recoils or target fragments produced in interactions with the incident photo-neutrons. The measured LET values collectively form the LET spectrum. The LET spectrum is used to calculate other dosimetric quantities such as absorbed dose and dose equivalent.

3.3.1 Fluence

From the International Commission on Radiation units and Measurement (ICRU) Report No. 60 [ICRU, 1998], fluence, Φ, is defined as the total number of particles, dN, that intersect a unit area dA.

$$\Phi = \frac{dN}{dA}. \tag{3.11}$$

For isotropic or nearly isotropic radiation fields a correction in fluence includes the solid angle, Ω:

$$\Phi = \frac{d^2N}{dAd\Omega}, \tag{3.12}$$

and is given in units of cm^{-2} sr^{-1}.

3.3.2 Absorbed Dose

Absorbed dose is the amount of energy absorbed per unit mass of a material as a result of exposure to ionizing radiation:

$$D = \frac{dE}{dm}, \tag{3.13}$$

and is measured in SI unit of Gray (Gy) where 1 Gy is 1 J/kg.

3.3.3 Linear Energy Transfer (LET)

CR-39 PNTD used in this research does not measure absorbed dose or dose equivalent directly; rather it measures the linear energy transfer (LET) of individual particle tracks. These LET values can then be used to calculate the absorbed dose. LET is the measure of energy deposited per unit distance over the path of the charged particle.

$$LET = \frac{dE}{dl}. \tag{3.14}$$

The SI unit of LET is J/m though in radiation therapy it is commonly expressed in keV/μm. LET is closely related to both the mass stopping power and the linear stopping power.

Linear stopping power is defined as the average energy loss of a charged particle per unit path length:

$$S = \frac{dE}{dx}. \tag{3.15}$$

There are three ways for energy to be lost by a charged particle traveling through a material: atomic collisions, nuclear interactions, and radiative losses, i.e. bremsstrahlung. The total linear stopping power can be written as:

$$S = \left(\frac{dE}{dx}\right)_{elec} + \left(\frac{dE}{dx}\right)_{nuc} + \left(\frac{dE}{dx}\right)_{rad}. \tag{3.16}$$

Since both LET and linear stopping power are dependant on the density of the material, mass stopping power which is independent of density is given by:

$$\frac{S}{\rho} = \frac{1}{\rho}\,\frac{dE}{dx}, \tag{3.17}$$

where ρ is the mass density of the material. The SI units for mass stopping power is J m^2/kg. However it is more commonly expressed in units of MeV cm^2/g.

In the ICRU report No. 60 [ICRU, 1998], the linear energy transfer passing through a material, also known as the linear stopping power, L_Δ, for charged particles, is denoted by:

$$L_\Delta = \frac{dE_\Delta}{dx}, \tag{3.18}$$

where dE_Δ is the energy lost by a charged particle due to electronic collisions within a distance dx, minus the sum of kinetic energies, from secondary electrons with kinetic energies greater than Δ.

The subscript Δ is usually given in units of eV and is often written as LET_Δ. Using this notation, the unrestricted linear stopping power, S, is written as LET_∞. It is important to remember that the LET and the stopping power are dependant on the material through which the charged particle travels. Thus the LET_∞ of a given charged particle of known kinetic energy will not be equal in two different materials. The common notation to distinguish between material dependence, LET_Δ, is written as LET_Δmaterial. For example, $\mathrm{LET}_\infty H_2O$, is the unrestricted linear stopping power in water, whereas LET_{200}CR-39 represents the restricted linear stopping power in CR-39 PNTD which neglects the kinetic energies of secondary electrons greater than 200 eV.

3.4 Conversion From LET To Absorbed Dose and Dose Equivalent

Using the LET distribution of the incident radiation, absorbed dose can be determined. For a monoenergetic radiation beam [Benton, 2004]:

$$D = \frac{1.602 \times 10^{-19} \Phi LET}{\rho}, \tag{3.19}$$

where the factor 1.06×10^{-19} converts keV to joules. In a mixed energy radiation beam, equation (3.19) will include the individual contributions for each particular fluence Φ_i of particles with LET_i:

$$D = \frac{1.602 \times 10^{-19}}{\rho} \sum_i \Phi_i LET_i \tag{3.20}$$

Identical absorbed doses of different types of radiation produce different amounts of damage to biological systems [Hess and Eugster, 1949]. For example, the damage

produced in a laboratory animal exposed to 1 Gy of α-particles is typically more severe than the damage produced by a 1 Gy exposure of γ-rays. Because of this, the International Commission on Radiobiological Protection (ICRP) has over the years determined a number of different quantities based on weighting absorbed dose to account for the varying LET of different types of radiation. Dose equivalent, H, is defined as the product of absorbed dose, D, multiplied by an LET-dependent quality factor, Q [ICRP, 1977]:

$$H = Q(LET)D(LET). \tag{3.21}$$

The SI unit of dose equivalent is the Sievert (Sv) where 1 Sv = 100 Rem (Rad equivalent man).

The quality factor, Q, in the Annex A of ICRP publication No. 60 [ICRP, 1991] has been defined as:

$$Q(LET) = \begin{cases} 1.0 & LET < 10 \\ 0.32LET - 2.2 & 10 \leq LET \leq 100 \\ 300/\sqrt{LET} & LET > 100\ . \end{cases} \tag{3.22}$$

3.5 Determination of Absorbed Dose and Dose Equivalent in CR-39 PNTD

The derivation of fluence, dose, and dose equivalent, from isotropic radiation incident on the surface of a CR-39 plastic nuclear track detector, can be found with the aid of the diagram shown in Figure 3.2. The figure shows a sphere of radius, r, that is centered at point, O, on the surface of the CR-39 PNTD layer. Using a spherical coordinate system, the differential area dA on the surface of the sphere can be shown as:

$$dA = 4\pi r^2 \sin\phi \, d\phi, \tag{3.23}$$

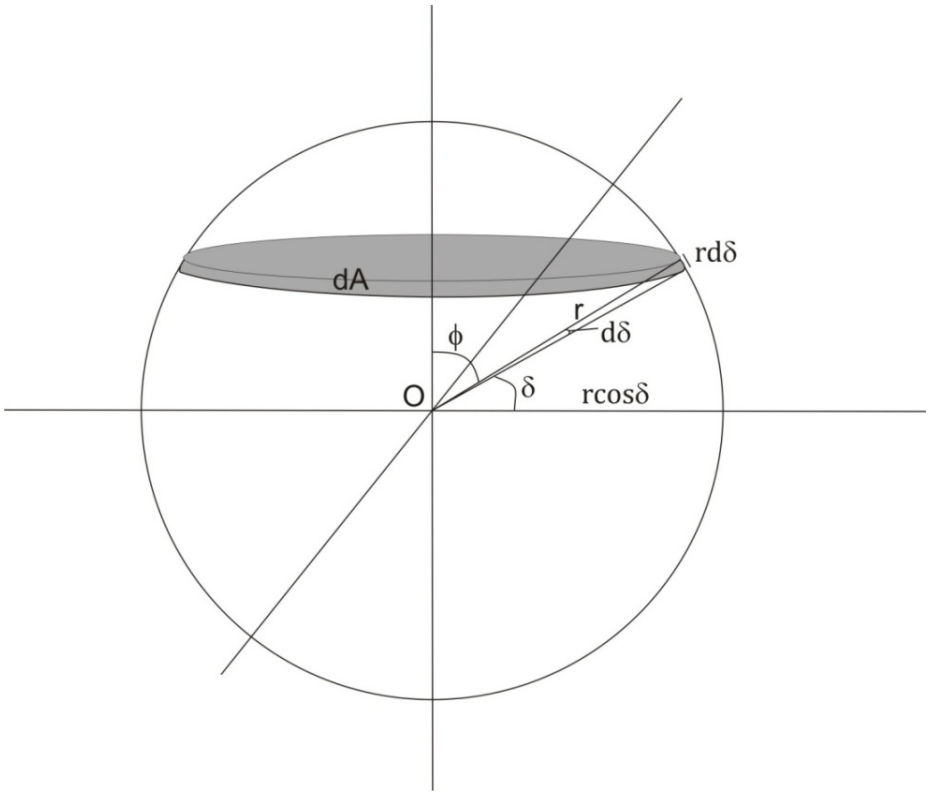

Figure 3.2 Geometry for solid angle calculation [Benton, 2004]

where ϕ is the polar angle. The factor 4π instead of 2π comes from the fact that, in isotropic fields, particles can pass through from both below and above the area dA.

The dip angle, δ, is equal to $\pi/2$ - ϕ. Thus:

$$\sin\phi = \cos\left(\frac{\pi}{2} - \phi\right) = \cos\delta \tag{3.24}$$

and

$$dA_s = 4\pi r^2 \cos\delta dr d\delta \tag{3.25}$$

By definition, the differential solid angle, $d\Omega$ is:

$$d\Omega = \frac{\vec{n}\cdot d\vec{A}}{r^2} = \frac{\cos\phi dA}{r^2}, \tag{3.26}$$

or

$$d\Omega = \frac{\sin\delta dA}{r^2}. \tag{3.27}$$

Substituting equation (3.23) into equation (3.27) gives:

$$d\Omega = 4\pi \sin\delta \cos\delta d\delta. \tag{3.28}$$

Substituting equation (3.28) into equation (3.12) and rearranging the terms gives:

$$\frac{dN}{dA} dN = \Phi 4\pi \cos\delta \sin\delta d\delta. \tag{3.29}$$

From the assumption that the distribution of neutrons is isotropic, the LET spectrum is not a function of δ and it can be integrated from δ_c to $\pi/2$, where δ_c is the critical dip angle, the minimum angle at which tracks can be produced by particles of a given LET [Benton, 2004]:

$$\frac{dN}{dA} \int dN = \Phi 4\pi \int_{\delta c}^{\frac{\pi}{2}} \cos\delta \sin\delta d\delta, \tag{3.30}$$

$$\frac{dN}{dA} = \Phi 2\pi \sin^2\delta|_{\delta_c}^{\frac{\pi}{2}}, \tag{3.31}$$

and

$$\frac{dN}{dA} = \Phi 2\pi \left(1 - \sin^2\delta_c\right). \tag{3.32}$$

Since $\cos^2\delta = 1 - \sin^2\delta$,

$$\frac{dN}{dA} = \Phi 2\pi \cos^2\delta_c. \tag{3.33}$$

Integrating this over the area, A, of the detector surface gives:

$$\int dN = \Phi 2\pi \cos^2\delta_c \int_0^A dA, \tag{3.34}$$

$$N = \Phi 2\pi A \cos^2 \delta_c, \tag{3.35}$$

or solving for Φ:

$$\Phi = \frac{1}{2\pi A \cos^2 \delta_c} \cdot N. \tag{3.36}$$

Using equation (3.36), the differential LET fluence can be written [Benton, 2004]:

$$\frac{d\Phi}{dLET} = \frac{1}{2\pi A \cos^2 \delta_c} \cdot \frac{dN}{dLET} \tag{3.37}$$

The term $1/2\pi A \cos^2 \delta_c$ is known as the weighting factor, w, and each given LET value has a specific weighting factor depending on the critical dip angle [Benton, 2004]. Considering the ith track in a set of measured tracks, the LET and the weighting factor can be written as $LET(i)$ and $W(i)$ respectively.

The differential LET fluence spectrum is found by summing each particle track of a given LET interval and multiplying that value by the average weighting factor for that particular interval:

$$\Phi(i) = N(i)\overline{W}(i), \tag{3.38}$$

where the average weighting factor, $\overline{W}(i)$, is calculated by the average value of the critical dip angle, δ_c, for a given LET interval. The units of the differential LET fluence spectrum are n/cm^2 sr. The integral LET fluence is calculated by summing $\Phi(i)$ for $LET(i) \geq LET(x)$ where $LET(x)$ is the LET value at which the integral fluence is being determined:

$$\Phi(LET(i) \geq LET(x)) = \sum_{i=max}^{x} N(i)\overline{W}(i), \tag{3.39}$$

and its units are the same as the differential LET fluence.

Given equation (3.19), the differential LET dose spectrum is:

$$D(i) = \frac{4\pi \times 1.602 \times 10^{-9}}{\rho} LET(i)N(i)\overline{W}(i), \tag{3.40}$$

and the integral LET dose spectrum is given by:

$$D(LET(i) \geq LET(x)) = \frac{4\pi \times 1.602 \times 10^{-9}}{\rho} \sum_{i=max}^{x} LET(i)N(i)\overline{W}(i), \tag{3.41}$$

where both differential LET dose spectrum and integral LET dose spectrum are given in units of Gy. The factor 4π appears in both equations in order to correct for the isotropy of incident particles.

Similarly, the differential dose equivalent and integral dose equivalent are given by:

$$H(i) = \frac{4\pi \times 1.602 \times 10^{-9}}{\rho} LET(i)N(i)Q(i)\overline{W}(i) \tag{3.42}$$

$$H(LET(i) \geq LET(x)) = \frac{4\pi \times 1.602 \times 10^{-9}}{\rho} \sum_{i=max}^{x} LET(i)N(i)Q(i)\overline{W}(i), \tag{3.43}$$

respectively and have units of Sv. $Q(i)$ is the quality factor dependent on LET interval.

3.6 Thermal/Resonance Neutron Detectors (TRND)

CR-39 PNTDs are only sensitive to neutron energies in the range of 1-20 MeV. For this reason, a neutron moderator with sensitivity to neutrons of energy < 1 MeV is used in conjunction with CR-39 PNTD to detect low energy neutrons. This detector is referred to as a thermal/resonance neutron detector (TRND).

A TRND consists of having two small squares (0.6 x 0.6 x 0.1) of ^{6}LiF sandwiched between layers of CR-39 PNTD. One of the ^{6}LiF squares is completely covered with thermal neutron absorber while the second is uncovered. In this experiment, cadmium (Cd) is used as the thermal neutron absorber.

Since ^{6}LiF has a high cross section (950 b at thermal energy) for low energy neutron absorption and decays via the ^{6}Li(n,T)α reaction, it serves as a radiator of alpha and

T (^{3}H) particles to the CR-39 PNTDs. These tracks from the α and T particles are a measure of incident low energy neutron fluence during the exposure. The Cd foils shield thermal neutrons. This allows the PNTD pair to distinguish between thermal ($<$ 0.025 eV) and resonance neutrons (0.025 eV - 1 MeV). The part of the CR-39 PNTD that is not covered with the ^{6}LiF and/or Cd can be used to measure high energy neutrons (1-20 MeV).

After exposure, the processed PNTDs contain latent tracks produced by the α and T particles. These short-range stopping α particles from the ^{6}LiF squares produce distinctive tracks which can easily be discerned using an optical microscope. Chemical processing of the TRNDs produces tracks which are large enough for easy detection while retaining sufficient track detail needed for background discrimination [Benton et al., 2001]. The track densities are manually counted using a 50 x optical microscope. Backgrounds were counted in the detectors from control TRNDs.

Once the α-particle fluence has been measured, it is converted to neutron dose equivalent (H) using the conversion factors of McDonald, shown in Figure 3.3 [McDonald et al., 1998]. It is important to note that for energies below 20 MeV, the differences between the plotted conversion coefficient data points are small and can be considered negligible when compared to the uncertainties in the estimated risk resulting from exposure to neutrons [McDolland, Thomas, NCRP, US NRC, and ANS]. It can be seen from the figure that the largest differences for energies below 20 MeV range from 10 to 30%.

The data was interpolated to include the energy range from 10^{-8} to 20 MeV with increasing increments in log space. The average fluence to dose equivalent conversion coefficients were calculated for high energy (1-20 MeV), epithermal (10 keV-1 MeV), and thermal ($<$1 keV) neutron energies. These average values were found to be 419, 10, and 12 pSv cm^2/n, respectively.

The CR-39 PNTD contained in the TRNDs was chemically etched and read out in

the same way as the other CR-39 PNTDs used in this work, unless otherwise specified.

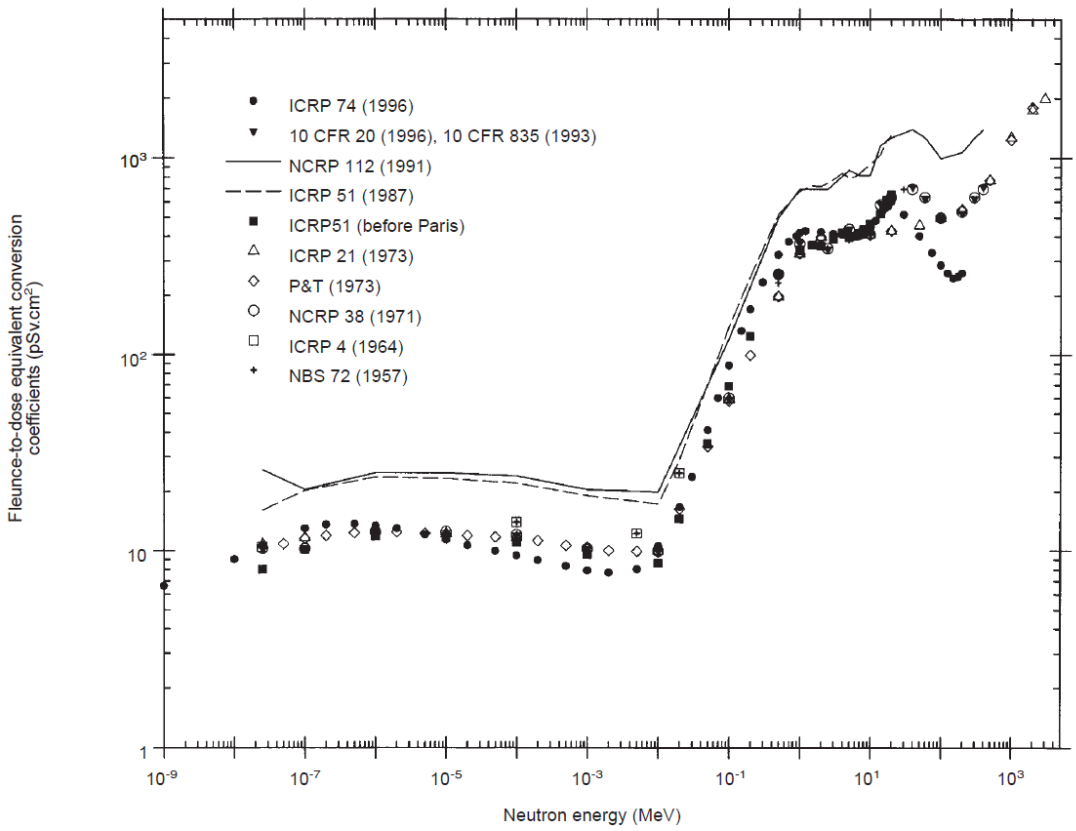

Figure 3.3 Plot of neutron fluence to dose equivalent conversion coefficients. Points are taken from the indicated documents. Continuous curves are data from ICRP Publication 51 and NCRP Report 112 [McDonald et al., 1998].

CHAPTER 4

EXPERIMENTAL DESIGN AND SETUP

This chapter describes the preparation, exposure, and processing of the CR-39 PNTDs used in the photo-neutron experiment.

4.1 Preparation of the CR-39 PNTD and TRND

CR-39 PNTDs and TRNDs used in this experiment were arranged in pairs. Each CR-39 PNTD was cut to dimensions of 4 x 4 cm on a milling machine using a 1/8 inch, 45 degree end mill. Latex gloves were worn while handling the CR-39 to prevent oil and dirt getting on the CR-39 PNTD and TRNDs.

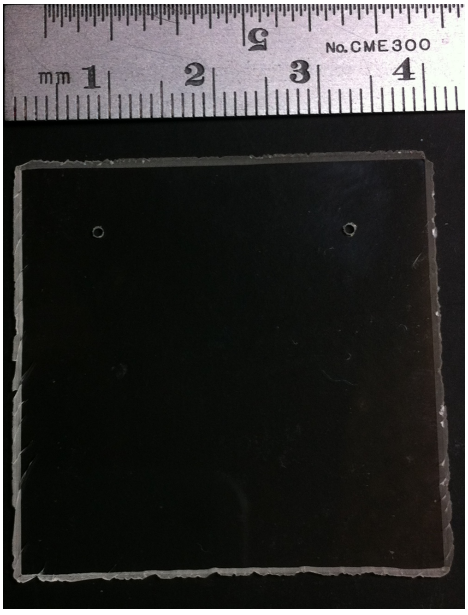

Figure 4.1 CR-39 PNTD measuring 4 x 4 cm with reference scale.

For each CR-39 PNTD and TRND pair, a descriptive identification was inscribed with a diamond-tipped scriber on the lower left of the detector. The identification

label contained the experiment name, the detector number, and a front/back identifier. The first (front) CR-39 PNTD layer, in the pair, was identified by: PHN-01-I, while the second (back) layer was inscribed with PHN-01-II. For the CR-39 TRNDs, the identification labels PHN-TRN-01-I and PHN-TRN-01-II were used.

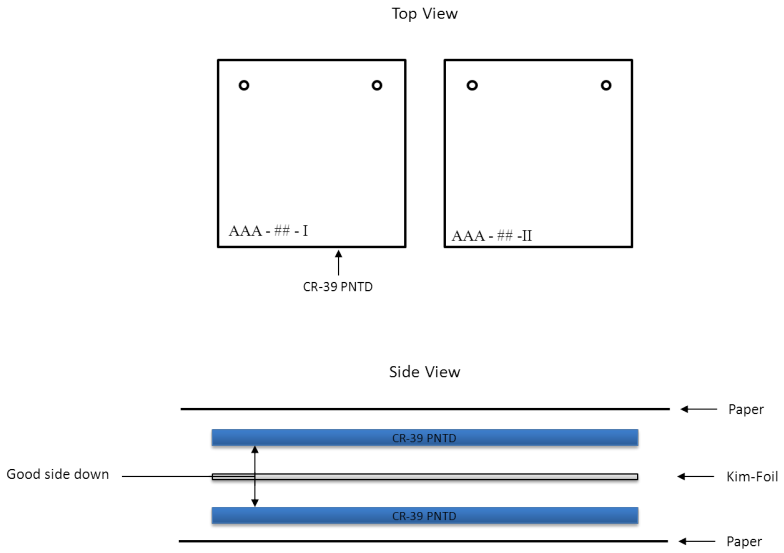

Figure 4.2 Assembly of the CR-39 PNTD pairs. Top: shows the two CR-39 PNTDs with their placement of the mounting holes along with the unique identifier. Bottom: shows the packaging of the CR-39 PNTDs

Each CR-39 PNTD and TRND also had mounting holes drilled into the upper right and left corners of the detectors, about a centimeter from the edges, using a small tabletop drill press. These holes allowed for the CR-39 PNTD and TRND layers to be mounted in a custom made etching rack during chemical processing. Figure 4.1 shows a 4 x 4 cm CR-39 PNTD.

The CR-39 PNTDs were assembled as illustrated in Figure 4.2. An 8 μm layer of Kim-foil (polycarbonate film), was placed between the pair of CR-39 PNTDs. The layer of polycarbonate film allows for oxygen to diffuse into the latent damage trails on the CR-39 PNTD surface during and after irradiation of the detectors. Figure 4.2 also shows the placement of the mounting holes, identification label, as well as the

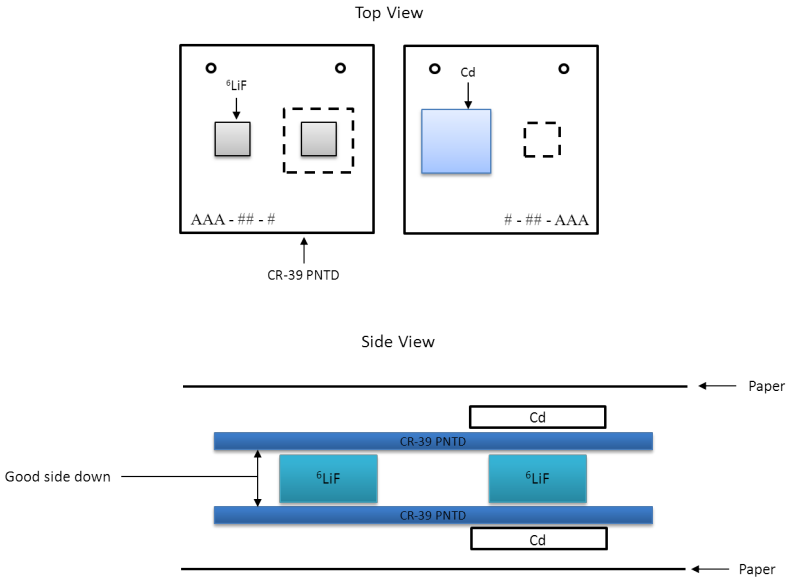

Figure 4.3 Assembly of the CR-39 TRND pairs. The top diagram shows the back and front of the CR-39 TRNDs with their placement of the mounting holes along with the unique identifier. The bottom diagram shows the packaging of the CR-39 TRNDs

final assembly of the CR-39 PNTD pairs. Each CR-39 PNTD pair was wrapped in a piece of paper and bound together with a small piece of adhesive tape. Each CR-39 PNTD pair was then labelled using the same naming convention. Using the example above PHN-01-I and PHN-01-II would be bound together using the identifier PHN-01.

The CR-39 TRNDs were assembled differently than the CR-39 PNTDs. Two 0.6 cm x 0.6 cm x 0.1 cm ^{6}LiF TLD chips were taped to one side of the CR-39 PNTD about 1 cm from the side edges and 2 cm from the top and bottom of the PNTD layer. Once the ^{6}LiF TLD chips are taped to one side of the CR-39 PNTD another was placed on top of the ^{6}LiF TLD chips sandwiching them together. One of the ^{6}LiF TLD chips that was sandwiched between the CR-39 PNTDs was covered by a 1 cm x 1 cm x 0.1 cm layer of metal cadmium (Cd), while the second was uncovered, as shown in figure 4.3. Each CR-39 TRND was wrapped in a piece of paper and bound together with a small piece of adhesive tape. After wrapped in paper, each CR-39

TRND pair was labelled using the same naming convention.

4.2 Irradiations

The irradiations were preformed at Hillcrest Medical Center in Tulsa, OK, using a Varian Clinac 23EX at 6 and 18 MV_p beam, and a Varian Trilogy with a 10 MV_p. The field size of each beam was set to 15 x 15 cm^2. CR-39 PNTDs and TRNDs were irradiated in air and inside a polyethylene phantom. The phantom consisted of high density polyethylene (0.96 gm/cm^3) blocks each with dimensions of 20 x 20 cm^2 and thicknesses of either 5.0 cm or 2.5 cm. These blocks were placed in three columns arranged in a way to create a rectangular box with dimensions 60 cm in length, 20 cm in width and 20 cm in height. The surface of the phantom was placed at the height so that the source to surface distance (SSD) was 100 cm. The beam was centered in the middle of the first column block. Diagrams illustrating the placement of detectors in air and in the phantom are shown in figure 4.4.

The detectors irradiated in air were centered perpendicular to the beam at distances of 0, 20, 40 cm from the primary beam axis. The surface of the detectors was arranged so that the SSD was 100 cm. In the polyethylene phantom the detectors were centered perpendicular to the beam, but at depths of 0, 5, and 10 cm from the surface, in the beam central axis at depths of 10 cm from the surface, and a distances of 20 and 40 cm from the beam central axis.

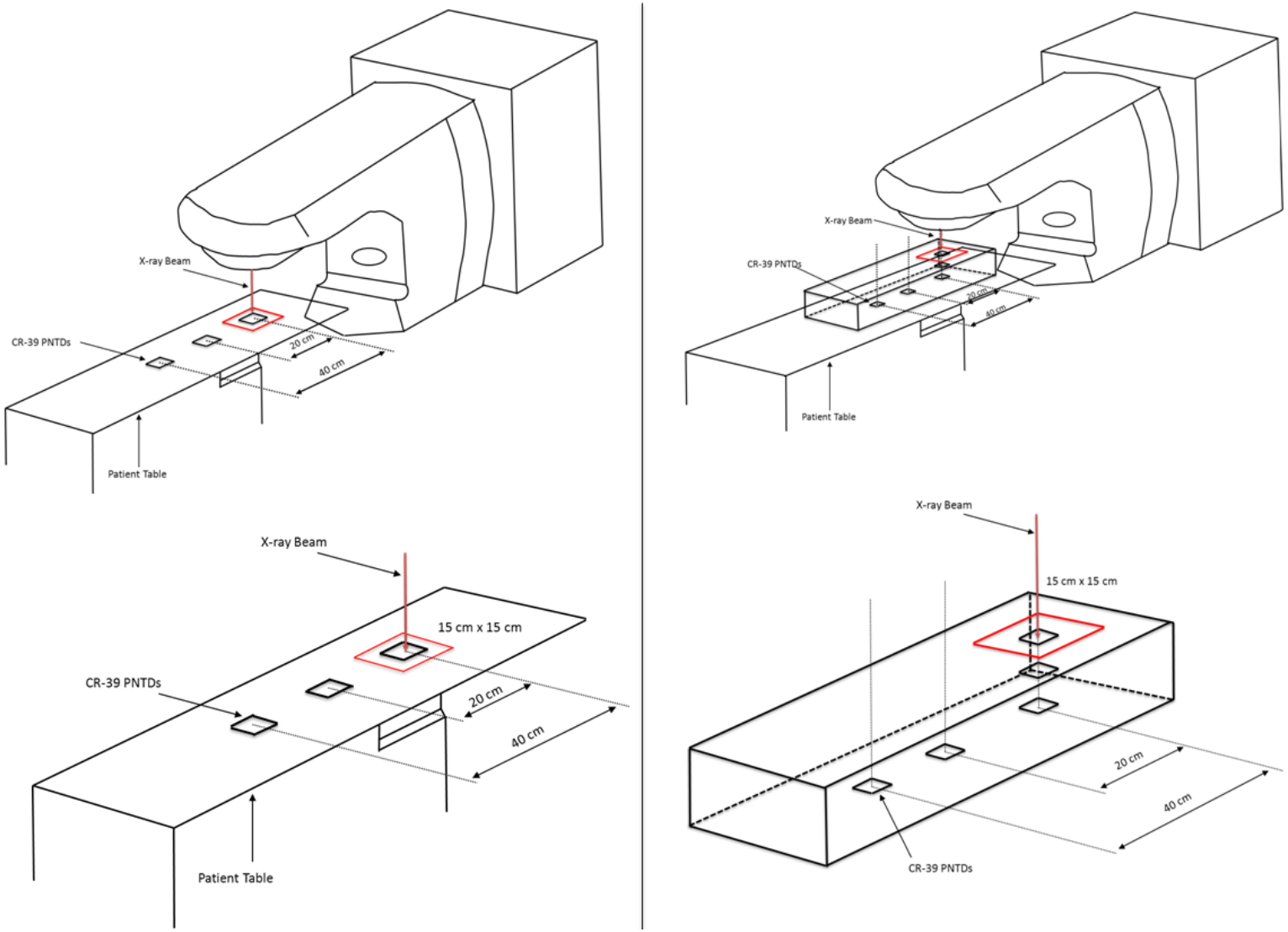

Figure 4.4 The diagram on the left shows the schematics for the experiment in air for both PNTDs and TRNDs. The diagram on the right shows the schematics for the experiment for both PNTDs and TRNDs.

4.3 Processing of the Exposed CR-39 PNTD and TRND Pairs

After the CR-39 PNTDs and TRNDs were exposed to radiation, they were taken back to the lab and disassembled. Latex gloves were worn to prevent dirt and oils getting on the PNTDs and TRNDs. The CR-39 PNTDs and TRNDs were then separated into two groups depending on the identifier as group I and group II. The height, width, thickness, and mass of each CR-39 PNTD and TRND were measured and recorded before they were chemically etched. This information was needed to determine the bulk etch of the detectors after being chemically etched.

After the measurements were made, the CR-39 PNTDs were placed in a custom made mounting rack using stainless steel wire and 0.5 cm spacers, as illustrated in Figure 4.5. Each etching rack was then placed in a plastic container with one liter of 6.25 N NaOH solution. These plastic containers were then placed in a Precision Scientific shaking water bath operating at 50°C. The mounting racks in the plastic container were oriented so that the CR-39 PNTDs and TRNDs were parallel to the direction of movement of the shaking water bath. An illustration of this process is shown in Figure 4.6.

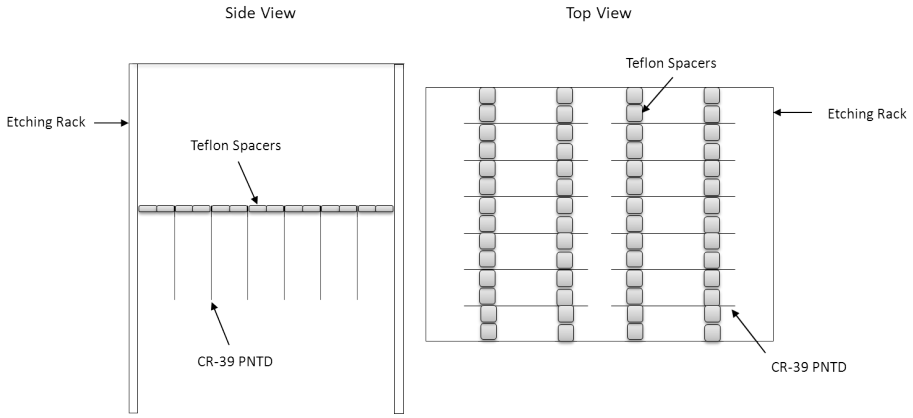

Figure 4.5 Mounting of CR-39 PNTDs and TRNDs on etching rack

The CR-39 PNTDs and TRNDs were etched for 36 hours. After etching the racks

were removed from the plastic container and rinsed with cold tap water. The CR-39 PNTDs were then disassembled from the etching rack and thoroughly rinsed with deionized water. After rinsing, the detectors were hung inside a fume hood to dry at room temperature for 24 hours.

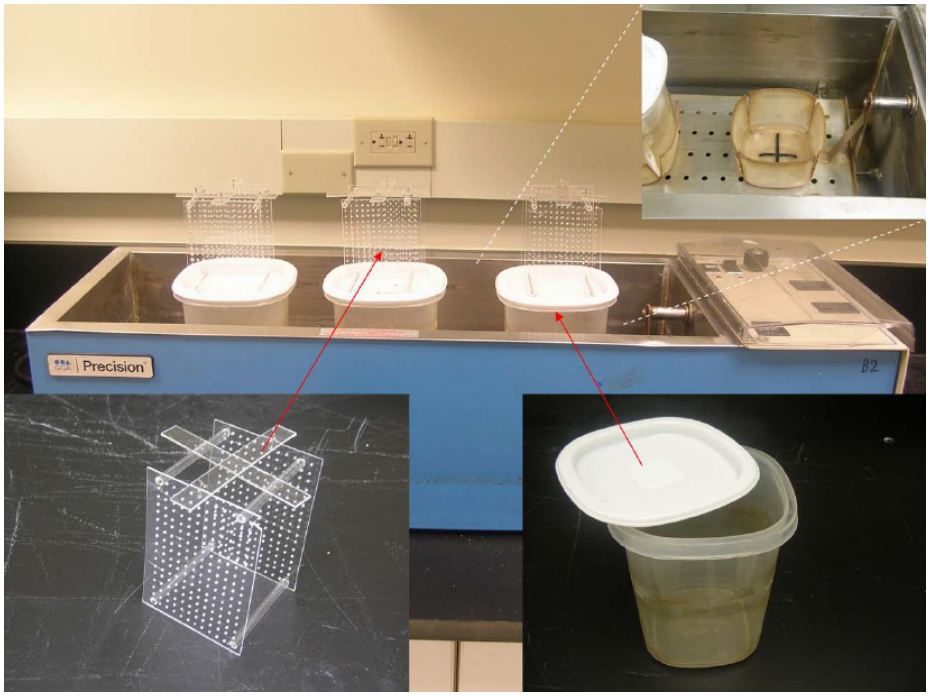

Figure 4.6 Placement of etching racks in water bath

Post etch measurements of the thickness and mass were repeated for each CR-39 PNTD and TRND and the data recorded. The bulk etch, or thickness removed from the detector surface by chemical etching, of the CR-39 PNTD and TRND layers was determined using the bulk etch equation (3.10), as discussed in Section 3.2.2. For the duration of 36 hours equation (3.10) yielded bulk etch values of around 10 μm.

4.4 Analysis of CR-39 PNTDs and TRNDs

Each CR-39 PNTD and TRND was read out using a SAMAICA (Scanning and Measuring with Automatic Image Contour Analysis) nuclear track detector analysis system. This system was manufactured by ELBEK-Bildanalyse GmbH, Siegen

Germany, and was used to measure the semi-major, a, and semi-minor, b, axes of all tracks within a given area on the CR-39 PNTD and TRND surface. Figure 4.7 shows a proton recoil tracks from CR-39 PNTDs (a) and alpha particle track from the TRNDs (b).

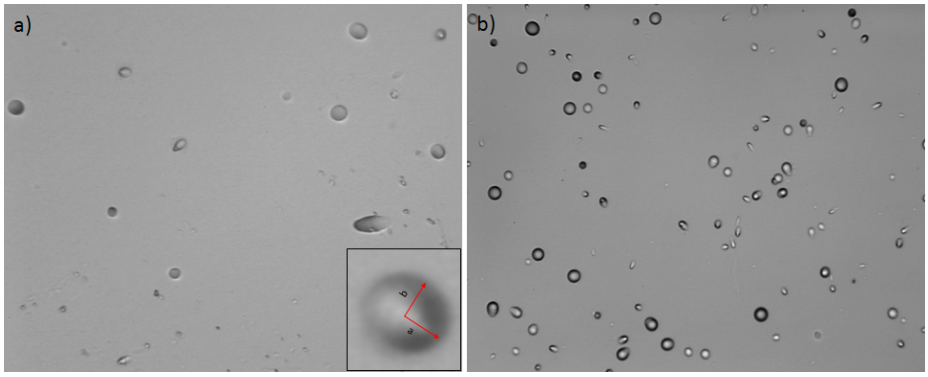

Figure 4.7 The figure on the left (a) shows a photomicrograph of 18 MV beam, nuclear tracks in CR-39 PNTD with 50x magnification. The insert shows the semi-major, a, and semi-minor, b, axes labelled on a nuclear track. The figure on the right (b) shows a photomicrograph of 18 MV beam, alpha tracks in CR-39 TRND with 20x magnification.

The ELBEK system is comprised of a Leitz Orthoplan optical microscope equipped with transmitted light illumination, a CCD camera, and a computer controlled translation stage. The hardware includes a standard personal computer equipped with a video frame grabber card and running customized track analysis software for both the analysis of video images and the measurement of nuclear tracks. The computer also coordinates data acquisition, movement of the microscope stage, and storage of the measured data. Figure 4.8 shows the ELBEK system used for scanning the CR-39 PNTDs and TRNDs.

During analysis of a CR-39 PNTD or TRND layer, the ELBEK computer moves the translation stage to a predetermined set of coordinates and retrieves an image from the CCD camera. The SAMAICA software will then allow the user to manually fit ellipses to the openings of the nuclear tracks in the image. This gives the lengths

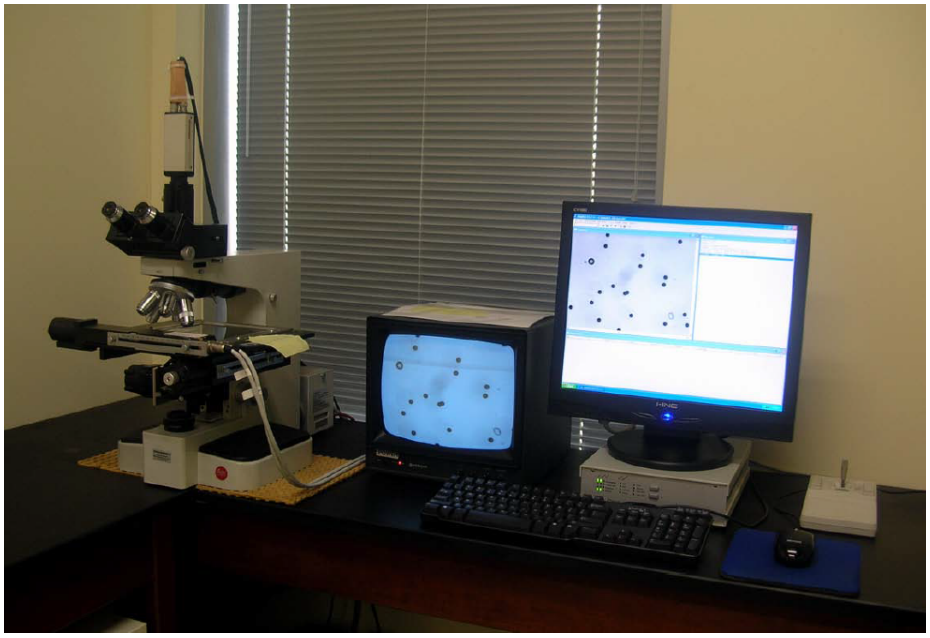

Figure 4.8 The ELBEK automatic track detector analysis system used in analyzing the CR-39 PNTDs for this study.

of the semi-major, a, and semi-minor, b, axes characterizing each track as discussed in Chapter 3. Once an image is analysed and all the tracks within the image are measured, the computer stores the data and moves the microscope stage to the next position and the process is repeated.

Following the analysis of the CR-39 PNTDs and TRNDs, the data file generated is processed by a custom written computer code designed specially for this project to generate differential and integral LET spectra. The process of generating the differential and integral LET spectra is as follows:

1. The reduced etch rate ratio, V_R, is determined for each track based on its measured semi-major, a, and semi-minor, b, axes and normalized by the bulk etch, B, using equation (3.10).

2. The LET_{200}CR-39 in keV/μm of each track is calculated based on the calibration function, that relates V_R to LET_{200}CR-39 [Benton, 2004]:

$$y = 2.127 + 0.9319x + 0.3124x^2 + 1.054x^3 \ . \tag{4.1}$$

3. The LET_{200}CR-39 for each track is converted to $\mathrm{LET}_{\infty}\mathrm{H_2O}$ [Benton, 2004]:

$$log(LET_{\infty}H_2O) = 0.1689 + 0.984\, log(LET_{200}CR{-}39) \tag{4.2}$$

4. The dip angle cutoff, δ_c for each track is calculated based on an empirical fit of δ_c and V_R. This empirical fit was determined by E R Benton [Benton, 2004] and given as:

$$\delta_c = 0.0305 + 0.9872 \sin^{-1}\left(\frac{1}{V_R}\right). \tag{4.3}$$

5. The track values are then sorted into a fixed number of equal bins of 1 keV/μm width.

The use of binning the LET in fixed number of bins of 1 keV/μm allows for easy background subtraction as measured in control CR-39 PNTDs and TRNDs detectors. In this case the control CR-39 PNTDs and TRNDs detectors were made at the same time as the other detectors. However, they were not exposed to any radiation from the linacs.

CHAPTER 5

RESULTS

5.1 Integral Fluence

The LET spectra for PNTDs irradiated in the 18, 10, and 6 MV_p x-ray beams were generated following the readout of the detectors. The integral and differential LET fluence have been normalized by the absorbed dose of x-rays delivered. For all three beams, 6, 10, and 18 MV_p, a dose of 200 monitor units (MU) was delivered. It was assumed, in this study, that 1 MU is equal to 1 cGy. The individual integral and differential LET fluence spectra can be seen in appendix A and appendix B respectively.

Figure 5.1 shows the integral fluence LET spectrum from secondary neutrons measured in CR-39 PNTD from a 200 cGy 18 MV_p x-ray exposure in air at varying distances off-axis from the beam. The highest fluence of photo-neutrons was measured to be $\sim$900 tracks/cm^{2}Gy$_x$ at 0 cm off-axis to the beam. The fluence decreased to $\sim$400 and $\sim$100 tracks/cm^{2}Gy$_x$ as the distance off-axis increased from 20 to 40 cm, respectively. One reason for the decrease in fluence as the distance increased could be due to the angular photo-neutron cross section. When a high energy photon interacts with a high Z nucleus, a photo-neutron can be produced. The direction of these photo-neutrons is dependent upon the energy of the x-ray [Sanchez-Doblado et al., 2012]. Higher energy neutrons will have a smaller scattering angle so that more neutrons will pass through and interact with a detector directly in the beam as compared to detectors at 20 and 40 cm off-axis to the beam.

Figure 5.1 shows a greater abundance of lower LET tracks ($< \sim$100 keV/μm) to

that of higher LET tracks (> ∼100 keV/μm) for all three detectors placed at 0, 20, and 40 cm off-axis. This is due to the fact that neutron collisions taking place in the detectors are predominantly with protons. As discussed previously in Chapter 2, any tracks greater than ∼100 keV/μm come from target fragmentation of the heavier nuclei in the detector. The LET spectra in detectors at 0 and 20 cm off-axis had low contributions from high LET tracks, while the LET spectra measured at 40 cm off-axis had no contribution from high LET tracks.

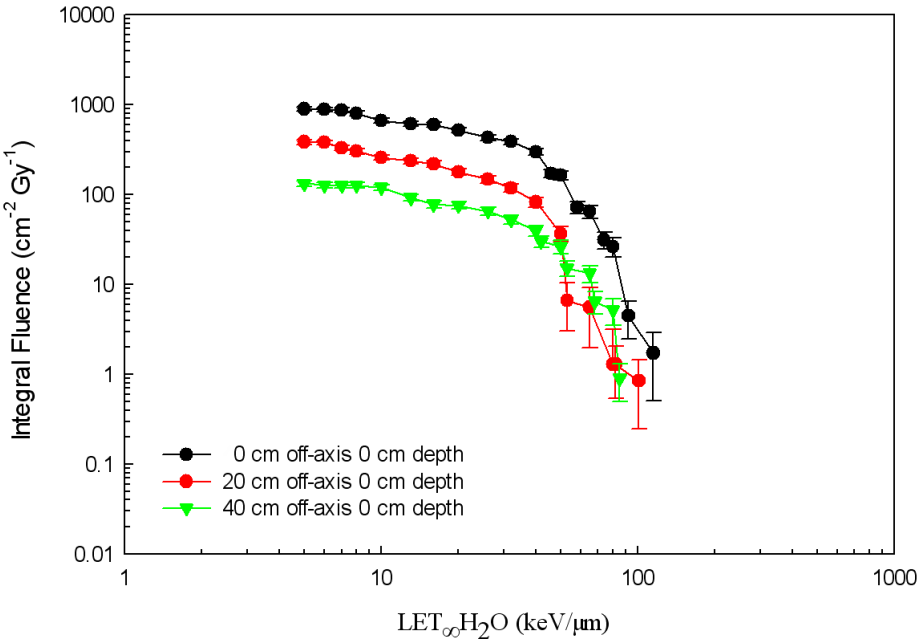

Figure 5.1 Integral LET Fluence spectra from neutrons measured in the 18 MV$_p$ x-ray beam in air at 0 cm depth and at varying distances off-axis to the beam.

Figure 5.2 shows the integral LET fluence for the 18 MV$_p$ x-ray beam in a phantom at 0 cm off-axis to the beam and at varying depths of 0, 5, and 10 cm. The fluence at the surface (0 cm depth) was ∼1000 tracks/cm^{2}Gy$_x$. This value is comparable to the measurements made in air at the same position (0 cm off-axis, 0 cm depth) shown in Figure 5.1. At depths of 5 and 10 cm the fluence decreased to ∼200 and ∼70 tracks/cm^{2}Gy$_x$, respectively. This is likely due to the attenuation of the neutrons

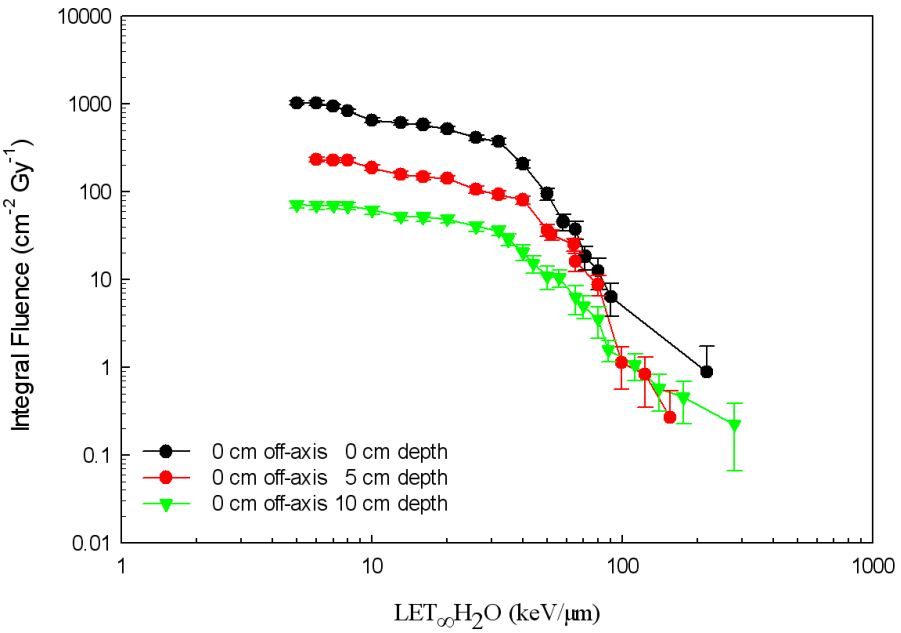

Figure 5.2 Integral Fluence spectra from neutrons measured in the 18 MV_p x-ray beam in a phantom at 0 cm off-axis and at varying depths.

with depth inside the phantom.

It can also be seen in Figure 5.2 that neutrons at all three depths of the phantom make a greater contribution of high LET tracks compared to neutrons in air (Figure 5.1). This increase in high LET tracks is due to the polyethylene phantom. There are two reasons for why high LET tracks are more likely to occur in the presence of the phantom than in air. The first is target fragmentation from the carbon atoms in the polyethylene phantom. As described in Chapter 2, target fragmentation occurs when an energetic nucleon, in this case a neutron, penetrates a heavy target nucleus, e.g. carbon, which then ejects one or more nucleons or heavier fragments. The residual nucleus is left in an unstable state and will de-excite through the evaporation of more nucleons. The residual nucleus will then recoil in the opposite direction to that of the evaporated nucleons. If the recoil nucleus were to enter the CR-39 PNTD it would produce a high LET track.

Another reason for the greater contribution of high LET tracks in the phantom

than in air could be due to the neutron absorption cross section from oxygen and carbon nuclei in CR-39 PNTD. High energy neutrons can interact elastically with carbon or a hydrogen nuclei in the polyethylene. These elastic interactions will cause a fraction of the neutrons' kinetic energy to be transferred to the hydrogen and carbon nuclei, thereby moderating neutrons. The absorption cross section for oxygen and carbon in the CR-39 PNTD increases as the neutron energy decreases. The absorption of a neutron from a carbon or oxygen atom will cause the nucleus to be in an excited state, which will then de-excite through an evaporation process causing the residual nucleus to recoil and produce a high LET track.

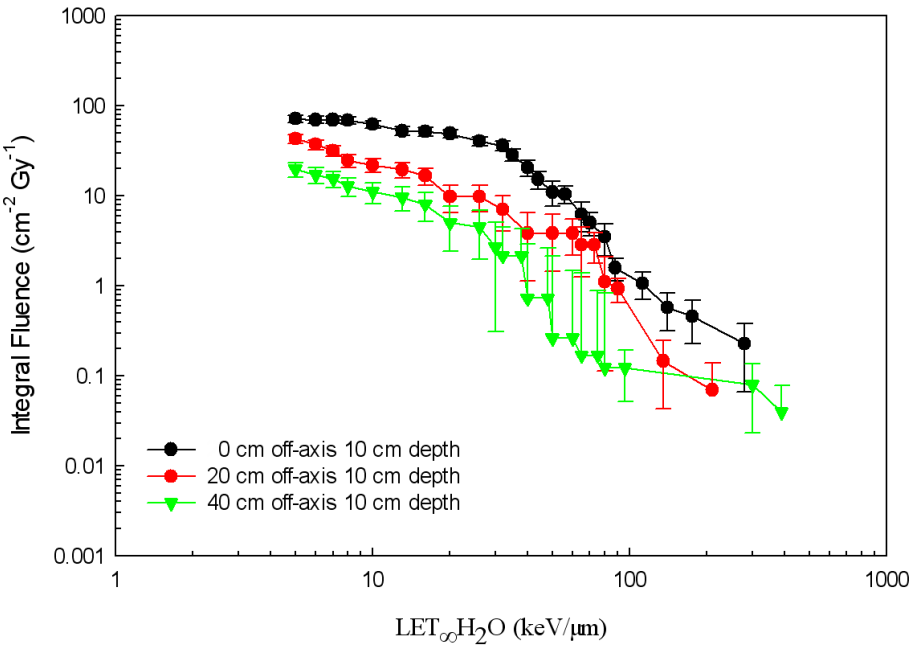

Figure 5.3 Integral Fluence vs LET for 18 MV$_p$ x-ray beam in phantom at 10 cm depths with varying distances off-axis.

Figure 5.3 shows the Integral LET fluence spectra measured in detectors exposed in an 18 MV$_p$ x-ray beam in a phantom at a depth of 10 cm and at varying distances off-axis. The highest measured fluence was ~70 tracks/cm^{2}Gy$_x$ at 0 cm off-axis and this decreased to ~40 and ~20 tracks/cm^{2}Gy$_x$ at distances of 10 and 20 cm off-axis, respectively. The contributions from high LET tracks can also be seen in Figure 5.3

and are due to the detectors being irradiated inside the phantom.

A comparison integral LET fluence spectra measured in those detectors that were exposed in the phantom to those exposed in air is shown in Figure 5.4. Figure 5.4(a) shows a comparison of spectra measured in the 18 MV_p x-ray beam at 0 cm off-axis, and 0 cm depth in phantom versus spectra measured in the 18 MV_p x-ray beam at 0 cm off-axis in air. There is not a significant difference between the two integral LET fluence spectra, since both detectors were located at 100 cm SSD and exposed under the same conditions. The only difference is the contribution of high LET tracks in the phantom that is not seen in air.

Figure 5.4(b) compares LET spectrum measured at 0 cm off-axis and 10 cm depth in the phantom with that measured at of 0 cm off-axis in air. The spectrum measured in air has a significantly larger fluence, $\sim$900 tracks/cm^{2}Gy$_x$, than that measured in the phantom, $\sim$70 tracks/cm^{2}Gy$_x$. The lower fluence is due to the greater attenuation of neutrons in the polyethylene phantom as compared to air. The spectrum measured in the phantom also possesses a greater contribution from high LET tracks. Figures 5.4 (c) and (d) also show the attenuation in neutron fluence, as well as a greater contribution of high LET tracks, in the PNTDs at 10 cm in the phantom compared to that in air.

5.2 Results from Plastic Nuclear Track Detectors

Table 5.1 lists the measured values from PNTDs in air for absorbed dose and dose equivalent normalized to the given x-ray dose of 200 cGy for maximum x-ray energies of 18, 10, and 6 MV_p. Only the PNTD directly in the 6 MV_p x-ray beam was measured due to photo-neutron production occurring with x-ray energies greater that $\sim$7 MeV. The PNTD directly in the 6 MV_p x-ray beam was measured to verify that photo-neutron absorbed dose would be negligible compared to background.

As shown in Table 5.1, the measured values, of normalized absorbed dose, for the

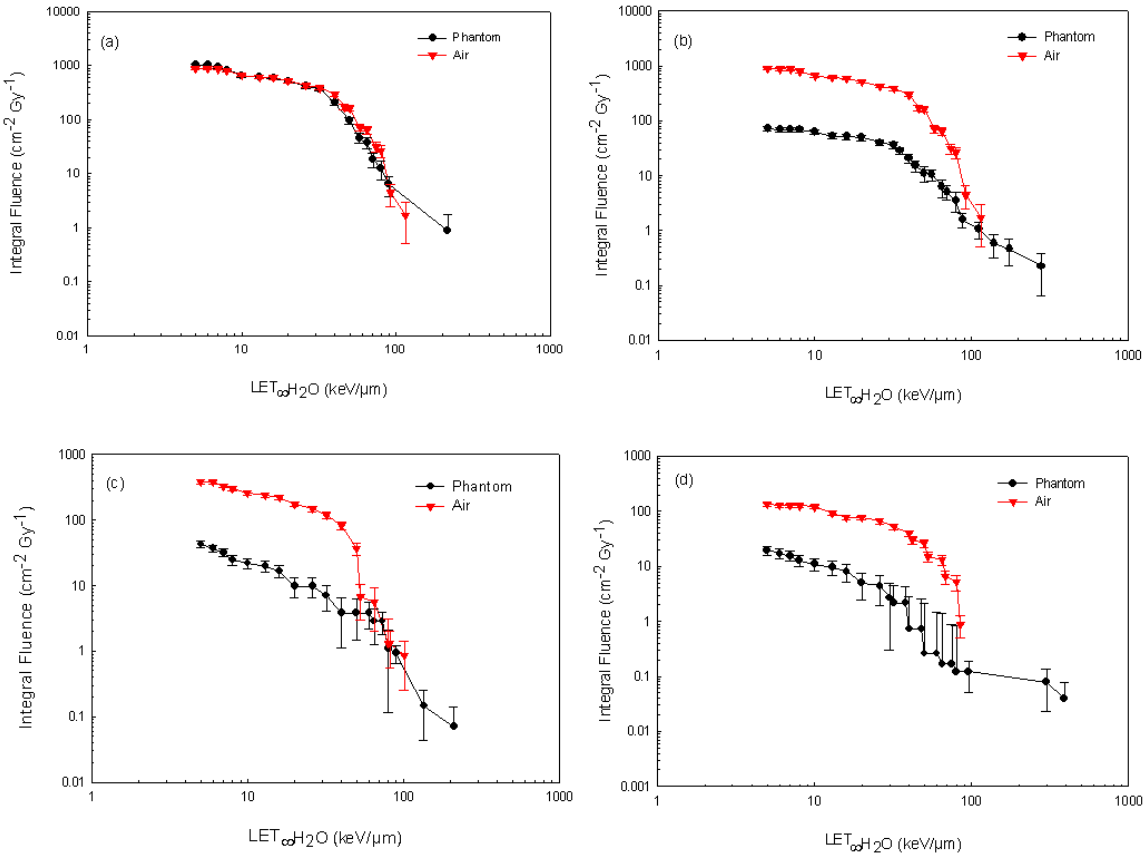

Figure 5.4 LET spectra measured by CR-39 PNTDs from an 18 MV_p x-ray beam in phantom vs air: (a) 0 cm depth, 0 cm off-axis in phantom vs 0 cm off-axis in Air (b) 0 cm off-axis, 10 cm depth in phantom vs 0 cm off-axis in air, (c) 20 cm off-axis, 10 cm depth in phantom vs 20 cm off-axis in air, (d) 40 cm off-axis, 10 cm depth in phantom vs 40 cm off-axis in air.

18 MV_p x-ray beam are 495 ± 29 $\mu Gy_n/Gy_x$ for the detector directly in the beam (0 cm off-axis), 166 ± 12 $\mu Gy_n/Gy_x$ for the detector 20 cm off-axis to the beam, and 74 ± 6 $\mu Gy_n/Gy_x$ for the detector 40 cm off-axis. The normalized dose equivalent measured from the same detectors was 5500 ± 420, 1398 ± 155, 845 ± 103 $\mu Sv_n/Gy_x$, respectively.

The majority of the dose deposited into the detectors are from neutrons created directly in the beam. As mentioned previously, high energy neutrons created from a high energy x-ray beam are highly directional [Sanchez-Doblado et al., 2012]. For this reason there are more photo-neutrons along the beam axis than there are at a distance 20 or 40 cm off-axis. The more photo-neutrons there are, within a given spatial volume, the more interactions will occur with the material and the greater the deposit of absorbed dose.

This trend is also seen in the detectors exposed to the 10 MV_p x-ray beam. The highest measured value of normalized absorbed dose was 10 ± 3 $\mu Gy_n/Gy_x$ from the detector at 0 cm off-axis, 5 ± 2 $\mu Gy_n/Gy_x$ for the detector at 20 cm off-axis, and 3 ± 2 $\mu Gy_n/Gy_x$ from the detector at 40 cm off-axis. The measured values for dose equivalent were 103 ± 46, 30 ± 38, and 30 ± 37 $\mu Sv_n/Gy_x$, respectively. The detector irradiated directly in the 6 MV_p x-ray beam had measured values of 1 ± 2 $\mu Gy_n/Gy_x$, and 3 ± 36 $\mu Sv_n/Gy_x$.

As mentioned in Chapter 2, the average x-ray energy produced from a medical linear accelerator is about one third the maximum energy [Khan, 2003]. Since the threshold x-ray energy to produce a photo-neutron is ∼7 MeV, the higher the maximum energy of the x-rays produced by the linear accelerator, the more probable it is for a photon to have energies above 7 MeV. The increase in the number of photo-neutrons will lead to more neutron absorbed dose deposited in the detectors. This can be seen in Table 5.1 comparing the detectors exposed at 0 cm off-axis for the 18, 10 and 6 MV_p x-ray beams. The absorbed dose and the dose equivalent measured in these

Table 5.1 Neutron absorbed dose and dose equivalent measured in CR-39 PNTD and exposed to x-ray beams of different energy (6, 10, and 18 MV_p) at three off-axis distances in air.

Maximum X-Ray Energy (MV_p)	**Distance off-Axis (cm)**	**Normalized Absorbed Dose ($\mu Gy_n/Gy_x$)**	**Normalized Dose Equivalent ($\mu Sv_n/Gy_x$)**
18	0	495±29	5500±420
	20	166±12	1398±155
	40	74±6	845±103
10	0	10±3	103±46
	20	5±2	30±38
	40	3±2	30±37
6	0	1±2	3±36

detectors were 495 ± 29, 10 ± 3, and 1 ± 2 $\mu Gy_n/Gy_x$ and 5500 ± 420, 1398 ± 155, 845 ± 103 $\mu Sv_n/Gy_x$ respectively. The 6 MV_p x-ray beam measurement verified that photo-neutrons are not produced by x-rays of energy less than ∼7 MeV.

Table 5.2 lists the values measured in a phantom of normalized absorbed dose and dose equivalent for x-ray energies of 18, and 10 MV_p. Detectors were exposed at depths of 0, 5, and 10 cm from the upper surface of the phantom along the beam axis, and also at a distances of 20 and 40 cm from the beam's central axis at a depth of 10 cm from the surface. The PNTDs in the 6 MV_p x-ray beam were not measured due to photo-neutron production not occurring at energies less than ∼7 MeV.

For the PNTDs exposed in the 18 MV_p x-ray beam, the values measured were 467 ± 28 $\mu Gy_n/Gy_x$ and 4307 ± 370 $\mu Sv_n/Gy_x$ in the detector directly in the beam (0 cm off-axis at 0 cm depth), 131 ± 10 $\mu Gy_n/Gy_x$ and 1491 ± 146 $\mu Sv_n/Gy_x$ in the detector at 0 cm off axis at 5 cm depth, and 46 ± 5 $\mu Gy_n/Gy_x$ and 550 ± 85 $\mu Sv_n/Gy_x$ for the detector 0 cm off-axis and 10 cm depth.

Hydrogen is the best moderator of neutrons because the masses of the proton and

Table 5.2 Neutron absorbed dose and dose equivalent measured in CR-39 PNTD exposed to x-ray beams of different energy (10, and 18 MV_p) at varying depths and distances off-axis in the phantom.

Maximum X-Ray Energy (MV_p)	**Distance off-Axis (cm)**	**Depth (cm)**	**Normalized Absorbed Dose ($\mu Gy_n/Gy_x$)**	**Normalized Dose Equivalent ($\mu Sv_n/Gy_x$)**
18	0	0	467±28	4307±370
	0	5	131±10	1491±146
	0	10	46±5	550±85
	20	10	16±3	167±57
	40	10	6±3	46±43
10	0	0	9±3	61±43
	0	5	3±2	11±36
	0	10	0.2±2	2±37
	20	10	1±2	10±37
	40	10	1±2	13±37

neutron are very similar to each other. Polyethylene, which has 2 hydrogen atoms for every carbon atom, will moderate and/or scatter neutrons as they collide elastically with protons. Due to the neutrons losing their energy and or scattering, they will attenuate, resulting in a lower dose as the depth increases. The absorbed dose and dose equivalent also decreased as the distance off-axis increased. The detectors exposed at 20 and 40 cm off-axis at 10 cm depth have measured values for absorbed dose and dose equivalent of 16 ± 3 $\mu Gy_n/Gy_x$ and 167 ± 57 $\mu Sv_n/Gy_x$ for detectors exposed at 20 cm off-axis, and 6 ± 3 $\mu Gy_n/Gy_x$ and 46 ± 43 $\mu Sv_n/Gy_x$ for detectors exposed at 40 cm off-axis.

It is interesting to note that the two detectors that were directly in the beam in exposures in air (Figure 5.1) and in the phantom (Figure 5.2) measured the same values for absorbed dose within error bars: 495 ± 29 $\mu Gy_n/Gy_x$ in air and

467 ± 28 $\mu Gy_n/Gy_x$ in the phantom. Both these detectors were located at 100 cm SSD and exposed under the same conditions. The only difference is the PNTD in air was placed on top of the treatment table, while the PNTD in the phantom was placed on top of the polyethylene phantom.

Results from PNTDs exposed to the 10 MV_p x-ray beam also show the same trend as the PNTDs exposed to the 18 MV_p x-ray beam. The highest dose was measured in the PNTD directly in the beam with values of 9 ± 3 $\mu Gy_n/Gy_x$ and 61 ± 43 $\mu Sv_n/Gy_x$. These values decreased to 3 ± 2 and 0.2 ± 2 $\mu Gy_n/Gy_x$ for absorbed dose and 11 ± 36 and 2 ± 37 $\mu Sv_n/Gy_x$ for dose equivalent at 0 cm off-axis and at 5 and 10 cm depths, respectively. For the PNTDs at 20 and 40 cm off-axis and at 10 cm depth, the absorbed dose for both detectors was 1 ± 2 $\mu Gy_n/Gy_x$. The dose equivalent values were 10 ± 37 and 13 ± 37 $\mu Sv_n/Gy_x$, respectively.

The absorbed dose measured in the detectors exposed directly in the 10 MV_p x-ray beam in air and in the phantom shows the same trend as that seen in the detectors exposed in the same position in the 18 MV_p x-ray beam. These values from the 10 MV_p x-ray beam are 9 ± 3 $\mu Gy_n/Gy_x$ in the phantom and 10 ± 3 $\mu Gy_n/Gy_x$ in air. Again, this is because both detectors were exposed at the same distance from the source (100 cm SSD) and under the same conditions.

Table 5.3 shows the contribution from high LET ($\geq$ 100 keV/μm) particle dose equivalent to neutron absorbed dose and dose equivalent measured in CR-39 PNTD exposed in air, as a percentage of the total normalized neutron absorbed dose and dose equivalent. In measurements made in the 18 MV_p x-ray beam, the highest contribution of high LET tracks that contributed to neutron absorbed dose is 2 ± 14% at 0 cm off-axis. At distances 20 and 40 cm off-axis, the contribution of high LET tracks to the neutron absorbed dose is 1 ± 10% and 0%, respectively. For the measurements made in the 10 MV_p x-ray beam, only the detector directly in the beam registered any contribution to neutron dose from high LET tracks: 1 ± 5%. As explained in

Table 5.3 Contribution from High LET (≥100 keV) tracks to absorbed dose and dose equivalent from neutrons measured in CR-39 PNTD exposed to x-ray beams of different energy at three off-axis distances in air.

Maximum X-Ray Energy (MV_p)	**Distance off-Axis (cm)**	**Percentage of High LET Tracks Normalized Dose**	**Percentage of High LET Tracks Normalized Dose Equivalent**
18	0	2±14	5±27
	20	1±10	4±23
	40	0	0
10	0	1±5	8±20
	20	0	0
	40	0	0
6	0	0	0

Chapter 2, target fragmentation is the production of short-range (<10 μm) secondary particles having LET above that of the primary particle [Benton et al., 2011].

Table 5.4 shows the contribution from high LET tracks to neutron absorbed dose and dose equivalent measured in CR-39 PNTD exposed in the phantom to 18 and 10 MV_p x-ray beams. For the detectors exposed to the 18 MV_p x-ray beam, the highest percent contribution from high LET tracks to neutron absorbed dose was measured at positions of 20 and 40 cm off-axis at a depth of 10 cm: 12 ± 18% and 10 ± 15%, respectively. For the detectors exposed at 0 cm off-axis and at depths 0, 5, and 10 cm, the percent contributions from high LET tracks to neutron absorbed dose were: 3 ± 21%, 2 ± 15%, and 9 ± 29%, respectively. The percent contribution from high LET tracks to neutron absorbed dose increased with increasing depth. By comparing the percent contribution of high LET tracks to neutron absorbed dose measured in an 18 MV_p x-ray beam in the phantom (Table 5.4) to that measured in air (Table 5.3), one can infer that high LET tracks due to target fragmentation have

Table 5.4 Contribution from High LET tracks to neutron absorbed dose and dose equivalent measured in CR-39 PNTDs exposed to x-ray beams of 18 and 10 MV_p at varying depths and distances off-axis in the phantom.

Maximum X-Ray Energy (MV_p)	**Distance off-Axis (cm)**	**Depth (cm)**	**Percentage of High LET Tracks Normalized Dose**	**Percentage of High LET Tracks Normalized Dose Equivalent**
18	0	0	3±21	8±38
	0	5	2±15	5±26
	0	10	9±29	15±34
	20	10	12±18	30±26
	40	10	10±15	25±16
10	0	0	0	0
	0	5	0	0
	0	10	0	0
	20	10	0	0
	40	10	0	0

a greater probability of occurring in the presence of the phantom than in air. No high LET tracks were observed in the detectors exposed in the 10 MV_p x-ray beam.

5.3 Results from Thermal Nuclear Track Detectors

Tables 5.5, 5.6, and 5.7 list the measured fluence and dose equivalent values from TRNDs in air for x-ray beam energies of 18, 10, and 6 MV_p. Fluence and dose equivalent have been normalized by the absorbed dose of x-rays delivered. These measurements include the contribution from thermal neutrons ($\leq$ 0.025 eV), and epithermal neutrons ($\sim$0.025 to $\sim$1000 ev). High energy (1-20 MeV) neutron fluence and dose equivalent, measured from them PNTDs in Section 5.2, are also included along with the total dose equivalent from all neutron energies.

The fluence measured for epithermal and thermal neutrons from the TRNDs have been converted to dose equivalent, using the conversion factors of McDonald [McDonald et al., 1998; NCRP, 2005] as discussed in Chapter 2. For epithermal and thermal neutrons, an average conversion factor of 10 and 12 pSv cm^2/n, respectively were used. High energy neutrons have a conversion factor of 419 pSv cm^2/n. Due to this big difference in conversion factors from high energy neutron to that of epithermal and thermal neutrons, the dose equivalent from thermal and epithermal neutrons will be low compared to that from high energy neutrons. In this experiment, epithermal and thermal neutron made up less than 1 % of the total dose equivalent.

Table 5.5 shows the calculated values for dose equivalent from TRNDs exposed to an 18 MV_p x-ray beam at 0, 20, and 40 cm off-axis to the beam. The contribution of epithermal and thermal neutrons from the TRNDs exposed at 0, 20, and 40 cm off-axis are: 0.2 $\pm$ 0.1, 0.1 $\pm$ 0.1, and 0.1 $\pm$ 0.1 $\mu Sv_n/Gy_x$, respectively. The highest value measured is from the detector exposed directly in the beam. This is due to the direction of the photo-neutrons being dependent upon the energy of the incident x-ray beam. High energy x-rays will produce photo-neutrons with low emission angles. The

Table 5.5 Neutron fluence and dose equivalent measured in CR-39 TRNDs exposed to 18 MV_p x-ray beams at three off-axis distances in air.

Distance off-Axis (cm)	**Classification of Neutron Type**	**Normalized Fluence (10^3 cm^{-2} Gy^{-1})**	**Normalized Dose Equivalent ($\mu Sv_n/Gy_x$)**
0	Thermal	7.6±0.4	0.2±0.1
0	Epithermal	1.5±0.1	0
0	High Energy	895.8±49.1	5500±420
	Total	**904.1±49.5**	**5500±420**
20	Thermal	1.6±0.1	0.1±0.1
20	Epithermal	1.4±0.7	0
20	High Energy	383.8±23.6	1398±155
	Total	**386.8±24.4**	**1398±155**
40	Thermal	3.5±0.2	0.1±0.1
40	Epithermal	0	0
40	High Energy	132.8±9.5	845±103
	Total	**136.3±9.7**	**845±103**

energies of the photo-neutrons vary greatly and are dependent upon the photo-neutron cross section as well as the incident x-ray energy. Since photo-neutrons are highly directional the probability of thermal neutrons passing through and interacting with the detector directly in the beam is greater than those interacting with detectors at 20 and 40 cm away off-axis to the beam.

Table 5.6 Neutron fluence and dose equivalent measured in CR-39 TRNDs exposed 10 MV_p to x-ray beam at three off-axis distances in air.

Distance off-Axis (cm)	**Classification of Neutron Type**	**Normalized Fluence (10^3 cm^{-2} Gy^{-1})**	**Normalized Dose Equivalent ($\mu Sv_n/Gy_x$)**
0	Thermal	1.2±0.2	0
0	Epithermal	0.4±0.1	0
0	High Energy	24.4±3.8	103.0±46.0
	Total	**26.0±4.0**	**103.0±46.0**
20	Thermal	0.8±0.1	0
20	Epithermal	0.5±0.1	0
20	High Energy	12.3±3.0	30±38
	Total	**13.7±3.2**	**30±38**
40	Thermal	0.2±0.1	0
40	Epithermal	0.4±0.1	0
40	High Energy	4.8±2.5	30±37
	Total	**5.46±2.6**	**30±37**

Thermal and epithermal neutrons are created when high energy neutrons are moderated due to elastic and inelastic collisions in the head of the linac, room walls, table and other areas and objects in the treatment room. Since the TRNDs in air do not have a high density medium in close proximity to moderate the neutrons, dose equivalent from epithermal and thermal neutrons should be significantly lower than

that from higher energy neutrons.

Results from the 10 MV_p x-ray beam exposure show no contribution from epithermal and thermal neutrons to the neutron dose equivalent. The reason for this is that fewer photo-neutron are being created with the 10 MV_p x-ray beam than in the 18 MV_p x-ray beam.

Table 5.7 Neutron fluence and dose equivalent measured in CR-39 TRNDs exposed to a 6 MV_p x-ray beam at three off-axis distances in air.

Distance off-Axis (cm)	**Classification of Neutron Type**	**Normalized Fluence (10^3 cm^{-2} Gy^{-1})**	**Normalized Dose Equivalent ($\mu Sv_n/Gy_x$)**
0	Thermal	0.7±0.1	0
0	Epithermal	0.8±0.1	0
0	High Energy	2.6±2.5	0
	Total	**4.0±2.7**	**0**
20	Thermal	0.2±0.1	0
20	Epithermal	0.4±0.1	0
	Total	**0.6±0.1**	**0**
40	Thermal	0	0
40	Epithermal	1.0±0.1	0
	Total	**1.0±0.1**	**0**

For the 6 MV_p x-ray beam, dose equivalent was calculated to be zero when taking in account the background. This again verifies that photo-neutrons production does not occur for x-ray energies less than 7 MeV.

Table 5.8 shows the values for dose equivalent from thermal and epithermal neutrons, measured in the TRNDs exposed to an 18 MV_p x-ray beam. The total contribution from thermal and epithermal neutrons measured at 0 cm off-axis with depths of 0, 5, and 10 cm are 3.0 ± 0.4, 9.2 ± 1.0, and 1.9 ± 0.5 $\mu Sv_n/Gy_x$, respectively.

Table 5.8 Neutron fluence and dose equivalent measured in CR-39 TRND exposed to an 18 MV_p x-ray beam at varying depths and distances off-axis in the phantom.

Distance off-Axis (cm)	**Depth cm**	**Classification of Neutron Type**	**Normalized Fluence (10^3 cm^{-2} Gy^{-1})**	**Normalized Dose Equivalent ($\mu Sv_n/Gy_x$)**
0	0	Thermal	85.1±2.6	2.5±0.3
0	0	Epithermal	19.1±0.6	0.5±0.1
0	0	High Energy	1028.5±57.4	4307±370
		Total	**1132.7±60.5**	**4310±370**
0	5	Thermal	264.7±79.4	7.6±0.8
0	5	Epithermal	66.3±19.9	1.6±0.2
0	5	High Energy	234.1±15.2	1491±146
		Total	**565.1±114.5**	**1500±147**
0	10	Thermal	56.1±1.7	1.6±0.2
0	10	Epithermal	13.7±0.4	0.3±0.3
0	10	High Energy	71.7±6.7	550±85
		Total	**125.9±8.8**	**552±85**
20	10	Thermal	39.6±1.2	1.1±0.1
20	10	Epithermal	39.7±1.2	1.0±0.1
20	10	High Energy	42.7±4.9	167±57
		Total	**122.0±7.3**	**169.1±57.2**
40	10	Thermal	44.7±1.3	1.3±0.1
40	10	Epithermal	6.0±0.2	0.1±0.1
40	10	High Energy	19.7±3.5	46±43
		Total	**70.4±5.0**	**47.4±43.1**

The detector exposed at 0 cm off-axis and at a depth of 5 cm had the highest measured value of dose equivalent from low energy neutrons. A reason for this is most likely due to the polyethylene phantom. The high energy neutrons were moderated through the polyethylene phantom which led to a larger fraction of high energy neutrons being moderated down to thermal and epithermal energies.

For the TRNDs exposed outside the beam at 20 and 40 cm off-axis at a depth of 10 cm, the thermal and epithermal contributions to the neutron dose equivalent were 2.1 ± 0.2 $\mu\text{Sv}_n/\text{Gy}_x$, and 1.4 ± 0.2 $\mu\text{Sv}_n/\text{Gy}_x$ respectively.

In Table 5.9 the measured values for neutron dose equivalent from epithermal and thermal neutrons from detectors exposed to 10 MV_p x-rays at 0 cm off-axis at depths 0, 5, and 10 cm were 0.1 ± 0.1, 0.1 ± 0.1, and 0 $\mu\text{Sv}_n/\text{Gy}_x$, respectively. As depth increased the neutron dose equivalent decreased. This was observed in those detectors exposed at 20 and 40 cm off-axis at a depth of 10 cm. Those values are 0.1 ± 0.1, and 0 $\mu\text{Sv}_n/\text{Gy}_x$, respectively.

Table 5.10 shows the measured values for dose equivalent from thermal and epithermal neutrons measured, in TRNDs exposed in 6 MV_p x-ray beam. The neutron dose equivalent was found to be zero within error bars again verifying the threshold for photo-neutrons being about 7 MeV.

Table 5.9 Neutron fluence and dose equivalent measured in CR-39 TRND exposed to an 10 MV_p x-ray beam at varying depths and distances off-axis in the phantom.

Distance off-Axis (cm)	**Depth cm**	**Classification of Neutron Type**	**Normalized Fluence (10^3 cm^{-2} Gy^{-1})**	**Normalized Dose Equivalent ($\mu Sv_n/Gy_x$)**
0	0	Thermal	3.1±0.2	0.1±0.1
0	0	Epithermal	0.2±0.1	0
0	0	High Energy	21.5±3.6	61±43
		Total	**24.9±3.8**	**61±43**
0	5	Thermal	2.7±0.2	0.1±0.1
0	5	Epithermal	0.2±0.1	0
0	5	High Energy	9.2±2.7	11±36
		Total	**12.1±3.0**	**11±36**
0	10	Thermal	1.4±0.1	0
0	10	Epithermal	0	0
0	10	High Energy	0.6±2.5	2±37
		Total	**1.9±2.6**	**2±37**
20	10	Thermal	1.9±0.2	0.1±0.1
20	10	Epithermal	0.1±0.1	0
20	10	High Energy	3.2±2.6	10±37
		Total	**5.28±3.0**	**10±37**
40	10	Thermal	1.0±0.1	0
40	10	Epithermal	0.1±0.1	0
40	10	High Energy	2.2±2.6	13±37
		Total	**3.3±2.6**	**13±37**

Table 5.10 Neutron fluence and dose equivalent measured in CR-39 TRND exposed to an 6 MV_p x-ray beam at varying depths and distances off-axis in the phantom.

Distance off-Axis (cm)	**Depth cm**	**Classification of Neutron Type**	**Normalized Fluence (10^3 cm^{-2} Gy^{-1})**	**Normalized Dose Equivalent ($\mu Sv_n/Gy_x$)**
0	0	Thermal	0	0
0	0	Epithermal	0	0
		Total	**0**	**0**
0	5	Thermal	0.3±0.1	0
0	5	Epithermal	0	0
		Total	**0.4±.1**	**0**
0	10	Thermal	0	0
0	10	Epithermal	0.2±0.1	0
		Total	**0.2±0.1**	**0**
20	10	Thermal	0	0
20	10	Epithermal	0.2±0.1	0
		Total	**0.2±0.1**	**0**
40	10	Thermal	0	0
40	10	Epithermal	0.3±0.1	0
		Total	**0.3±0.1**	**0**

CHAPTER 6

DISCUSSION AND CONCLUSIONS

This study's primary objective was to measure absorbed dose and dose equivalent from photo-neutrons produced by x-ray radiotherapy linear accelerators operating at energies of 6, 10, and 18 MV_p. For 6 and 18 MV_p x-ray beams, a Varian Clinac 23EX was used, while a Varian Trilogy linac was used for a 10 MV_p x-ray beam. These x-ray energies were chosen to represent the higher and lower range of x-ray energies commonly used in radiotherapy where photo-neutron production can occur. The 6 MV_p x-ray beam was included to verify that photo-neutron production does not occur at x-ray energies below about 7 MeV. This study was carried out using CR-39 PNTDs for the measurement of high energy (> 1 MeV) neutrons and TRNDs for the measurement of thermal and epithermal (< 1 MeV) neutrons. The measurements were made with two experimental setups: in air and inside a polyethylene phantom. The field size of each beam was 15 x 15 cm^2 and the surface of either the phantom or treatment table was set at 100 cm SSD.

In general, for both experimental setups (in air and in a phantom), the normalized absorbed dose and dose equivalent from photo-neutrons produced by a medical linear accelerator decreased with increasing distance off-axis and increasing depth from the beam's isocenter.

Table 6.1 lists the experimental results for maximum and minimum absorbed dose and dose equivalent measurements of photo-neutrons in the phantom and in air. In this study, the experimentally measured absorbed dose ranged from 6 ± 3 $\mu Gy_n/Gy_x$ to 495 ± 29 $\mu Gy_n/Gy_x$ for the 18 MV_p x-ray beam, 0.2 ± 2 $\mu Gy_n/Gy_x$

to 10 ± 3 $\mu Gy_n/Gy_x$ for the 10 MV_p x-ray beam, and 0 $\mu Gy_n/Gy_x$ for the 6 MV_p x-ray beam.

Table 6.1 The maximum and minimum values for neutron absorbed dose and dose equivalent measured in CR-39 PNTD and exposed in air and in a phantom to x-ray beams of different energies (10 and 18 MV_p).

Maximum	**Normalized**		**Normalized**	
X-Ray Energy	**Absorbed Dose**		**Dose Equivalent**	
MV_p	$\mu Gy_n/Gy_x$		$\mu Sv_n/Gy_x$	
	Minimum	**Maximum**	**Minimum**	**maximum**
18	6 ± 3	495 ± 29	47.4 ± 43.1	5500 ± 420
10	0.2 ± 2	10 ± 3	2 ± 37	103 ± 46

The dose equivalent measurements for this study ranged from 47.4 ± 43.1 $\mu Sv_n/Gy_x$ to 5500 ± 420 $\mu Sv_n/Gy_x$ for the 18 MV_p x-ray beam, 2 ± 37 $\mu Sv_n/Gy_x$ to 103 ± 46 $\mu Sv_n/Gy_x$ for the 10 MV_p x-ray beam and 0 $\mu Sv_n/Gy_x$ for the 6 MV_p x-ray beam.

Those detectors that were exposed in air measured absorbed dose and dose equivalent values higher than those detectors exposed inside the phantom. The higher absorbed dose and dose equivalent in air suggest that photo-neutron fluxes are attenuated as they propagate through the phantom.

Those detectors exposed inside of the phantom also measured a higher contribution from high LET particles than those detectors exposed in air. This suggests that the incident photo-neutrons are interacting with high-Z matter through non-elastic means such as compound nucleus formation and target fragmentation.

Low energy (< 1 MeV) neutrons, as measured by the TRNDs, do not make an appreciable contribution to the overall absorbed dose or dose equivalent. Low energy neutrons in this study accounted for less than 1% of the dose equivalent.

Photo-neutrons are not produced at x-ray energies below about 7 MeV. As the x-ray energy increases the rate of photo-neutron production also increases.

This study suggests that the absorbed dose and dose equivalent from photo-neutrons produced in a common medical linear accelerator operating at energies 10 and 18 MV_p range from 0.2 $\mu Gy_n/Gy_x$ and 2 $\mu Sv_n/Gy_x$ to 495 $\mu Gy_n/Gy_x$ and 5500 $\mu Sv_n/Gy_x$, respectively.

A comparison of the experimentally measured data for dose equivalent in this study is made with published literature. There have been relatively few experiments or Monte Carlo simulations quantifying photo-neutron absorbed dose or dose equivalent from linacs published in professional literature [Liu et al., 1997; Zanini et al., 2004; Ongaro et al., 2000]. Articles have been published measuring the photo-neutron spectrum produced by medical linacs [Barquero et al., 2002; Facure et al., 2005; Holeman et al., 1977; Howell et al., 2006; Howell et al., 2009; Naseri and Mesbahi, 2010; Kralik and Truek, 2004; Kralik et al., 2008; Reft et al., 2006], neutron-induced activation in and around medical linacs [Fischer et al., 2006; McGinely and Landry, 1989; Howell et al., 2009], and estimates or measurements of photo-neutron fluence from medical linacs [Howell et al., 2006; Kray et al., 2005; Mameli et al., 2008; Mesbai et al., 2010; Mesbahi et al., 2011; Mesbahi, 2009; Howell et al., 2009; Naseri and Mesbahi, 2010; Kralik and Truek, 2004; Kralik et al., 2008]. However, in all of these cases it is difficult to know how to interpret the data in terms of damage from photo-neutron exposure to living tissue either inside or outside the treatment volume.

Some papers quantify photo-neutron production in a medical linear accelerator in terms of the dosimetric quantity of ambient dose equivalent, $H^*(10)$ [Liu et al., 1997] [Zanini et al., 2004] [Agosteo et al., 1993] [Howell et al., 2009] [Kralik et al., 2008]. Ambient dose equivalent is the dose equivalent that would be produced by the corresponding expanded and aligned field, in the 30 cm diameter ICRU sphere at a depth of 10 cm on the radius opposing the direction of the aligned field [ICRU, 1993]. Because dose equivalent and ambient dose equivalent are two different quantities, technically speaking, they should not be directly compared. However, according to

a study from Halg et. al. where equivalent dose and ambient dose equivalent were calculated using Monte Carlo radiation transport code FLUKA, for neutrons of energy ranging from 10^{-7} to 10^{3} MeV using 13 monoenergetic beams the values of these two quantities are nearly the same [Halg et al., 2011]. Halg et.ãl. showed that the largest difference between the equivalent dose and ambient dose equivalent is less than 4%. Since this difference is much smaller than the uncertainty of individual neutron dosimetric measurements (about 35-50%) [NCRP, 1991; NCRP, 2005; NRC, 1977; ANSI, 1976], neutron ambient dose equivalent can be considered practically identical to equivalent dose [Halg et al., 2011]. In this study based on ICRP publication 60 [ICRP, 1991] an assumption is made that equivalent dose and dose equivalent are practically interchangeable. The term 'dose equivalent' will be used to signify the photo-neutron dose equivalent, equivalent dose, and ambient dose equivalent reported in the literature.

6.1 Comparison with Published Data

Comparisons of the photo-neutron dose equivalent measured in this present work with photo-neutron dose equivalent values reported in other literature are shown in Tables, 6.2, 6.3, 6.4, and 6.5. These tables show the measured values of photo-neutron dose equivalent from neutron sensitive detectors exposed to either 18 MV_p x-rays or 10 MV_p x-rays in air and/or in a phantom.

Since neutron dose equivalent varies between different linacs and radiation therapy setups (field size, distance off-axis, depth, etc.), a direct comparison is often not strictly valid. However, a comparison can be made to indicate that the photo-neutron dose equivalent with varying setups is of a similar order.

Neutron sensitive detectors used in other experiments include superheated emulsion detectors (bubble detectors), gold activation foils, polycarbonate films, thermoluminescence detectors (TLDs), and CR-39 PNTDs processed by electrochemical etching

(ECE).

It is important to note that CR-39 PNTD processed by ECE is a very different method than that used in this research. The method of electrochemical etching is a way to enlarge the nuclear tracks up to a size where they can be observed with the naked eye [Najjar et al., 1978]. This method allows for easy viewing of the nuclear tracks using an optical microscope with low magnification and the tracks can be easily counted using an automated scanning system [Najjar et al., 1978].

In electrochemical etching an alternating voltage is applied between two electrodes placed on either side of the detector during the etching process. The electric field caused by the alternating voltage enhances the etching process to the latent damage trail. Soon after the etching process, conical track begin to form. The electric field at the tips of these tracks are much larger than the average field applied to the bulk of the detector. These high electric fields at the tips of the tracks will cause a localized electrical breakdown causing a tree or star like shape to form at the end of the etched track, enhancing the size of each track [Tommasino and Armellini, 1973]. The electrical breakdown, causing the tree or star like shape, will permanently distort the track causing all information, including the LET of the track, to be lost. The ECE method does not allow for energy discrimination between etched tracks [Fulvio et al., 2013].

Each detector mentioned above functions differently. However, the technique used to measure neutron dose equivalent is roughly the same in all detectors in that the neutron fluence measured in each detector is multiplied by a fluence to dose equivalent conversion coefficient to obtain the dose equivalent.

The approach used in this work differs from the efforts mentioned above in that, with CR-39 PNTD processed by standard (non-electrochemical) etching the size of each individual track is proportional to the LET of the particle which formed the track, allowing for the energy deposited by the incident photo-neutron to be measured (Sections 3.4). By measuring track size of the recoil particles, the energy deposited by

neutrons can be measured with a fair amount of accuracy [Benton, 2004; Zhou, 2012].

CR-39 PNTD is a polymer whose an elemental composition ($C_{12}H_{18}O_7$) is a good representation of human tissue. When neutrons transfer their energy to charged particles through elastic or inelastic collisions in the CR-39 PNTD, absorbed dose and dose equivalent in tissue can be measured.

Unlike PNTDs, the other neutron-sensitive detectors do not measure the energy deposited by each neutron. The measured neutron fluence, is multiplied by a fluence to dose equivalent or fluence to ambient dose equivalent conversion coefficient to determine the photo-neutron dose equivalent or ambient dose equivalent. In using this approach, it is assumed that all neutron interactions transfer the same average energy to charged particles. Consequently, using a single conversion factor or multiple conversion factors over a wide range of neutron energies to calculate dose equivalent or ambient dose equivalent introduces large uncertainties.

The conversion coefficients themselves introduce limitations in the way they are calculated. Neutron fluence to dose equivalent or ambient dose equivalent conversion coefficients are calculated under a variety of conditions with various radiation transport codes, in different phantoms, at different depths in a phantom and in different irradiation geometries [McDonald et al., 1998]. The conversion factors associated with each energy interval of the spectrum are obtained from the data set by logarithmic interpolation [Sims and Killough, 1983]. The interpolated conversion factors, along with the convolution of the neutron fluence, produces the spectrum averaged fluence to dose equivalent factor [Sims and Killough, 1983]. Each different organization (ICRP, ICRU, NCRP, etc.) uses different neutron cross sections along with their own methods (Monte Carlo radiation transport code and interpolations) to determine the neutron dose equivalent conversion coefficients as can be shown in Figure 3.3 [McDonald et al., 1998].

The approach used in this work contains a number of advantages over the methods

described above. One major advantage is that the LET of each recoil track produced as the result of an incident neutron interaction, is measured directly and the LET of the secondary particle produced is determined [Benton, 2004]. This method is model independent since it does not rely on Monte Carlo-based fluence to dose equivalent conversion coefficients.

As shown in Table 6.2, Jaradat and Biggs [Jaradat and Biggs, 2008] conducted a study using a Varian 2100C/D linac with a 10 MV_p x-ray beam. They calculated the dose equivalent using bubble detectors for various field sizes between 0.3 x 0.3 cm^2 and 40 x 40 cm^2. The average dose equivalent was determined for the detectors placed directly in the beam (0 cm off-axis) at 100 cm SSD. Jaradat and Biggs reported an average neutron dose equivalent of 0.124 mSv_n/Gy_x. In the present study neutron dose equivalent for a detector placed directly in the beam at 100 SSD exposed to a 10 MV_p x-ray beam of field size 15 x 15 cm^2 is 0.103 mSv_n/Gy_x. Neutron dose equivalent measured by Jaradat and Biggs differs by 20% with that measured in this study. Taking into effect the large (∼35-50%) uncertainty [NCRP, 1991; NCRP, 2005; NRC, 1977; ANSI, 1976] in neutron dosimetry and differences in methods these two values can be considered to agree with each other. The slight differences in these values are also likely affected by to the different radiation therapy setups (field size) and machines used in the two experiments.

Most published literature state that photo-neutron production does not begin until x-ray energies exceed 10 MeV [Facure et al., 2005; Followill et al., 2003; Kralik et al., 2008; Sanchez-Doblado et al., 2012; Barquero et al., 2005; Spurny et al., 1996; Takam et al., 2001]. For this reason there is a lack of photo-neutron dose equivalent data for 10 MV_p x-ray beams. However, as can be seen in Table 6.2 from measurements from Jaradat and Biggs and this work, neutron dose equivalent in 10 MV_p x-ray beams is not negligible and further work should be conducted at this low energy.

Table 6.3 compares photo-neutron dose equivalent measurements from this work

Table 6.2 Comparison of this work with previously published results. All detectors were exposed in air to an 10 MV_p x-ray beam. This table is ordered by distance off-axis and depth.

Reference	**Detectors**	**Machine**	**Field Size** (cm^2)	**Distance off-axis** (cm)	**Depth** (cm)	**Dose** (mSv_n/Gy_x)
Present Work	CR-39 PNTD	Varian Trilogy	15 x 15	0	0	0.103†
[Jaradat and Biggs, 2008]	Bubble Detector	Varian 2100C/D	avg	0	0	0.124†
Present Work	CR-39 PNTD	Varian Trilogy	15 x 15	20	0	0.03†
Present Work	CR-39 PNTD	Varian Trilogy	15 x 15	40	0	0.03†

† Dose Equivalent

with dose equivalent measured from the published literature made in air to an 18 MV_p x-ray beam. Three other research groups have published photo-neutron dose equivalent data for detectors exposed directly in the x-ray beam. Howell et al. [Howell et al., 2006] and Jaradat and Biggs [Jaradat and Biggs, 2008] both measured the average photo-neutron dose equivalent at varying field sizes, while Hashemi et al. [Hashemi et al., 2008] measured the photo-neutron dose equivalent using a field size of 20 x 20 cm^2. Howell et al. and Jaradat and Biggs measured dose equivalent values of 3.13 and 3.5 mSv_n/Gy_x, respectively. Hashemi et al. measured 3.7 mSv_n/Gy_x. In this work, the measured photo-neutron dose equivalent from the detector directly in a 15 x 15 cm^2 x-ray beam was 5.5 mSv_n/Gy_x. The neutron dose equivalent measured by Hashemi et al., Howell et al., and Jareadat and Biggs differs with this study by 33, 43, and 36%, respectively. These values seem fairly comparable when taking into effect the high uncertainties involved in neutron dosimetry, and may well reflect differences in methods and exposure setups.

The neutron dose equivalent measured from the detector located at 20 cm off-axis from isocenter, in this work, is 1.4 mSv_n/Gy_x. Other researchers have published photo-neutron dose equivalent for detectors located about the same distance off-axis to that of this work ($\pm$ 10 cm). Hashemi et al. and Paredes et al. both used a field size of 20 x 20 cm^2. Hashemi et al. measured a photo-neutron dose equivalent of 2.4 mSv_n/Gy_x at 10 cm off-axis, 71% higher than this study, while Paredes et al. measured 2.3 mSv_n/Gy_x at 30 cm off-axis, 64% higher than this study. Barquero et al. measured the neutron dose equivalent at 25, 25, and 30 cm off-axis to isocenter of 0.64, 0.86, and 0.35 mSv_n/Gy_x, respectively, in a 40 x 40 cm^2 x-ray beam. Neutron dose equivalent measured by Barquero et al. differs by 54, 39, and 75% with that measured in the current study. This again is probably due to differences in the method, setup, and especially from varying the distances off-axis by $\pm$ 10 cm.

Howell et al. [Howell et al., 2009] measured the photo-neutron fluence using gold

Table 6.3 Comparison of this work with previously published results. Photo-neutron dose equivalent[†] or ambient dose equivalent[‡] is measured from neutron sensitive detectors mentioned in the table. All detectors were exposed in air to an 18 MV_p x-ray beam. This table is categorized by distance off-axis, and depth.

Reference	**Detectors**	**Machine**	**Field Size** (cm^2)	**Distance off-axis** (cm)	**Depth** (cm)	**Dose** (mSv_n/Gy_x)
Present Work	CR-39 PNTD	Varian 23EX	15 x 15	0	0	5.5[†]
[Hashemi et al., 2008]	Polycarbonate films	Elekta SL75/25	20 x 20	0	0	3.7[†]
[Howell et al., 2006]	Gold Foil Activation	Varian Trilogy	avg	0	0	3.13[‡]
[Jaradat and Biggs, 2008]	Bubble Detector	Varian 2100C/D	avg	0	0	3.5[†]
[Hashemi et al., 2008]	Polycarbonate films (ECE)	Elekta SL75/25	20 x 20	5	0	3.4[†]
[Hashemi et al., 2008]	Polycarbonate films (ECE)	Elekta SL75/25	20 x 20	10	0	2.4[†]
Present Work	CR-39 PNTD	Varian 23EX	15 x 15	20	0	1.40[†]
[Barquero et al., 2002]	TLDs	Siemens KD-S	40 x 40	25	0	0.86[†]
[Barquero et al., 2002]	TLDs	Siemens KD-S	40 x 40	25	0	0.64[†]
[Paredes et al., 1999]	CR-39 (ECE)	Varian 2100C	20 x 20	30	0	2.3[†]
[Barquero et al., 2002]	TLDs	Siemens KD-S	40 x 40	30	0	0.35[†]
[Howell et al., 2009]	Gold Foil Activation	Varian 21EX	0 x 0	40	0	1.3[‡]
[Howell et al., 2009]	Gold Foil Activation	Precise	0 x 0	40	0	0.55[‡]
[Howell et al., 2009]	Gold Foil Activation	Oncor	0 x 0	40	0	0.38[‡]
[Howell et al., 2009]	Gold Foil Activation	Varian 21EX	0 x 0	40	0	1.9[‡]
[Howell et al., 2009]	Gold Foil Activation	Precise	0 x 0	40	0	0.84[‡]
[Howell et al., 2009]	Gold Foil Activation	Oncor	0 x 0	40	0	0.52[‡]
Present Work	CR-39 PNTD	Varian 23EX	15 x 15	40	0	0.84[†]
[Kralik et al., 2008]	Bonner,CR-39 (ECE)	Varian 2100C/D	10 x 10	50	0	0.022[‡]
[Kralik et al., 2008]	Bonner,CR-39 (ECE)	Varian 2100C/D	20 x 20	50	0	0.021[‡]
[Hashemi et al., 2008]	Polycarbonate films (ECE)	Elekta SL75/25	20 x 20	50	0	0.8[†]
[Kralik et al., 2008]	Bonner,CR-39 (ECE)	Varian 2100C/D	30 x 30	50	0	0.025[‡]
[Hashemi et al., 2008]	Polycarbonate films (ECE)	Elekta SL75/25	20 x 20	100	0	0.2[†]

[†] Dose Equivalent, [‡] Ambient Dose Equivalent

foil activation detectors located 40 cm off-axis in various linacs with a field size of 0 x 0 cm^2. From the neutron fluence, Howell et al. calculated the ambient dose equivalent using methods discussed in ICRP-21 and ICRP-74. Those results are 1.3, 0.55, 0.38 mSv_n/Gy_x for ICRP-21 conversion coefficients and 1.96, 0.84, and 0.52 mSv_n/Gy_x for ICRP-74 conversion coefficients. In this work, the measured photo-neutron dose equivalent from the detector at 40 cm off-axis is 0.84 mSv_n/Gy_x. The photo-neutron dose equivalent from the Varian 21EX linac in Howell et al. (1.9, and 1.3 mSv_n/Gy_x) differs with that in this research by factors of 2.3 and 1.5, respectively. In Howell et al., the Varian 21EX linac measured the highest value for neutron dose equivalent. The photo-neutron dose equivalent from the Precise linac measured using ICRP-21 and ICRP-74 conversion coefficients was 0.55 and 0.84 mSv_n/Gy_x, respectively. 0.38 and 0.52 mSv_n/Gy_x was measured for the Oncor linac using ICRP-21 and ICRP-74 coefficients, respectively. The ICRP-21 coefficients (0.55 and 0.38 mSv_n/Gy_x) differed from that of this study by 35 and 55%, respectively. The neutron dose equivalent measured using ICRP-74 coefficients (0.84 and 0.52 mSv_n/Gy_x) seemed to agree well with that of this study, differing by only 0, and 38%, respectively. From Howell et al. it can be seen that using model-based conversion coefficients to determine dose equivalent introduces large uncertainties. Measurements of LET spectra in CR-39 PNTD is again model independent which bypasses these uncertainties resulting in more accurate measurements.

Kralik et al. [Kralik et al., 2008] and Hashemi et al. [Hashemi et al., 2008] measured the neutron dose equivalent at 50 cm off-axis from isocenter. Kralik et al. exposed their detectors in field sizes of 10 x 10 cm^2 and 20 x 20 cm^2 and measured values of 0.22 and 0.21 mSv_n/Gy_x, respectively. Neither value agreed with this study's results, differing by 97%. Hashemi et al., using a 20 x 20 cm^2 field size, measured 0.8 mSv_n/Gy_x, which only differs by 5% with the this study's measurements located at 40 cm off-axis from isocenter.

Table 6.4 Comparison of this work with previously published results. All detectors were exposed in a phantom to an 10 MV_p x-ray beam. This table is ordered by distance off-axis and depth.

Reference	**Detectors**	**Machine**	**Field Size** (cm^2)	**Distance off-axis** (cm)	**Depth** (cm)	**Dose** (mSv_n/Gy_x)
Present Work	CR-39 PNTD	Varian Trilogy	15 x 15	0	0	0.061†
[d'Errico et al., 2001]	Bubble Detectors, CR-39 (ECE)	Varian Clinac	10 x 10	0	1	1.4†
[d'Errico et al., 2001]	Bubble Detectors, CR-39 (ECE)	Varian Clinac	10 x 10	0	5	0.9†
Present Work	CR-39 PNTD	Varian Trilogy	15 x 15	0	5	0.011†
[d'Errico et al., 2001]	Bubble Detectors, CR-39 (ECE)	Varian Clinac	10 x 10	0	10	0.6†
Present Work	CR-39 PNTD	Varian Trilogy	15 x 15	0	10	0.002†
Present Work	CR-39 PNTD	Varian Trilogy	15 x 15	20	10	0.01†
Present Work	CR-39 PNTD	Varian Trilogy	15 x 15	40	10	0.013†
[d'Errico et al., 2001]	Bubble Detectors, CR-39 (ECE)	Varian Clinac	10 x 10	50	1	0.03†
[d'Errico et al., 2001]	Bubble Detectors, CR-39 (ECE)	Varian Clinac	10 x 10	50	5	0.01†
[d'Errico et al., 2001]	Bubble Detectors, CR-39 (ECE)	Varian Clinac	10 x 10	50	10	0†

† Dose Equivalent

Table 6.4 shows a comparison between this work's measurements from CR-39 PNTDs in a phantom exposed to a 10 MV_p x-ray beam with that of (d'Errico et al. [d'Errico et al., 2001]) bubble detectors exposed to the same x-ray energy inside a phantom. This study measured the neutron dose equivalent at 0 cm off-axis and 0 cm depth to be 0.061 mSv_n/Gy_x, while 1.4 mSv_n/Gy_x was measured at 0 cm off-axis and 1 cm depth by d'Errico et al., a disagreement of a factor of 23. For this study the neutron dose equivalent measured from the detectors located at 0 cm off-axis and at depths of 5 and 10 cm were 0.011 mSv_n/Gy_x, and 0.002 mSv_n/Gy_x, respectively. d'Errico et al. measured significantly higher values for the neutron dose equivalent at 0 cm off-axis and at a depths of 5 and 10 cm, 0.9 mSv_n/Gy_x and 0.6 mSv_n/Gy_x, respectively. These values disagree with this study by a factor of 82 for the detectors directly in the beam at a depth of 5 cm and a factor of 300 for the detectors directly in the beam at a depth of 10 cm.

Table 6.5 compares photo-neutron dose equivalent from this work with dose equivalent from d'Errico et al. [d'Errico et al., 1998] and dErrico et al. [d'Errico et al., 2001]. All detectors were exposed in a phantom to an 18 MV_p x-ray beam. In this work the measured photo-neutron dose equivalent from the detector directly in a 15 x 15 cm^2 x-ray beam is 4.3 mSv_n/Gy_x. The neutron dose equivalent measured by d'Errico et al. (98) and d'Errico et al. (01) from the detectors in the same locations differed from that of this study by 5% and 28%, respectively. The detectors located at 0 cm off-axis at a depth of 5 cm, in this work, measured neutron dose equivalent to be 1.5 mSv_n/Gy_x. d'Errico et al. (98) and d'Errico et al. (01) measured the neutron dose equivalent from the detectors in the same locations to be 2.5 and 4.1 mSv_n/Gy_x, respectively. These results are 67% and 173% higher than this study. The reason for the discrepancy in these values could be due to the different radiation therapy setups between the two experiments, as well as differences in methods.

For the detectors located 0 cm off-axis at a depth of 10 cm, the measured neu-

tron dose equivalent for this work was 0.55 mSv_n/Gy_x. d'Errico et al. (98) and d'Errico et al. (01) measured the neutron dose equivalent from the detectors in the same locations to be 1.5 and 2.4 mSv_n/Gy_x, respectively. These results differ by 173% and 336%, to the results measured in this study.

For the detector located 20 cm off-axis at a depth of 10 cm, the measured neutron dose equivalent for this work was 0.17 mSv_n/Gy_x. d'Errico et al. (98) measured the neutron dose equivalent from the detectors in the same locations to be 0.2 mSv_n/Gy_x, an 18% difference compared to this work.

Table 6.6 shows the photo-neutron dose equivalent calculated by Monte Carlo simulations. The simulations were preformed modeling a radiotherapy linac using a 10 or 18 MV_p x-ray beam in air at varying the distances off-axis. These values are compared to the measured neutron dose equivalent values measured using CR-39 PNTDs exposed to a 10 and 18 MV_p x-ray beam at the same or comparable distances off-axis in this study. The neutron dose equivalent measured from CR-39 PNTD located directly in the 10 MV_p x-ray beam was 0.103 mSv_n/Gy_x. Liu et al. [Liu et al., 1997] used a Monte Carlo radiation transport codes EGS, and MORSE to calculate the neutron dose equivalent of 0.02 mSv_n/Gy_x. Liu et al.'s result disagrees with our study by a factor of 5.2. The results from Monte Carlo simulation depend on the input data and parameters. Since these parameters are not specifically known, it is hard to determine why these two values disagree.

The neutron dose equivalent measured from the CR-39 PNTD located directly in the 18 MV_p x-ray beam was 5.5 mSv_n/Gy_x. Liu et al. [Liu et al., 1997], Zanini et al. [Zanini et al., 2004], and Ongaro et al. [Ongaro et al., 2000] calculated the neutron dose equivalent from an 18 MV_p x-ray beam in the same location to be 1.5, 2.35, and 4.8 mSv_n/Gy_x, respectively. The result in this study agree quite well with that of Ongaro et al. (13%). Liu et al. and Zanini et al. do not agree so well with this study's result, differing by 73 and 57%, respectively.

Table 6.5 Comparison of this work with previously published results. All detectors were exposed in a phantom to an 18 MV_p x-ray beam. This table is ordered by distance off-axis and depth.

Reference	**Detectors**	**Machine**	**Field Size** (cm^2)	**Distance off-axis** (cm)	**Depth** (cm)	**Dose** (mSv_n/Gy_x)
[Vanhavere et al., 2004]	Bubble Detectors	Varian Clinac	10 x 10	0	0	8.0*
Present Work	CR-39 PNTD	Varian 23EX	15 x 15	0	0	4.3†
[d'Errico et al., 1998]	Bubble Detectors, CR-39 (ECE)	Saturne 20	10 x 10	0	1	4.5†
[d'Errico et al., 2001]	Bubble Detectors, CR-39 (ECE)	Varian Clinac	10 x 10	0	1	5.5†
[d'Errico et al., 1998]	Bubble Detectors, CR-39 (ECE)	Saturne 20	10 x 10	0	5	2.5†
[Vanhavere et al., 2004]	Bubble Detectors	Varian Clinac	10 x 10	0	5	4.6*
[d'Errico et al., 2001]	Bubble Detectors, CR-39 (ECE)	Varian Clinac	10 x 10	0	5	4.1†
Present Work	CR-39 PNTD	Varian 23EX	15 x 15	0	5	1.5†
[d'Errico et al., 1998]	Bubble Detectors, CR-39 (ECE)	Saturne 20	10 x 10	0	10	1.5†
[Vanhavere et al., 2004]	Bubble Detectors	Varian Clinac	10 x 10	0	10	3.8*
[d'Errico et al., 2001]	Bubble Detectors, CR-39 (ECE)	Varian Clinac	10 x 10	0	10	2.4†
Present Work	CR-39 PNTD	Varian 23EX	15 x 15	0	10	0.55†
[Vanhavere et al., 2004]	Bubble Detectors	Varian Clinac	10 x 10	0	15	2.5*
[d'Errico et al., 1998]	Bubble Detectors, CR-39 (ECE)	Saturne 20	10 x 10	10	1	2.05†
[d'Errico et al., 1998]	Bubble Detectors, CR-39 (ECE)	Saturne 20	10 x 10	10	5	0.8†
[d'Errico et al., 1998]	Bubble Detectors, CR-39 (ECE)	Saturne 20	10 x 10	10	10	0.3†
[d'Errico et al., 1998]	Bubble Detectors, CR-39 (ECE)	Saturne 20	10 x 10	20	1	1.75†
[d'Errico et al., 1998]	Bubble Detectors, CR-39 (ECE)	Saturne 20	10 x 10	20	5	0.6†
[d'Errico et al., 1998]	Bubble Detectors, CR-39 (ECE)	Saturne 20	10 x 10	20	10	0.2†
Present Work	CR-39 PNTD	Varian 23EX	15 x 15	20	10	0.17†
Present Work	CR-39 PNTD	Varian 23EX	15 x 15	40	10	0.046†
[d'Errico et al., 2001]	Bubble Detectors, CR-39 (ECE)	Varian Clinac	10 x 10	50	1	1.9†
[d'Errico et al., 2001]	Bubble Detectors, CR-39 (ECE)	Varian Clinac	10 x 10	50	5	1.1†
[d'Errico et al., 2001]	Bubble Detectors, CR-39 (ECE)	Varian Clinac	10 x 10	50	10	0.5†

† Dose Equivalent, * Equivalent Dose

The neutron dose equivalent measured 20 cm off-axis in this study was 1.4 mSv_n/Gy_x. Ongaro et al. calculated the neutron dose equivalent from an 18 MV_p x-ray beam in the same location to be 2.3 mSv_n/Gy_x, a difference of 64%. Again, since the results from Monte Carlo simulations depend on the input data and parameters, it is difficult to know how comparable these results should be.

6.2 Future Work

The results from this study and those in the published literature are all of a similar order of magnitude, indicating broad agreement. The differences between this study's measurements of neutron dose equivalent compared to other study's dose equivalent measurements are due to many reasons. The major source of disagreement is likely the different methods used to measure the dose equivalent produced by photo-neutrons. Other sources of disagreement include differences in measurement/calculation location, difference in setup especially field size, and difference between different model radiotherapy lincas.

All studies mentioned show that photo-neutron production does occur in higher energy linacs (> 10 MV_p) and cannot be considered negligible. The photo-neutrons, produced from high energy linacs impose a risk of secondary cancers induction. This risk must be assessed and weighed against the benefits of radiotherapy. For this reason it is important to accurately quantify the absorbed dose and corresponding dose equivalent from secondary neutrons, especially to healthy tissue surrounding the treatment volume, during x-ray radiotherapy

The need for additional data must be emphasized, particularly with respect to different x-ray energies. This study only focused on the high and low end of x-ray radiotherapy (18 and 10 MVp) and intermediate energies, such as a 15 MV_p x-ray beams would be particularly interesting to analyze.

Additional detector exposures are needed to completely analyze the photo-neutron

Table 6.6 Photo-neutron dose equivalent†, or ambient dose equivalent‡ is measured from a Monte Carlo simulation. This table is categorized by maximum x-ray energy, distance off-axis, and depth.

Reference	**Computer Code**	**Machine**	**Field Size** (cm^2)	**Maximum X-ray Energy** (MV_p)	**Distance off-axis** (cm)	**Depth** (cm)	**Dose** (mSv_n/Gy_x)
Present Work	CR-39 PNTD	Varian Trilogy	15 x 15	10	0	0	0.103†
[Liu et al., 1997]	EGS-MORSE	Varian Clinac 2100C/2300C	0 x 0	10	0	0	0.02‡
Present Work	CR-39 PNTD	Varian 23EX	15 x 15	18	0	0	5.5†
[Liu et al., 1997]	EGS-MORSE	Varian Clinac 2100C/2300C	0 x 0	18	0	0	1.5‡
[Zanini et al., 2004]	MCNP4B-GN	Varian Clinac 2300C/D	10 x 10	18	0	0	2.35‡
[Ongaro et al., 2000]	MCNP4B-GN	Elekta SL20I	10 x 10	18	0	0	4.8†
[Zanini et al., 2004]	MCNP4B-GN	Varian Clinac 2300C/D	10 x 10	18	8	0	1.16‡
[Ongaro et al., 2000]	MCNP4B-GN	Elekta SL20I	10 x 10	18	8	0	3.3†
[Zanini et al., 2004]	MCNP4B-GN	Varian Clinac 2300C/D	10 x 10	18	15	0	1.08‡
[Ongaro et al., 2000]	MCNP4B-GN	Elekta SL20I	10 x 10	18	15	0	2.6†
Present Work	CR-39 PNTD	Varian 23EX	15 x 15	18	20	0	1.40†
[Ongaro et al., 2000]	MCNP4B-GN	Elekta SL20I	10 x 10	18	20	0	2.3†

† Dose Equivalent, ‡ Ambient Dose Equivalent

absorbed dose and dose equivalent at different depths and different distances off-axis. This study used a total of 3 detectors in air (0, 20, and 40 cm off-axis) and 5 detectors in the phantom (0, 5, and 10 cm depth directly in the beam and 20 and 40 cm off-axis at a depth of 10 cm). More detectors placed at various positions in air and in the phantom will give a better understanding of photo-neutron attenuation.

Another important variable in measuring photo-neutron absorbed dose and dose equivalent is field size. This study chose a field size of 15 x 15 cm^2. However, to better understand how field size affects the photo-neutron absorbed dose and dose equivalent, additional data needs to be taken by varying the field size of the linac.

Additional data can be taken by comparing different model linacs. The design of a linac's head differs significantly between different manufactures and even among different model linacs from the same manufacture. Measuring the photo-neutron absorb dose and dose equivalent from different machines with the same x-ray energy will provide important information.

Another aspect in helping to better quantify the absorbed dose and dose equivalent from photo-neutrons is to improve statistics. This can be done by increasing the x-ray dose (MUs) of the linac.

A significant contribution to help understand and measure the photo-neutron absorbed dose and dose equivalent is to simulate the experiment using a Monte Carlo radiation transport code while simultaneously making measurements of neutron induced absorbed dose and dose equivalent for the identical machine and setup. Monte Carlo simulations can have a high degree of precision and detail depending on the accuracy of the input data, and parameters. However, it is important to note that simulation should always be verified against the results from actual measurements and not vice versa.

BIBLIOGRAPHY

[Agosteo et al., 1993] Agosteo, S., Para, A. F., and Maggioni, B. (1993). Neutron fluxes in radiotherapy rooms. *Medical Physics*, 20(2):407–414.

[Allen and Chaudhri, 1982] Allen, P. D. and Chaudhri, M. A. (1982). The dose contribution due to photonuclear reactions during radiotherapy. *Medical Physics*, 9:904–906. Technical Notes.

[ANSI, 1976] ANSI (1976). American national standard for personnel neutron dosimeters (neutron energies less than 20 mev). Technical Report ANSI N319, American National Standard Institue, Inc. for Personnel Neutron Dosimeters.

[Barquero et al., 2005] Barquero, R., Edwards, T. M., Iniguez, M. P., and Carrillo, H. R. V. (2005). Monte carlo simulation estimates of neutron doses to critical organs of a patient undergoing 18 mv x-ray linac-based radiotherapy. *Medical Physics*, 32(12):3579–3588.

[Barquero et al., 2002] Barquero, R., Mendez, R., Iniguez, M. P., Vega, H. R., and Voytchev, M. (2002). Thermoluminescence measurements of neutron dose around a medical linac. *Radiation Protection Dosimetry*, 101(1-4):493–496.

[Benton, 2004] Benton, E. R. (2004). *RADIATION DOSIMETRY AT AVIATION ALTITUDES AND IN LOW-EARTH ORBIT*. PhD thesis, The National University of Ireland.

[Benton et al., 2001] Benton, E. R., Benton, E. V., and Frank, A. L. (2001). Neutron dosimetry in low earth orbit using passive detectors. *Radiation Measurements*.

[Benton et al., 2011] Benton, E. R., Johnson, C. E., DeWitt, J., Yasuda, N., Benton, E. V., Moyer, M. H., and Frank, A. L. (2011). Observations of short-range, high -let recoil tracks in cr-39 plastic nuclear track detector by visible light microscopy. *Radiation Measurements*, 46:527–532.

[Benton and Henke, 1969] Benton, E. V. and Henke, R. P. (1969). Heavy particle range energy relations for dielectric nuclear track detectors. *Nuclear Instruments and Methods*, 67(1):87–92.

[Berman, 1975] Berman, B. L. (1975). Atlas of photoneutron cross section obtained with mono-energetic photons. *Atomic Data and Nuclear Data Tables*, 15:319–390.

[Broerse et al., 1981] Broerse, J. J., Hollander, C. F., and Zwieten, M. J. V. (1981). Tumor induction in rhesus monkeys after total body irradiation with x-rays and fission neutrons. *International Journal of Radiation Biology*, 40:671–676.

[Bruneni, 1997] Bruneni, J. L. (1997). *CR-39 CELEBRATING 50 YEARS, MORE THAN MEETS THE EYE*. PPG Industries Inc.

[Carinou et al., 2005] Carinou, E., Stamatelatos, I. E., Kamenopoulou, V., Gerogolopoulou, P., and Sandilos, P. (2005). A mcnp-based model for the evaluation of the photoneutron dose in high energy medical electron accelerators. *Physica Medica*, XXI(3):95–99.

[Cartwright and Shirk, 1978] Cartwright, B. G. and Shirk, E. K. (1978). A nuclear-track-recording polymer of unique sensitivity and resolution. *Nuclear Instrument and Methods*, 153:457–460.

[Cassou and Benton, 1978] Cassou, R. M. and Benton, E. V. (1978). Properties and applications of cr-39 polymeric nuclear track detector. *Nuclear. Track Detection.*

[Chibani and Ma, 1990] Chibani, O. and Ma, C.-M. C. (1990). Photonuclear dose calculations for high-energy photon beams from siemens and varian linacs. *Medical Physics*, 30:1990–2000.

[Cooper and Hausman, 2009] Cooper, G. M. and Hausman, R. E. (2009). *The cell: a molecular approach*. ASM Press, Washington, D.C., second edition.

[Delaney et al., 2005] Delaney, G., Jacob, S., Featherstone, C., and Barton, M. (2005). The role of radiotherapy in cancer treatment: Estimating optimal utilization from a review of evidence-based clinical guidelines. *Cancer*, 104(6):1129–1137.

[d'Errico et al., 1997] d'Errico, F., Apfel, R. E., Curzio, G., Dietz, E., Egger, E., Gualdrini, G. F., Guldbakke, S., Nath, R., and Siebert, B. R. L. (1997). Superheated emulsions: Neutronics and thermodynamics. *Radiation Protection and Dosimetry*, 70(1-4):109–112.

[d'Errico et al., 2001] d'Errico, F., Luszik-Bhadra, M., Nath, R., Siebert, B. R. L., and Wolf, U. (2001). Depth dose-equivalent and effective energies of photoneutrons generated by 6-18 mv x-ray beams for radiotherapy. *Health Physics Society*, 80(1):4–11.

[d'Errico et al., 1998] d'Errico, F., Nath, R., Tana, L., Curzio, G., and Alberts, W. G. (1998). In-phantom dosimetry and spectrometry of photoneutrons from an 18 mv linear accelerator. *Medical Physics*, 25(9):1717–1724.

[DeVita et al., 1979] DeVita, V. T., Oliverio, V. T., and Muggia, F. M. (1979). The drug development and clinical trials programs of the division of cancer treatment. *National Cancer Institute*, pages 195–216.

[Difilippo et al., 2003] Difilippo, F., Papiez, L., Moskvin, V., Peplow, D., DesRosiers, C., Johnson, J., Timmerman, R., m Randall, and Lillie, R. (2003). Contamination

dose from photoneutron processes in bodily tissues during therapeutic radiation delivery. *Medical Physics*, 30(10):2849–2854.

[Facure et al., 2005] Facure, A., Falcao, R. C., Silva, A. X., Crispim, V. R., and Vitorelli, J. C. (2005). A study of neutron spectra from medical linear accelerator. *Applied Radiation and Isotopes*, 62:69–72.

[Fischer et al., 2006] Fischer, H. W., Tabot, B. E., and Poppe, B. (2006). Activation processes in medical linear accelerator and spatial distribution of activation products. *Physics in Medicine and Biology*, 51:461–466.

[Fleischer et al., 1975] Fleischer, R. L., Price, P. B., and Walker, R. M. (1975). *Nuclear Tracks in Solids: Principles and Applications*. University of California Press, Berkeley.

[Followill et al., 2003] Followill, D. S., Stovall, M. S., Kry, S. F., and Ibbott, G. S. (2003). Neutron source strength measurements for varian, siemens, elektra, and general electric linear accelerators. *Applied Clinical Medical Physics*, 4(3):189–194.

[Fulvio et al., 2013] Fulvio, A. D., Domingo, C., Pedro, M. D. S., D'Agostino, E., Caresana, M., Tana, L., and d'Errico, F. (2013). Superheated emulsions and track etch detectors for photoneutron measurements. *Radiation Measurements*, 57:19–28.

[Garnica-Garza, 2005] Garnica-Garza, H. M. (2005). Characteristics of the photoneutron contamination present in a high-energy radiotherapy treatment room. *Physics in Medicine and Biology*, 50:531–539.

[Ghiasi and Mesbahi, 2010] Ghiasi, H. and Mesbahi, A. (2010). Monte carlo characterization of photoneutrons in the radiation therapy with high energy photons: A comparison between simplified and full monte carlo models. *Iranian Journal of Radiation*, 8(3):187–193.

[Goldhaber and Heckman, 1978] Goldhaber, A. S. and Heckman, H. H. (1978). High energy interaction of nuclei. *Annual Review of Nuclear and Particle Science*, 28:161–205.

[Greene and Williams, 1997] Greene, D. and Williams, P. C. (1997). *Linear Accelerators for Radiation Therapy*. Institute of Physics Publication, Bristol, UK, second edition.

[Halg et al., 2011] Halg, R. A., Besserer, J., and Schneider, U. (2011). Comparative simulations of neutron dose in soft tissue and phantom materials for proton and carbon ion therapy with actively scanned beams. *Medical Physics*, 37(154-163).

[Hall and Giaccia, 2006] Hall, E. and Giaccia, A. (2006). *Radiology for the Fadiologis*. Philadelphia, sixth edition.

[Hashemi and Hashemi-Malayeri, 2007] Hashemi, S. M. and Hashemi-Malayeri, B. (2007). A study of the photoneutron dose equivalent resulting from a saturne 20 medical linac using monte carlo method. *Nukleonika*, 52(1):39–43.

[Hashemi et al., 2008] Hashemi, S. M., Hashemi-Malayeri, B., Raisali, G., Shokrani, P., Sharafi, A. A., and Torkzadeh, F. (2008). Measurement of photoneutron dose produced by wedge filters of a high energy linac using polycarbonate films. *Journal of Radiation Research*, 49(3):279–283.

[Henke et al., 1986] Henke, R., Ogura, K., and Benton, E. V. (1986). Standard method for measurement of bulk etch in cr-39. *Nuclear Tracks and Radiation Measurements*, 12:307–310.

[Henke and Benton, 1971] Henke, R. P. and Benton, E. V. (1971). On geometry of tracks in dielectric nuclear track detectors. *Nuclear Instruments and Methods*, 97:483–489.

[Hess and Eugster, 1949] Hess, V. F. and Eugster, J. (1949). *Cosmic Radiation and its Biological Effects*. Fordham University Press, New York, NY, second edition.

[Hirayama, 2000] Hirayama, H. (2000). Lecture notes of photon interaction and cross sections.

[Holeman et al., 1977] Holeman, G. R., Price, K. W., Friedman, L. F., and Nath, R. (1977). Neutron spectral measurements in and intense photon field associated with a high x-ray radiotherapy machine. *Medical Physics*, 4(6):508–515.

[Howell, 2010] Howell, R. M. (2010). Neutron interactions part 1. MD Anderson, Houston, TX.

[Howell et al., 2006] Howell, R. M., Hertel, N. E., Wang, Z., Hutchinson, J., and Fullerton, G. D. (2006). Calculation of effective dose from measurements of secondary neutron spectra and scattered photon dose from dynamic mlc imrt for 6 mv, 15 mv, and 18 mv beam energies. *Medical Physics*, 33(2):360–368.

[Howell et al., 2009] Howell, R. M., Kry, S. F., Burgett, E., Hertel, N. E., and Followill, D. S. (2009). Secondary neutron spectra from modern varian, siemens, and elekta linacs with multileaf collimators. *Medical Physics*, 36(9):4027–4038.

[Huda, 2010] Huda, W. (2010). *Review of Radiologic Physics*. Lippincott Williams and Wilkins, Philadelphia, PA 19106, third edition.

[IAEA, 1979] IAEA (1979). Radiological safety aspects of the operation of electron linear accelerators. *International Atomic Energy Agency*, Technical Reports Series(No.188).

[IARC, 2000] IARC (2000). Ionizing radiation, part 1: X- and gamma- radiation, and neutrons. Technical Report 75, International Agency for Research on Cancer, Lyon, France.

[ICRP, 1977] ICRP (1977). Annals of the icrp: Recommendations of the international commission on radiobiological protection. *International Commission on Radiobiological Protection*, ICRP Publication 26. Oxford, MA.

[ICRP, 1982] ICRP (1982). General principles of monitoring for radiation protection of workers. Technical Report 35, International Commission on Radiological Protection, Elmsford, New York.

[ICRP, 1991] ICRP (1991). Recommendations of the international commission on radiobiological protection. *International Commission on Radiobiological Protection,ICRP Publication 60*. Oxford, MA.

[ICRU, 1983] ICRU (1983). Microdosimetry. *Report of the International Commission on Radiation Units and Measurements*, 36.

[ICRU, 1993] ICRU (1993). Quantities and units in radiation protection dosimetry. *International Commission on Radiation Units and Measurements (ICRU)*, 51.

[ICRU, 1998] ICRU (1998). Fundamental quantities and units of ionizing radiation. *International Committee on Radiation Units and Measurements*, ICRP Publication No. 60.

[Islam et al., 2013] Islam, M. R., Collumns, T. L., Zheng, Y., Monson, J. M., and Benton, E. R. (2013). Off-axis dose equivalent due to secondary neutrons from uniform scanning proton beams during proton radiotherapy. *Physics in Medicine and Biology*, 58:8235–8251.

[Jaradat and Biggs, 2008] Jaradat, A. K. and Biggs, P. J. (2008). Measurement of the neutron leakage from a dedicated intraoperative radiation therapy electron linear accelerator and a conventional linear accelerator for 9, 12, 15(16) and 18(20) mev electron energies. *Medical Physics*, 35(5):1711–1717.

[Jeraj and Vlado, 2004] Jeraj, M. and Vlado, R. (2004). Multileaf collimator in radiotherapy. *Radiology and Oncology*, 38(3):235–240.

[Joiner and van der Kogel, 2009] Joiner, M. C. and van der Kogel, A. (2009). *BASIC CLINICAL RADIOBIOLOGY*. Hodder Arnold, London.

[Khan, 2003] Khan, F. M. (2003). *The Physics of Radiation Therapy*. Lippincott Williams and Wilkins, Philadelphia, PA 19106, third edition.

[Kodaira et al., 2007] Kodaira, S., Yasuda, N., Hasebe, N., Doke, T., Ota, S., and Ogura, K. (2007). New method of the precise measurements for the thickness and bulk etch rate of the solid-state track detector. *Nuclear Instrument & Methods in Physics Research*.

[Kralik and Truek, 2004] Kralik, M. and Truek, K. (2004). Characterisation of neutron fields around high-energy x-ray radiotherapy machines. *Radiation Protection Dosimetry*, 100(1-4):503–507.

[Kralik et al., 2008] Kralik, M., Turek, K., and Vondracek, V. (2008). Spectra of photoneutrons produced by high-energy x-ray radiotherapy linacs. *Radiation Protection Dosimetry*, 132(1):13–17.

[Krane, 1988] Krane, K. S. (1988). *Introductory Nuclear Physics*. John Wiley & Sons, Inc, Hoboken, NJ.

[Kray et al., 2005] Kray, S. F., Salehpour, M., Followill, D. S., Stovall, M., Kuban, D. A., White, R. A., and Rosen, I. I. (2005). Out-of-field photon and neutron dose equivalents from step-and-shoot intensity-modulated radiation therapy. *International Journal of Radiation Oncology*, 62(4):1204–1216.

[Liu et al., 1997] Liu, J. C., Kase, K. R., Mao, X. S., Nelson, W. R., Kleck, J. H., and Johnson, S. (1997). Calculations of photoneutrons from varian clinac accelerators

and their transmissions in materials. *Stanford Linear Accelerator Center (SLAC)*, (SLAC-PUB-7404):1–5.

[Ma et al., 2008] Ma, A., Awotwi-Pratt, J., Alghamdi, A., Alfuraih, A., and Spyrou, N. M. (2008). Monte carlo study of photoneutron production in the varian clinac 2100c linac. *Journal of Radio Analytical and Nuclear Chemistry*, 276(1):119–123.

[Mameli et al., 2008] Mameli, A., Greco, F., Fidanzio, A., Fusco, V., Cilla, S., D'Onofrio, G., Grimaldi, L., Augelli, B. G., Giannini, G., Bevilacqua, R., Totaro, P., Tommasino, L., Azario, L., and Piermattei, A. (2008). Cr-39 detector based thermal neutron flux measurements in the photo neutron project. *Nuclear Instruments and Methods in Physics Research*, B 266:3656–3660.

[Martinez-Ovalle et al., 2012] Martinez-Ovalle, S. A., Barquero, R., Gomez-Ros, J. M., and Lallena, A. M. (2012). Neutron dosimetry in organs of an adult human phantom using linacs with multileaf collimator in radiotherapy treatments. *Medical Physics*, 5:2854–2866.

[McDonald et al., 1998] McDonald, J. C., Schwartz, R. B., and Thomas, R. H. (1998). Neutron dose equivalent conversion coefficients have changed in the last forty years...haven't they? *Radiation Protection Dosimetry*, 78(2):147–149.

[McGinely and Landry, 1989] McGinely, P. H. and Landry, J. C. (1989). Neutron contamination of x-ray beam produced by the varian clinac 1800. *Physics of Medicine and Biology*, 34(6):777–783. Technical Note.

[Mesbahi, 2009] Mesbahi, A. (2009). A monte carlo study on neutron and electron contamination of an unflattend 18-mv photon beam. *Applied Radiation and Isotopes*, 67:55–60.

[Mesbahi et al., 2011] Mesbahi, A., Azarpeyvand, A.-A., and Shirazi, A. (2011). Photoneutron production and backscattering in high density concretes used for radiation shielding. *Annals of Nuclear Energy*, 38:2752–2756.

[Mesbai et al., 2010] Mesbai, A., Ghiasi, H., and Mahdavi, S. R. (2010). Photoneutron and capture gamma dose equivalent for different room and maze layouts in radiation therapy. *Radiation Protection Dosimetry*, 140(3):242–249.

[Mukherjee, 2011] Mukherjee, S. (2011). *The Emperor of all Maladies: A Biography of Cancer*. Scribner, New York.

[Najjar et al., 1978] Najjar, S. A. R. A., zar Garcia, M. B., and Durrani, S. A. (1978). A multi-detector electrochemical etching and automatic scanning system. *Nuclear Track Detection*, 2:215–220.

[Naseri and Mesbahi, 2010] Naseri, A. and Mesbahi, A. (2010). A review on photoneutrons characteristics in radiation therapy with high-energy photon beams. *Reports of Practical Oncology and Radiotherapy*, 15:138–144.

[Nath et al., 1984] Nath, R., Epp, E. R., Laughlin, J. S., Swanson, W. P., and Bond, V. P. (1984). Neutrons from high-energy x-ray medical accelerators: An estimate of risk to the radiotherapy patient. *Medical Physics*, 11(3):231–241.

[Nath et al., 1993] Nath, R., Meigooni, A. S., King, C. R., Smolen, S., and d'Errico, F. (1993). Superheated drop detector for determination of neutron dose equivalent to patients undergoing high-energy x-ray and electron radiotherapy. *Medical Physics*, 20(3):781–787.

[NATO, 1996] NATO (1996). *Nato Handbook on the Medical Aspects of NBC Defensive Operations*. Departments of the Army, The Navy, and the Air Force, Washington, D.C. AMedP-6(B).

[NBS, 1982] NBS (1982). Medical physics data book. *National Bureau of Standards*, NBS Handbook No. 138.

[NCRP, 1991] NCRP (1991). Calibration of survey instruments used in radiation protection for the assessment of ionizing radiation fields and radioactive protection for the assessment of ionizing radiation fields and radioactive surface contamination. Technical Report 112, National Council on Radiation Protection and Measurements, 7910 Woodmount Avenue, Suite 400, Bethesda, MD, 20814.

[NCRP, 2005] NCRP (2005). Structural shielding design and evaluation for megavoltage x- and gamma-ray radiotherapy facilities. Technical Report 151, National Council on Radiation Protection and Measurements, 7910 Woodmount Avenue, Suite 400, Bethesda, MD, 20814.

[NNDC, 2013] NNDC (2013). National nuclear data center. Evaluated Nuclear Data File (ENDF).

[NRC, 1977] NRC (1977). Personnel neutron dosimeters. Technical report, U.S. Nuclear Regulatory Commission.

[Ongaro et al., 2000] Ongaro, C., Zanini, A., Nastasi, U., Rodenas, J., Ottaviano, G., and Manfredotti, C. (2000). Analysis of photoneutron spectra produced in medical accelerators. *Physics in Medicine and Biology*, 45:L55–L61.

[Paredes et al., 1999] Paredes, L., Genis, R., Balcazar, M., Tavera, L., and Camacho, E. (1999). Fast neutron leakage in 18 mev medical electron accelerator. *Radiation Measurements*, 31:475–478.

[Pena et al., 2005] Pena, J., Franco, L., Gomez, F., Iglesias, A., Pardo, J., and Pombar, M. (2005). Monte carlo study of siemens primus photoneutron production. *Institute of Physics Publishing*, 50:5921–5933.

[Podgorsak, 2003] Podgorsak, E. B., editor (2003). *Review of Radiation Oncology: A Handbook for Teachers and Students*. International Atomic Energy Agency.

[Reft et al., 2006] Reft, C. S., Runkel-Muller, R., and Myrianthopoulos, L. (2006). In vivo and phantom measurements of the secondary photon and neutron doses for prostate patients undergoing 18 mv imrt. *Medical Physics*, 33(10):3734–3742.

[Rinard, 1991] Rinard, P. (1991). Neutron interaction with matter. In *Passive Nondestructive Assay of Nuclear Materials*, number 375-377, chapter 12. Los Alamos National Laboratory, Los Alamos, NM 87545. NUREG/CR-5550.

[Saeed et al., 2009] Saeed, M. K., Moustafa, O., Yasin, O. A., Tuniz, C., and Habbani, F. I. (2009). Doses to patients from photoneutrons emitted in a medical linear accelerator. *Radiation Protection Dosimetry*, 133(3):130–135.

[Sanchez-Doblado et al., 2012] Sanchez-Doblado, F., Domingo, C., Gomez, F., Sanchez-Nieto, B., and Muniz, J. L. (2012). Estimation of neutron-equivalent dose in organs of patients undergoing radiotherapy by the use of a novel online digital detector. *Physics in Medicine and Biology*, 57:6167–6191.

[Serway et al., 2005] Serway, R. A., Moses, C. J., and Moyer, C. A. (2005). *Modern Physics*. Brook/Cole- Thomson Learning, Belmont, CA, third edition.

[Siebert and Schuhmacher, 1995] Siebert, B. R. L. and Schuhmacher, H. (1995). Quality factors, ambient and personal dose equivalent for neutrons, based on the new icru stopping power data for protons and alpha particles. *Radiation Protection Dosimetry*.

[Sims and Killough, 1983] Sims, C. S. and Killough, G. G. (1983). Neutron fluence-to-dose equivalent conversion factors: A comparison of data sets and interpolation methods. *Radiation Protection Dosimetry*, 5(1):45–48.

[Somogyi and Szalay, 1973] Somogyi, G. and Szalay, S. A. (1973). Track diameter kinetics in dielectric track detectors. *Nuclear Instruments and Methods*, 109(2):211–232.

[Souhami and Tobias, 1986] Souhami, R. L. and Tobias, J. S. (1986). Cancer and its management. *Oxford: Blackwell Scientific*.

[Spurny et al., 1996] Spurny, F., Bednar, J., hjohansson, L., and Satherberg, A. (1996). Linear energy transer spectra of secondary particles in cr-39 track etch detectors. *Radiation Measrements*, 26(5):645–649.

[Statkiewicz-Sherer et al., 2011] Statkiewicz-Sherer, M. A., Visconti, P. J., and Ritenour, E. R. (2011). *Radiation protection in medical radiography*. Mosby Elsevier, Maryland Heights, MO, sixth edition.

[Takam et al., 2001] Takam, R., Bezak, E., Marcu, L. G., and Yeoh, E. (2001). Out-of-field neutron and leakage photon exposures and the associated risk of second cancers in high-energy photon radiotherapy: Current status. *Radiation Research*, 176:508–520.

[Tobias, 1996] Tobias, J. S. (1996). The role of radiotherapy in the management of cancer - an overview. *Ann Acad Med Singapore*, 25:371–379.

[Tommasino and Armellini, 1973] Tommasino, L. and Armellini, C. (1973). A new etching technique for damage track detectors. *Radiation Effects*, 20:253–255.

[van der Giessen and Bierhuizen, 1997] van der Giessen, P. H. and Bierhuizen, H. W. J. (1997). Comparison of measured and calculated peripheral doses in patients undergoing radiation therapy. *Radiotherapy and Oncology*, 42:265–270.

[Vanhavere et al., 2004] Vanhavere, F., Huyskens, D., and Struelens, L. (2004). Peripheral neutron and gamma doses in radiotherapy with an 18 mv linear accelerator. *Radiation Protection Dosimetry*, 110(1-4):607–612.

[Zanini et al., 2004] Zanini, A., Durisi, E., Fasolo, F., Ongaro, C., Visca, L., Nastasi, U., Bun, K. W., Scielzo, G., Adler, J. O., Annand, J. R. M., and Rosner, G. (2004). Monte carlo simulation of the photoneutron field in linac radiotherapy treatments with different collimation systems. *Physics in Medicine and Biology*, 49:571–582.

[Zhou, 2012] Zhou, D. (2012). *CR-39 Plastic Nuclear Track Detectors in Physics Research*. Nova Science Publishers, Inc, New York.

APPENDIX A

Integral Fluence

Below are a list of figures showing the Integral Fluence vs $LET_{\infty}H_2O$ of each PNTD. Each caption of the figure explains the exposure of each PNTD, (x-ray energy, type, and position in cm (off-axis to beam, depth).

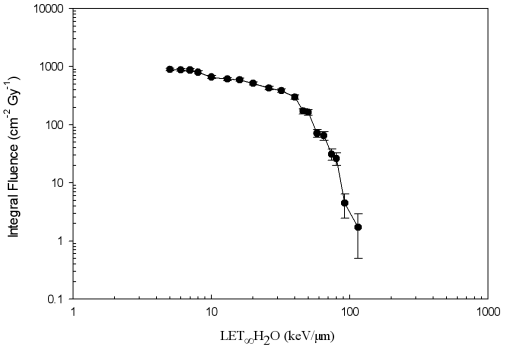

Figure A.1 18 MV Air (0,0)

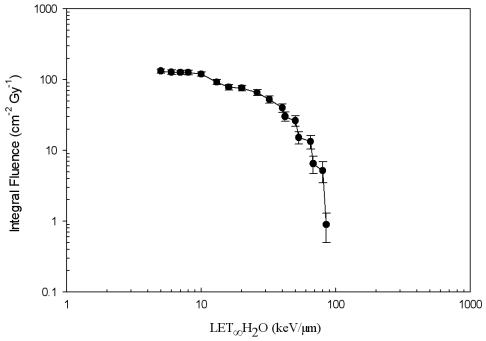

Figure A.3 18 MV Air (40,0)

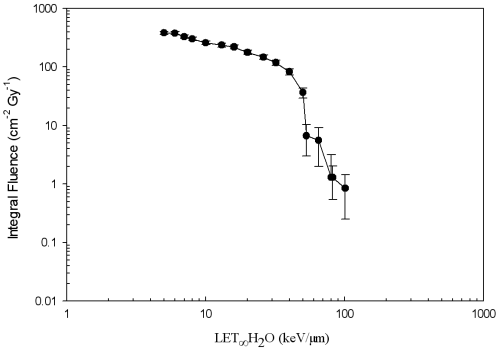

Figure A.2 18 MV Air (20,0)

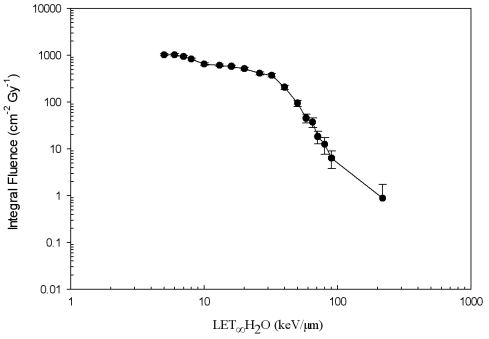

Figure A.4 18 MV Phantom (0,0)

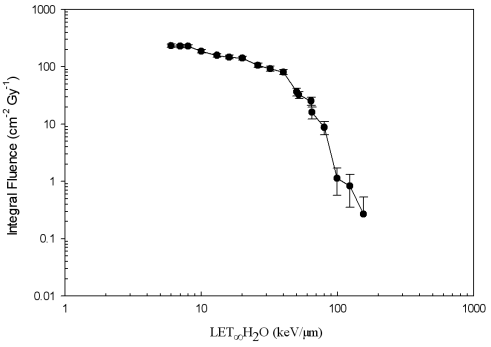

Figure A.5 18 MV Phantom (0,5)

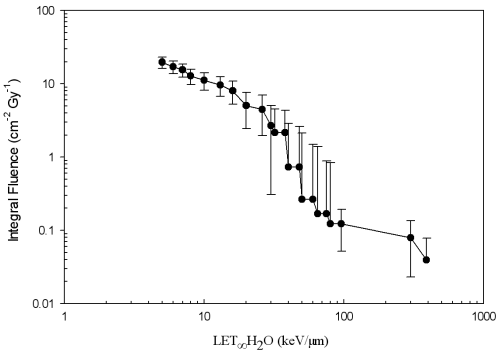

Figure A.8 18 MV Phantom (40,10)

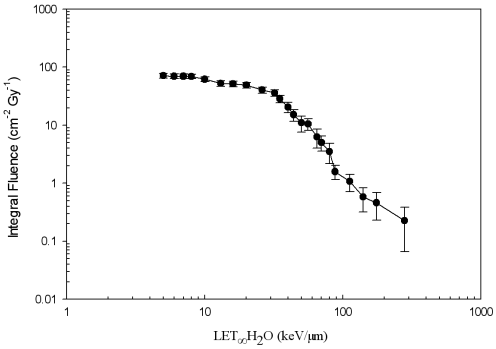

Figure A.6 18 MV Phantom (0,10)

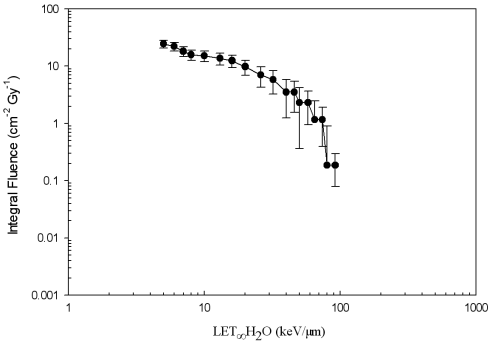

Figure A.9 10 MV Air (0,0)

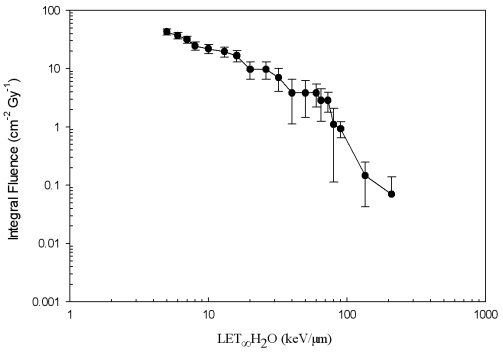

Figure A.7 18 MV Phantom (20,10)

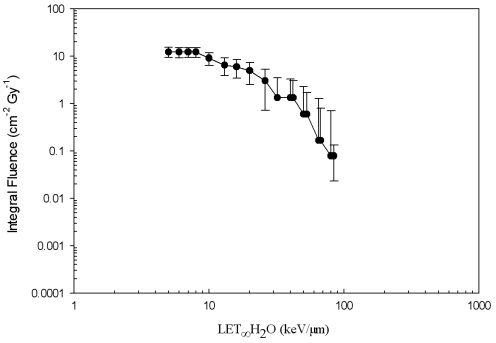

Figure A.10 10 MV Air (20,0)

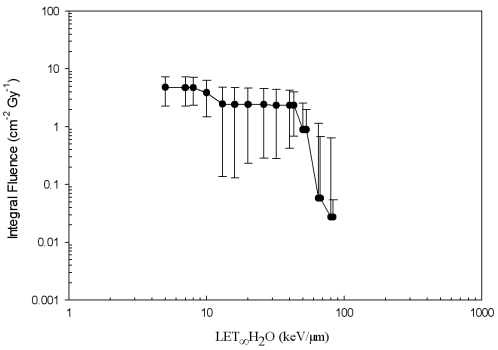

Figure A.11 10 MV Air (40,0)

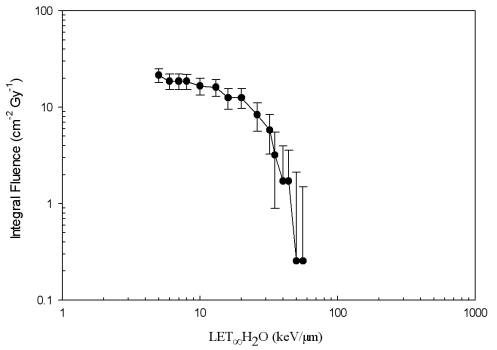

Figure A.12 10 MV Phantom (0,0)

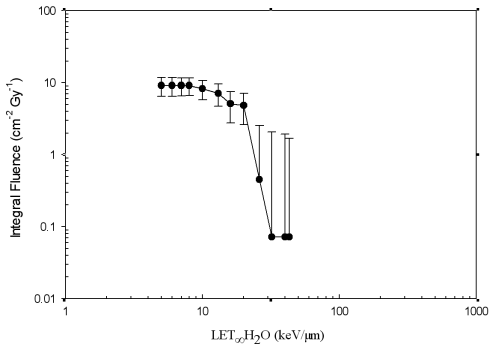

Figure A.13 10 MV Phantom (0,5)

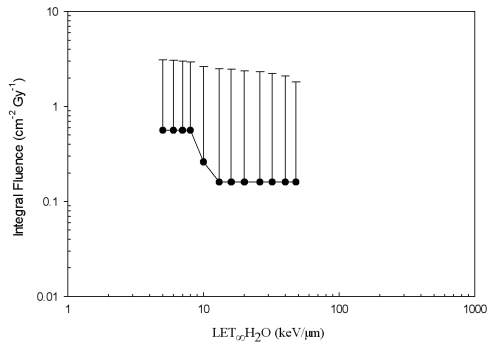

Figure A.14 10 MV Phantom (0,10)

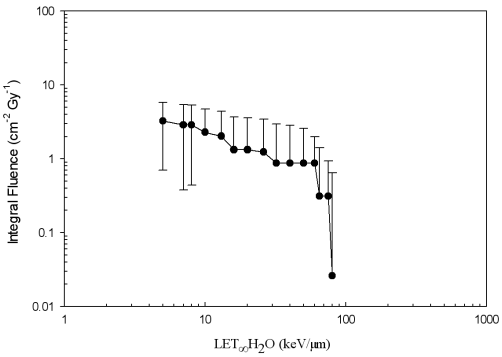

Figure A.15 10 MV Phantom (20,10)

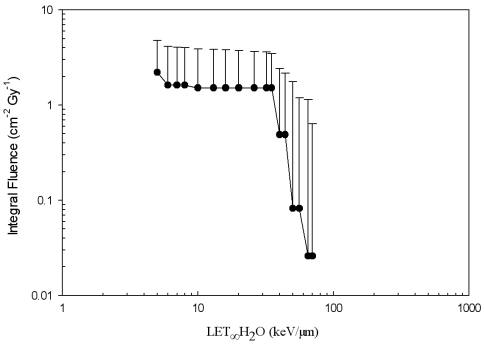

Figure A.16 10 MV Phantom (40,10)

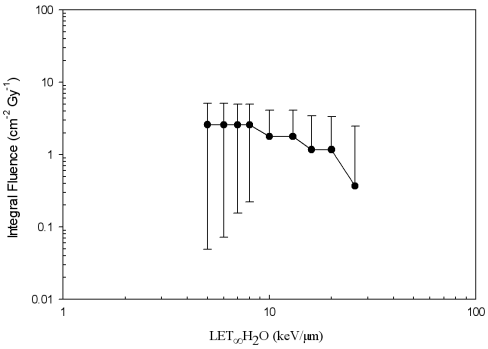

Figure A.17 6 MV Air (0,0)

APPENDIX B

Differential Fluence vs LET

Below are a list of figures showing the differential fluence vs $LET_{\infty}H_2O$ of each PNTD. Each caption of the figure explains the exposure of each PNTD, (x-ray energy, type, and position in cm (off-axis to beam, depth).

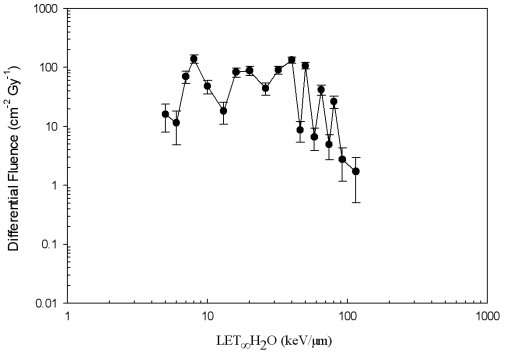

Figure B.1 18 MV Air (0,0)

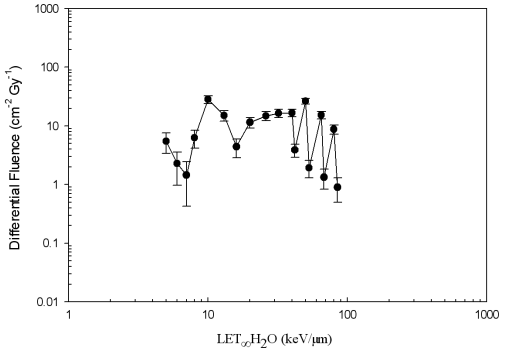

Figure B.3 18 MV Air (40,0)

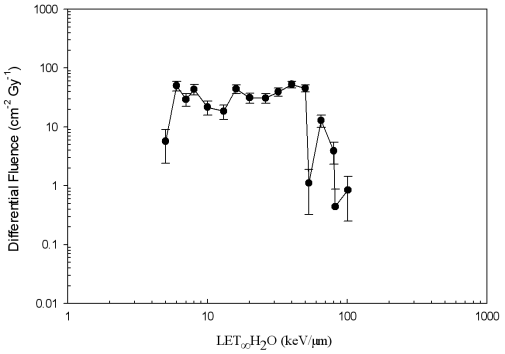

Figure B.2 18 MV Air (20,0)

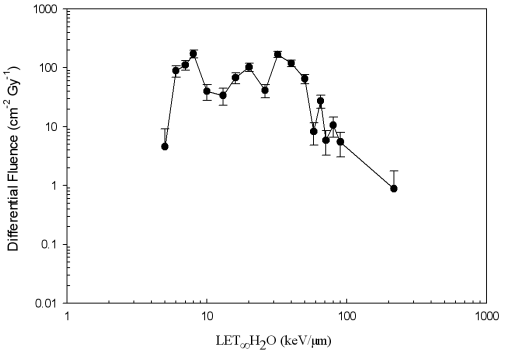

Figure B.4 18 MV Phantom (0,0)

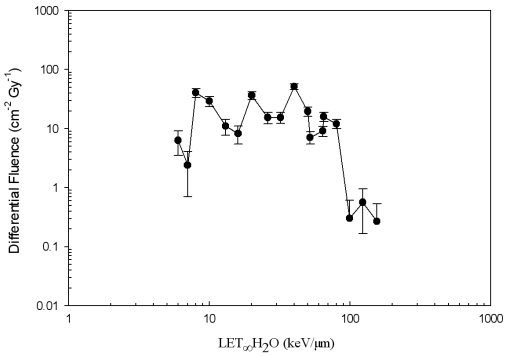

Figure B.5 18 MV Phantom (0,5)

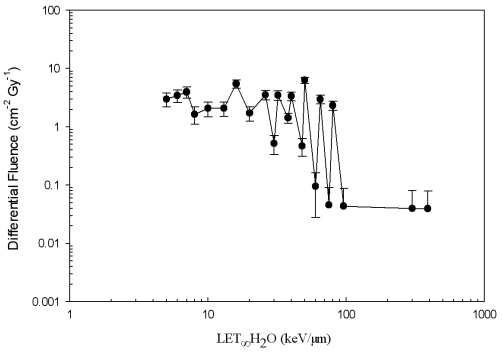

Figure B.8 18 MV Phantom (40,10)

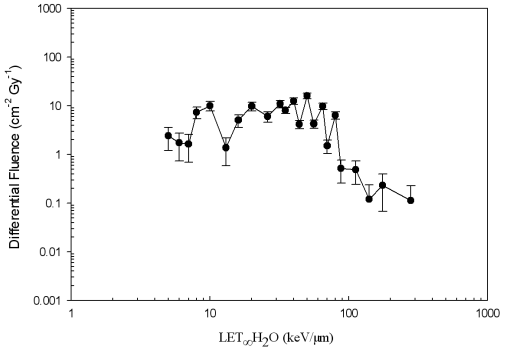

Figure B.6 18 MV Phantom (0,10)

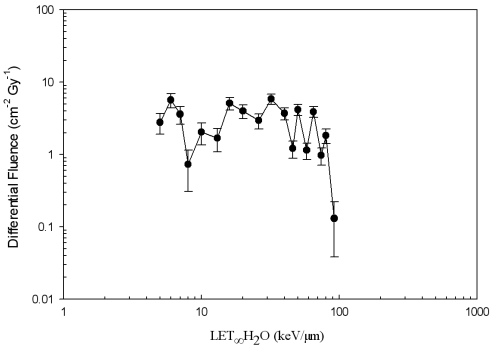

Figure B.9 10 MV Air (0,0)

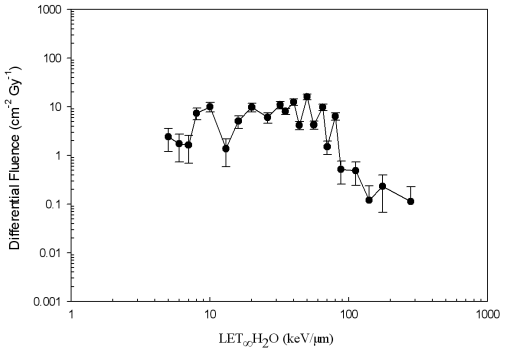

Figure B.7 18 MV Phantom (20,10)

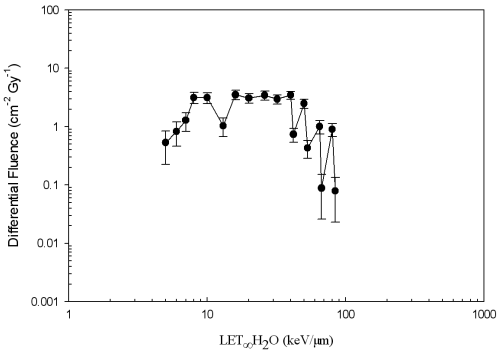

Figure B.10 10 MV Air (20,0)

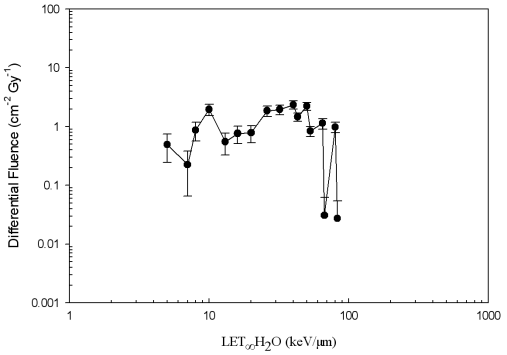

Figure B.11 10 MV Air (40,0)

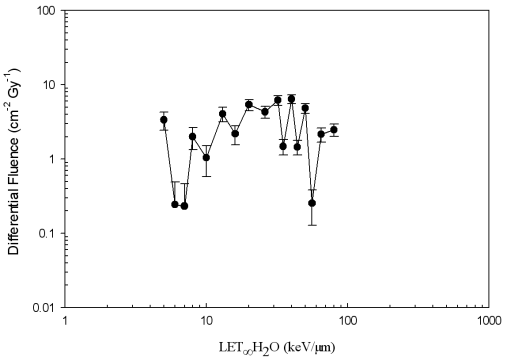

Figure B.12 10 MV Phantom (0,0)

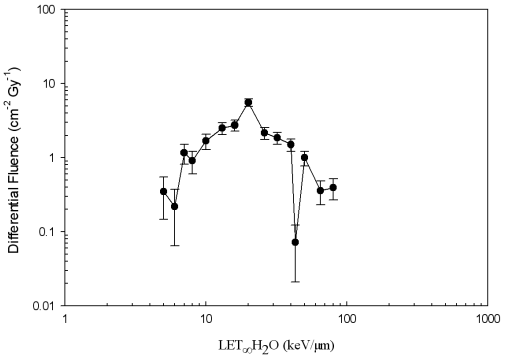

Figure B.13 10 MV Phantom (0,5)

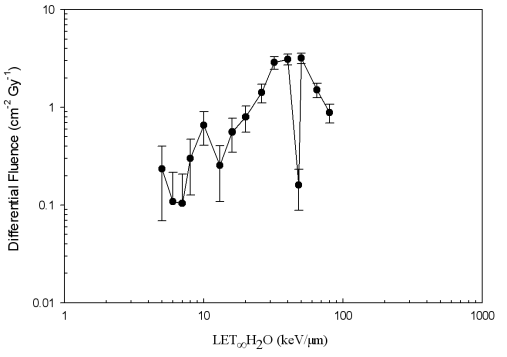

Figure B.14 10 MV Phantom (0,10)

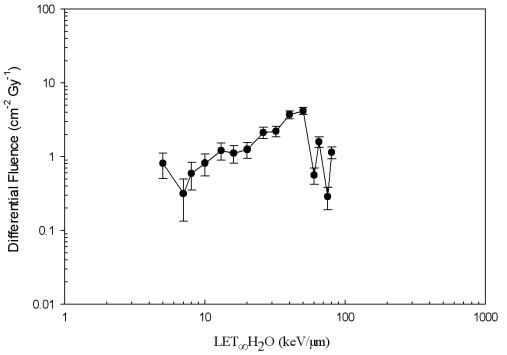

Figure B.15 10 MV Phantom (20,10)

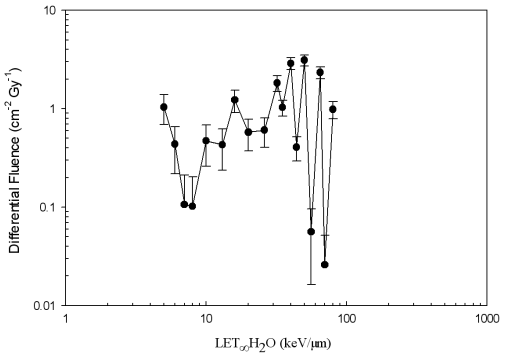

Figure B.16 10 MV Phantom (40,10)

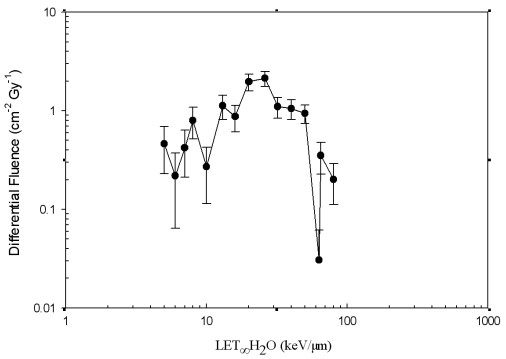

Figure B.17 6 MV Air (0,0)

VITA

Jonathan Monson

Candidate for the Degree of

Masters of Science

Thesis: Measurement of Photo-Neutrons From a Medical Linear Accelerator Using CR-39 Plastic Nuclear Track Detectors

Major Field: Medical Physics

Biographical:

Personal Data:

Born June 29, 1984 in Provo, Utah, United States

Education:

Received a Bachelors of Science degree in Physics at Brigham Young University - Idaho, Rexburg, Idaho, United States, 2010.

Completed the requirements for the degree of Master of Science in Medical Physics at Oklahoma State University in August, 2013.